A generic model of double-diffusive convection: extended and localized patterns

Haifaa Faraj Alrihieli

Submitted in accordance with the requirements for the degree of
Doctor of Philosophy

The University of Leeds
Department of Applied Mathematics

September 2019

To Fahad

and my lovely kids

Sondos, Shadan, Jaser, and Basel

Abstract

Two-dimensional double-diffusive convection in a horizontal layer of fluid heated from below exhibits a variety of dynamical behaviours. The system has two competing gradients that drive motion in the fluid: the temperature gradient and the solute gradient. With low solute gradient, the first bifurcation for the resting (trivial) state as the temperature gradient is increased is a pitchfork bifurcation leading to steady convection. With larger solute gradient, the bifurcation changes to a Hopf bifurcation leading to oscillatory convection. In double-diffusive convection with idealised boundary conditions, these two forms of convection set in with the same horizontal wavelength. The point where the pitchfork and Hopf bifurcation coincide is called the Takens–Bogdanov point. This dissertation concentrates on understanding the bifurcation behaviour close to this Takens–Bogdanov point in domains that are large compared to the wavelength of the pattern of convection. A new partial differential equation (PDE) model that replicates the linear behaviour of double-diffusive convection is presented. The model has a variety of nonlinear terms, which allows considerable flexibility in its behaviour, and is the first Swift–Hohenberg-type model that has a Takens–Bogdanov primary bifurcation. Compared to the full PDEs for double-diffusive convection, the model is simple, which helps to investigate the nonlinear behaviour numerically and analytically, especially in large domains. From solving the model numerically, different patterns have been obtained: extended and localized patterns. Extended solutions such as steady states (SS), travelling waves (TW), and standing waves (SW) convection have been found in small and large domains. In large domains, and at different parameter values, localized patterns have also been found. Localized steady states (LSS) are found in the subcritical regime of the pitchfork bifurcation and localized travelling waves (LTW) are found in the subcritical regime of the Hopf bifurcation. In both cases, the trivial state and a large-amplitude stable pattern coexist. Previously, LSS and LTW have been found in numerical and experimental investigations of thermosolutal and binary convection. Our work helps explain the origins of these states and allows detailed investigation of their properties. The model also exhibits new types of patterns; LSS with modulated waves (MW) background in the parameter region where small-amplitude SW and large-amplitude SS are both stable, and LTW with SS background in the region where small-amplitude SS and large-amplitude TW are both stable. We make use of the analysis of the Takens–Bogdanov normal form done by Dangelmayr and Knobloch (1987) in order to find parameter values in the model PDE where the pitchfork or Hopf bifurcations are supercritical or subcritical. This analysis does not predict large-amplitude stable extended patterns in the subcritical cases; we rely on global stability of the PDE model to ensure that these stable large-amplitude states exist. The two last states we found (LSS with MW background and LTW with SS background) are new and have not been observed before in systems of double-diffusive convection. The new model is sufficiently general that it could be used to investigate other convection problems such as magnetoconvection and rotating convection.

Acknowledgements

First and foremost, I would like to thank ALLAH for giving me the patience, strength, and making the completion of this thesis possible.

Starting research with a new project is not easy and cannot be done without getting enough support from people around me. I am particularly grateful to my supervisors Prof. Alastair Rucklidge and Dr. Priya Subramanian for their unlimited support and guidance, thoughtful suggestions, objective comments, practical advice, and insightful direction. They encouraged me to participate in many conferences, which was very useful. Their guidance helped me in all the time of research and writing of the thesis.

I am grateful to my husband Fahad and my kids Sondos, Shadan, Jaser and Basel for their love, support, encouragement, and for helping me throughout my academic life. All my thanks go to my mother Azizh, my aunt Dkhyla, my brothers and my sisters for their love, emotional support, and prayers. I dedicate this dissertation to the loving memory of my father, Faraj, and my cousin Mohammed who left us inspiring memories.

Also, l would like to thank my friends I have met inside and outside the university for their time and support.

Finally, I am greatly thankful to Leeds University for providing a comfortable environment for a postgraduate student. I would also like to express thanks and appreciation to Tabuk University for providing financial support to pursue my PhD degree.

Contents

List of Figures

List of Tables

Abbreviations

DK	Dangelmayr and Knobloch
ETD	Exponential Time Differencing
FFT	Fast Fourier Transform
LSS	Localized steady states
LSW	Localized standing waves
LTW	Localized travelling waves
MW	Modulated waves
ODE	Ordinary Differential Equation
PDE	Partial Differential Equation
SN	Saddle-node
SS	Steady states
SW	Standing waves
T	Trivial state
TB	Takens–Bogdanov
TW	Travelling waves

Chapter 1

Introduction

1.1 Thermal convection

Convection occurs when a horizontal layer of fluid is heated from below. As the temperature gradient increases, the fluid at the bottom expands and becomes less dense than the fluid at the top. The buoyant fluid rises through the colder layer, cools and becomes heavier, and goes down again. Repeating the rising and falling in different locations causes the fluid to form spatial patterns driven by the thermal gradient between the top and bottom layers of the fluid (see Figure 1.1 a). Convection can exhibit different patterns, such as rolls, squares, hexagons, or more complicated patterns, depending on the fluid properties and the details of the physical system [43, 66, 104]. In nature, there are many examples of convection, such as systems with convective heat transfer, mantle convection, atmospheric, and oceanic circulation [66].

The earliest experiments on the instability behaviour of thermal convection were conducted by Bénard in 1900 [26, 39, 63, 71, 81, 107]. Bénard melted a thin layer of wax in a container by heating it from below with a free surface on

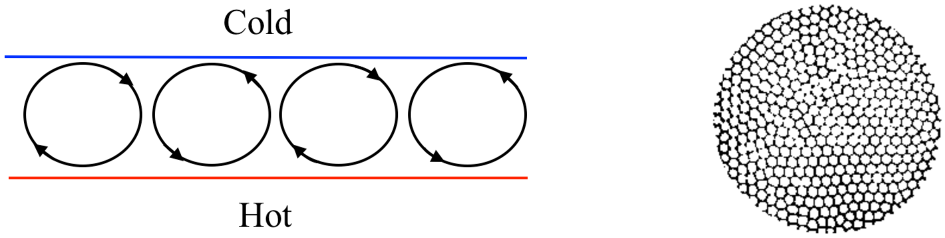

(a) (b)

Figure 1.1: (a) Schematic diagram of convection cells occurring in two-dimensional Rayleigh–Bénard convection for a fluid hated from below. (b) Top view of a hexagonal pattern in a Bénard experiment in a thin layer of spermaceti wax heated from below from [71].

the top. At the beginning of the experiment, there was no motion in the melted wax. When the temperature exceeded some critical temperature, Bénard saw hexagonal patterns appear in the top surface of the fluid (see Figure 1.1 b). In 1916, Rayleigh treated Bénard's problem as a stability problem using the theory of hydrodynamic stability [87]. Rayleigh considered a fluid that was bounded by two infinite horizontal plates which are maintained at constant uniform temperatures. Rayleigh assumed that the fluid is incompressible based on the *Boussinesq approximation* [26, 87, 97]. This approximation involves two assumptions: firstly, it assumes that the depth of the motions is less than the scale heights of pressure, temperature and density. Secondly, it assumes that the fluctuations in density is driven by thermal effects rather than being driven by the pressure. As a result of the Boussinesq approximation, density variations are neglected everywhere in the equation of motion except in the buoyancy term, as long as the temperature does not increase significantly. This approximation have been used to simplified the basic equations of convection system. Rayleigh's linear theory showed that instability occurs when the temperature difference between the top and bottom of the fluid layer ΔT is just above the critical temperature difference ΔT_c, through a non-dimensional parameter, the Rayleigh number Ra, which we will define in Section 1.1.4. Rayleigh predicted the value of the Rayleigh number at which the convection would onset for a horizontal layer of fluid heated from below.

In the next sections, we will introduce the equations governing two-dimensional Rayleigh–Bénard convection, and we will discuss the linear stability analysis.

1.1.1 Governing equations

Let us consider the non-dimensional partial differential equations (PDEs) that governing two-dimensional Rayleigh–Bénard convection in the layer of fluid heated from below, with the motion confined to a container of depth d in the z-direction and width L in the x-direction [39]. In two-dimensional convection, we allow quantities to be functions of x, z, and t only with no y-dependence. Since we are considering two-dimensional flows, dependent on x and z, then via the incompressibility condition

$$\nabla \cdot \mathbf{u} = \frac{\partial u}{\partial x} + 0 + \frac{\partial w}{\partial z} = 0, \tag{1.1}$$

where $\mathbf{u} = (u, 0, w)$ is the velocity field in (x, y, z) coordinates we introduce a stream-function ψ that satisfies the following

$$u = \frac{-\partial \psi}{\partial z}, \qquad w = \frac{\partial \psi}{\partial x}. \tag{1.2}$$

Therefore, we represent the governing two-dimensional Rayleigh–Bénard convection with stream-function ψ where the continuity equation (1.1) now becomes irrelevant since

$$\frac{\partial u}{\partial x} + 0 + \frac{\partial w}{\partial z} = \frac{-\partial^2 \psi}{\partial x \partial z} + 0 + \frac{\partial^2 \psi}{\partial x \partial z} = 0, \tag{1.3}$$

and any flow described by such a stream-function ψ is incompressible [9]. The PDEs then are expressed in terms of stream-function ψ and temperature perturbation T for a Boussinesq fluid as follows:

$$\begin{gathered} \frac{\partial \nabla^2 \psi}{\partial t} + J(\psi, \nabla^2 \psi) = Pr \nabla^4 \psi + RaPr \frac{\partial T}{\partial x}, \\ \frac{\partial T}{\partial t} + J(\psi, T) = \nabla^2 T, \end{gathered} \tag{1.4}$$

where ∇^2 is the Laplacian operator, defined by

$$\nabla^2 = \frac{\partial^2}{\partial x^2} + \frac{\partial^2}{\partial z^2}, \tag{1.5}$$

and J is the Jacobian operator, defined by

$$J(f, g) = \frac{\partial f}{\partial x}\frac{\partial g}{\partial z} - \frac{\partial f}{\partial z}\frac{\partial g}{\partial x}. \tag{1.6}$$

All variables in the governing equations (1.4) are in dimensionless form; the x and z are scaled by the depth d and time is scaled by $\frac{d^2}{\kappa}$, where κ is the thermal diffusivity. The temperature T is scaled by the temperature difference ΔT. The two dimensionless parameters are the Rayleigh number Ra and the Prandtl number Pr, given by

$$Ra = \frac{g\alpha\Delta T d^3}{\kappa\nu}, \quad Pr = \frac{\nu}{\kappa}, \tag{1.7}$$

where α is the thermal expansion coefficient, ν is the kinematic viscosity and g is the acceleration due to gravity (vertically downwards). The Rayleigh number Ra is considered as a control parameter in the thermal system since it has the temperature difference ΔT, which can be changed during the experiments. The momentum and heat in the governing equations (1.4) all diffuse and are also convectively transported by the fluid motion.

1.1.2 Boundary conditions

The fluid is confined between two horizontal plates $z = 0$ and $z = 1$, which are maintained at constant uniform temperatures at the top and bottom boundary as follows:

$$T = 1 \quad \text{at} \quad z = 0, \quad \text{and} \quad T = 0 \quad \text{at} \quad z = 1. \tag{1.8}$$

The system we consider is periodic in x with a cell of width L and we want to solve the equations of convection system (1.4) in the region $(0 \leqslant x \leqslant L; 0 \leqslant z \leqslant 1)$. Therefore, we impose periodic boundary conditions appropriate to a cell of width L. We assume the simplest boundary conditions, the stress-free boundary conditions, for which no tangential stresses act at the top and bottom surfaces, with reflection symmetry about $x = 0$ (so there is no flow or heat flux through the sides of the boundary). Thus

$$\begin{aligned} \psi &= 0 \qquad \text{at} \qquad z = 0, \qquad z = 1 \qquad \text{and} \qquad x = 0, \qquad x = L, \\ \frac{\partial^2 \psi}{\partial z^2} &= 0 \qquad \text{at} \qquad z = 0, \qquad z = 1 \qquad \text{and} \qquad x = 0, \qquad x = L, \\ \frac{\partial T}{\partial x} &= 0 \qquad \text{at} \qquad x = 0, \qquad \text{and} \qquad x = L. \end{aligned} \tag{1.9}$$

By imposing this boundary conditions, we seek spatial periodic solutions of horizontal period $\frac{\pi}{L}$.

1.1.3 Conduction state

The system (1.4) has the static (conductive) solution, when

$$\psi = 0, \qquad T = 1 - z. \tag{1.10}$$

It is convenient to subtract off this solution by writing

$$T = 1 - z + \theta(x, z, t). \tag{1.11}$$

Substituting the expansion (1.11) into (1.4), the system is rewritten as follows:

$$\begin{aligned} \frac{\partial \nabla^2 \psi}{\partial t} + J(\psi, \nabla^2 \psi) &= Pr \nabla^4 \psi + Ra Pr \frac{\partial \theta}{\partial x}, \\ \frac{\partial \theta}{\partial t} + J(\psi, \theta) &= \frac{\partial \psi}{\partial x} + \nabla^2 \theta, \end{aligned} \tag{1.12}$$

and the boundary conditions become:

$$\begin{aligned}
\psi &= 0 \quad \text{at} \quad z = 0, \quad z = 1 \quad \text{and} \quad x = 0, \quad x = L,\\
\theta &= 0 \quad \text{at} \quad z = 0, \quad \text{and} \quad z = 1,\\
\frac{\partial^2\psi}{\partial z^2} &= 0 \quad \text{at} \quad z = 0, \quad z = 1 \quad \text{and} \quad x = 0, \quad x = L,\\
\frac{\partial\theta}{\partial x} &= 0 \quad \text{at} \quad x = 0, \quad \text{and} \quad x = L.
\end{aligned} \tag{1.13}$$

The equations of Rayleigh–Bénard convection are equivariant with respect to reflections symmetry in a vertical plane, the Z_2 symmetry, and invariant under the transformation $(x, z, \psi, \theta) \to (x, 1 - z, -\psi, -\theta)$ and $(x, z, \psi, \theta) \to (L - x, z, -\psi, -\theta)$. The system described above has the static (conductive) solution $\psi = \theta = 0$.

1.1.4 Linear stability analysis

The governing equations of thermal convection (1.12) contain nonlinear terms which make the theoretical study of such a system complicated. A fundamental approach to studying such a system is to simplify the process using linear stability analysis. In linear stability analysis, we neglect all the nonlinear terms in the PDEs (1.12) and we examine only the stability of small perturbations to determine whether their amplitude grows or decays with time. The normal mode solutions that satisfy the boundary conditions (1.13) are:

$$\begin{aligned}
\psi(x, z, t) &= \psi_0 e^{\sigma t} \sin\frac{\pi x}{L} \sin \pi z,\\
\theta(x, z, t) &= \theta_0 e^{\sigma t} \cos\frac{\pi x}{L} \sin \pi z,
\end{aligned} \tag{1.14}$$

where σ is the growth rate that determines the stability of the system and $\frac{\pi}{L}$ is the horizontal wavenumber of the mode. By differentiating (1.14) and substituting into the PDEs (1.12), we get the system on the matrix form as follows:

$$\begin{pmatrix} \sigma a^2 + Pra^4 & -kRaPr \\ -k & \sigma + a^2 \end{pmatrix} \begin{pmatrix} \psi_0 \\ \theta_0 \end{pmatrix} = \begin{pmatrix} 0 \\ 0 \end{pmatrix}, \tag{1.15}$$

where $a^2 = (k^2 + \pi^2)$ and $k = \frac{\pi}{L}$. Setting the determinant to zero to obtain the eigenvalues $\sigma_{1,2}$, that correspond to the eigenvectors (ψ_0, θ_0) leads to the dispersion relation

$$\sigma^2 + a^2(Pr + 1)\sigma + a^4 Pr - RaPr\frac{k^2}{a^2} = 0, \tag{1.16}$$

where the eigenvalues $\sigma_{1,2}$ are given by

$$\sigma_{1,2} = \frac{-a^2(Pr+1) \pm \sqrt{a^4(Pr+1)^2 - 4(a^4 Pr - RaPr\frac{k^2}{a^2})}}{2}. \tag{1.17}$$

The boundary of stability is obtained by putting $\sigma = 0$ in the quadratic equation (1.16). Thus, the value of Ra in which the system is considered marginally stable is

$$Ra = \frac{a^6}{k^2} = \frac{(k^2 + \pi^2)^3}{k^2}. \tag{1.18}$$

Then minimizing Ra with respect to k^2, we obtain the critical Rayleigh number:

$$Ra_c = \frac{27\pi^4}{4} \simeq 657.5, \tag{1.19}$$

where the critical wavenumber is

$$k_c = \frac{\pi}{\sqrt{2}} \simeq 2.221. \tag{1.20}$$

It follows that if $Ra > Ra_c$, the system is linearly unstable, and if $Ra < Ra_c$, the system is linearly stable. Figure 1.2 (a) shows the marginal stability curve $\sigma = 0$, which is the boundary between the growing (unstable) and decaying (stable)

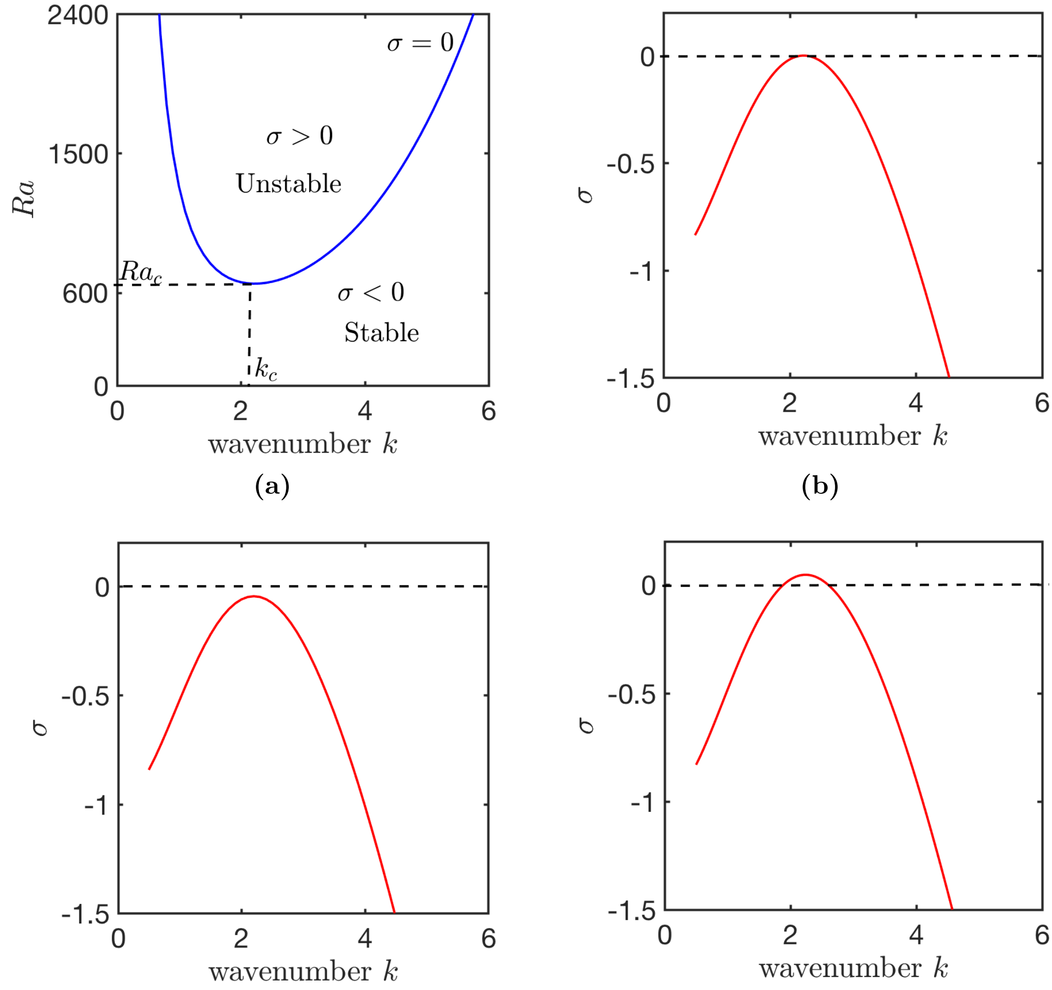

(a) **(b)** **(c)** **(d)**

Figure 1.2: (a) The marginal stability curve: graph of critical Rayleigh number Ra against the wavenumber k from (1.18). (b,c,d) Sketch of the graph of $\sigma(k, Ra)$ for fixed $Pr = 0.1$, (b) $Ra = Ra_c = 657.5$, (c) $Ra = 650 < Ra_c$, (d) $Ra = 680 > Ra_c$ from (1.17).

modes in the plane of the Rayleigh number Ra and the wavenumber k. Figure 1.2 (b,c,d) show the graph of σ as a function of k for fixed $Pr = 0.1$ where (b) $Ra = Ra_c$, (c) $Ra < Ra_c$ and (d) $Ra > Ra_c$.

1.1.5 Nonlinear convection

Rayleigh–Bénard convection sets in when the Rayleigh number exceeds the critical Rayleigh number Ra_c. Therefore, any perturbation given to the system will grow exponentially until nonlinear terms become important. The nonlinear system then can be reduced to an amplitude equation using weakly nonlinear method [38, 80, 94]. The method consists of an expansion of the solution of the full PDEs close to the critical value of the control parameter Ra in terms of a small parameter. Substituting the expansion into the governing equation (1.12), resulting in a reduced set of equations that describes the nonlinear interaction between a few unstable modes. We will give detailed examples of this kind of calculation in Section 2.4, but in this case, the equation close to Ra_c for the amplitude $u(t)$ for Rayleigh–Bénard convection takes the form:

$$\frac{du}{dt} = \frac{Pra^2}{(1+Pr)}\mu u - \frac{Prk^2}{8\,(1+Pr)}u^3, \tag{1.21}$$

where $a^2 = (k^2 + \pi^2)$, $k = \frac{\pi}{L}$ and μ is the unfolding parameter close to the critical value of the control parameter Ra, $\mu = Ra - Ra_c$. The amplitude equation (1.21) indicates that the primary bifurcation of Rayleigh–Bénard convection is a supercritical pitchfork bifurcation. A great number of investigations have been done in understanding the nonlinear fluctuation and the instability in Rayleigh–Bénard convection. Patterns like rolls, hexagons, rotating spirals, spiral-defect chaos and many other discoveries have been observed in Rayleigh–Bénard convection. An important review of Rayleigh–Bénard studies is made by [17, 71].

1.2 Swift–Hohenberg equation

In the context of Rayleigh–Bénard convection, we mention the Swift–Hohenberg equation. This equation was derived initially by Swift and Hohenberg in 1977 [102] to describe the effects of thermal fluctuations and the evolution of roll patterns close to the onset of Rayleigh–Bénard convection. Later, the Swift–Hohenberg equation has been considered as a model of pattern formation in many physical problems, including convection [23, 32, 35], chemical reactions with diffusion [69] and nonlinear optics [70], as it reproduces many universal features of pattern formation. The Swift–Hohenberg equation is a partial differential equation in the form:

$$\frac{\partial u}{\partial t} = ru - (q_c^2 + \partial_{xx})^2 u + N(u;b), \tag{1.22}$$

where $u(x,t)$ is a real scalar variable that represents the local convection motion, r is a control parameter that corresponds to the Rayleigh number Ra in Rayleigh–Bénard convection, q_c is the critical wavenumber, and $N(u;b)$ refers to the nonlinear terms, where b represents further parameters. The linear part of (1.22) have two control parameters r and q_c. Applying the following scaling

$$t \to \frac{1}{q_c^4} t, \qquad r \to q_c^4 r, \qquad x \to \frac{1}{q_c} x, \qquad N(u;b) \to q_c^4 N(u;b) \tag{1.23}$$

to (1.22) we get the same equation with $q_c = 1$. Therefore, the linear part of (1.22) is fully parameterized with only one control parameter r which helps to simplified the analysis and the numeric integration. Thus, we consider $q_c = 1$ in this thesis.

1.2.1 Linear stability analysis

The linear stability of the trivial state $u = 0$, is obtained by considering solutions of the form $u(x, t) = e^{\sigma t + ikx}$, where σ is the growth rate of a perturbation with wavenumber k. Then, the dispersion relation is

$$\sigma = r - (1 - k^2)^2. \tag{1.24}$$

Marginal stability occurs when $\sigma = 0$, at which point

$$r = (1 - k^2)^2. \tag{1.25}$$

Then minimizing the marginal value r with respect to the wavenumber k, we obtain $r_c = 0$ with $k_c = \pm 1$. The trivial solution is stable when $r < 0$ since $\sigma < 0$ for all k. If $r > 0$, there is instability for a band of wavenumbers centred on $k_c = \pm 1$. Figure 1.3 (a) shows the marginal stability curve from (1.25) and the plot of the dispersion relation is shown in Figure 1.3 (b,c) and (d). The linear behaviour of the Swift–Hohenberg equation with control parameter r replicates the linear behaviour of the Rayleigh–Bénard convection with control parameter Ra which is one reason the Swift–Hohenberg equation was proposed as a model of Rayleigh–Bénard convection [102].

1.2.2 Nonlinear results: extended and localized states

In the Swift–Hohenberg equation, two common nonlinearities are considered: the quadratic-cubic nonlinearities $N_{23}(u; b) = bu^2 - u^3$ [15, 18, 19] and the cubic-quintic nonlinearities $N_{35}(u; b) = bu^3 - u^5$ [23]. For periodic boundary conditions, the model (1.22) with both nonlinearities N_{23} and N_{35} has translation symmetry and is reversible, that it is equivariant under spatial reflections $(x, u) \to (-x, u)$.

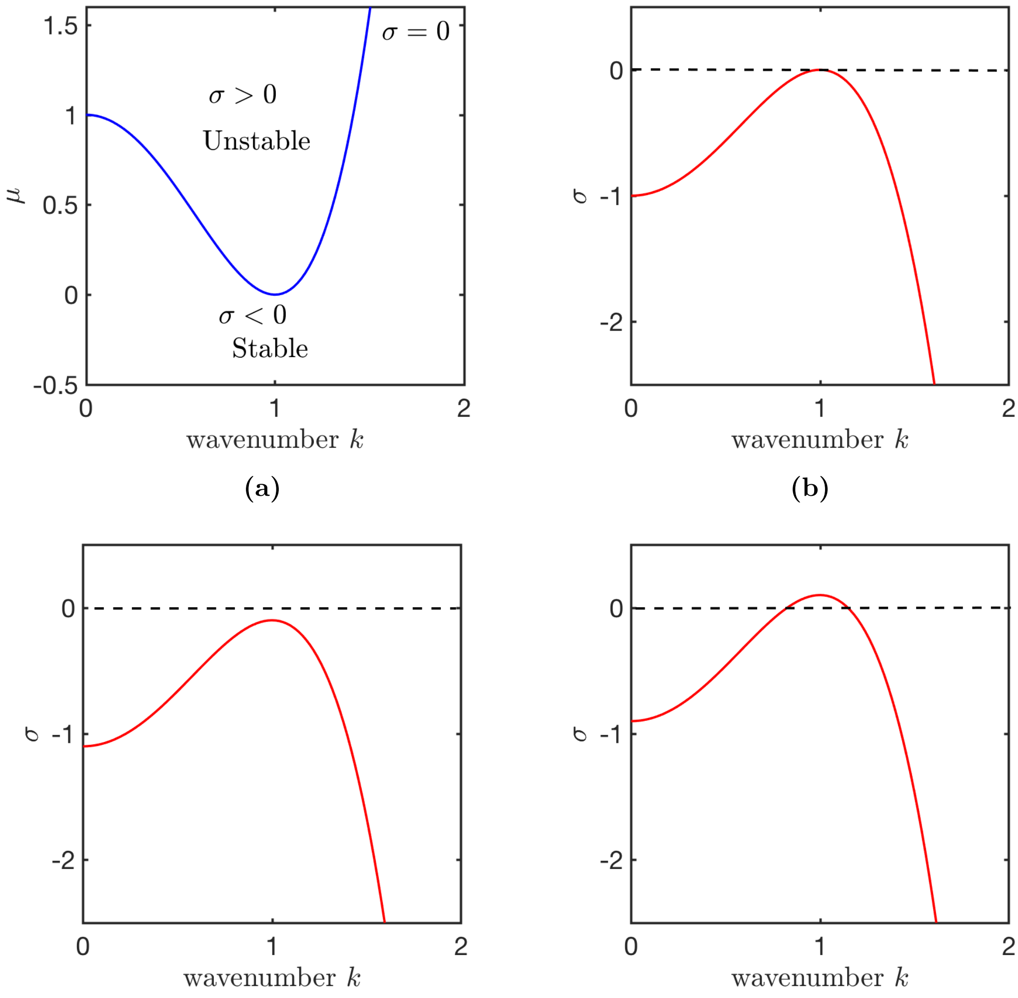

(a) **(b)** **(c)** **(d)**

Figure 1.3: (a) The marginal stability curve: graph of r against the wavenumber k from (1.25). (b,c,d) Sketch of the graph of $\sigma(k, r)$, (b) for $r = r_c = 0$, (c) $r = -0.1 < r_c$, (d) $r = 0.1 > r_c$ from (1.24).

The model with N_{35} has additional symmetry $(x, u) \to (x, -u)$. Therefore, the model with N_{35} is analogous to Rayleigh–Bénard convection with identical boundary conditions at the top and bottom while the quadratic term u^2 in N_{23} breaks this symmetry.

Applying weakly nonlinear theory, the Swift–Hohenberg equation can reduced to an equation for the amplitude $z(t)$:

$$\frac{dz}{dt} = rz - A|z|^2 z, \tag{1.26}$$

where $A = 3 - \frac{38}{9}b^2$ for N_{23} [20, 69] and $A = -3b$ for N_{35} [23]. When the system loses its stability at $r = 0$, the parameter b plays an important role in identifying the type of pattern-forming instability. It is supercritical if $b^2 < \frac{27}{38}$ for N_{23} and $b < 0$ for N_{35} and subcritical if $b^2 > \frac{27}{38}$ for N_{23} and $b > 0$ for N_{35}.

Although the Swift–Hohenberg equation cannot be directly derived from two-dimensional Rayleigh–Bénard convection, it captures many of the patterns observed in Rayleigh–Bénard convection near the critical Rayleigh number. In two dimensions, extended patterns such as rolls [41, 111], hexagons [118] and later spiral-defect chaos [117] have been found in investigations of the Swift–Hohenberg equation and its generalisations. The term "*extended pattern*" refers to a pattern that fills the domain (as in Figure 1.4 a). When considering nonlinear behaviour, the Swift–Hohenberg equation (1.22) (one PDE for a function of x and t) is much easier to analyse than the PDEs for Rayleigh–Bénard convection (two PDEs for two functions of x, z and t).

In the case of a subcritical pitchfork bifurcation, localized patterns have also been found in numerical investigations of the Swift–Hohenberg equation [15, 20–23, 25, 27, 29, 44, 47, 116]. The term "*localized pattern*" refers to a pattern that is found in one part of the domain while surrounded by the trivial state (as in Figure 1.4 b). Localized patterns have not been obtained in Rayleigh–Bénard convection partly because its pitchfork bifurcation is supercritical, but they do arise in other systems such as plane Couette flow [95], soft matter systems [100], time-dependent systems [2, 3, 119] and double-diffusive convection [11, 12, 74]. The Swift–Hohenberg equation is considered as a generic model of localized pattern formation.

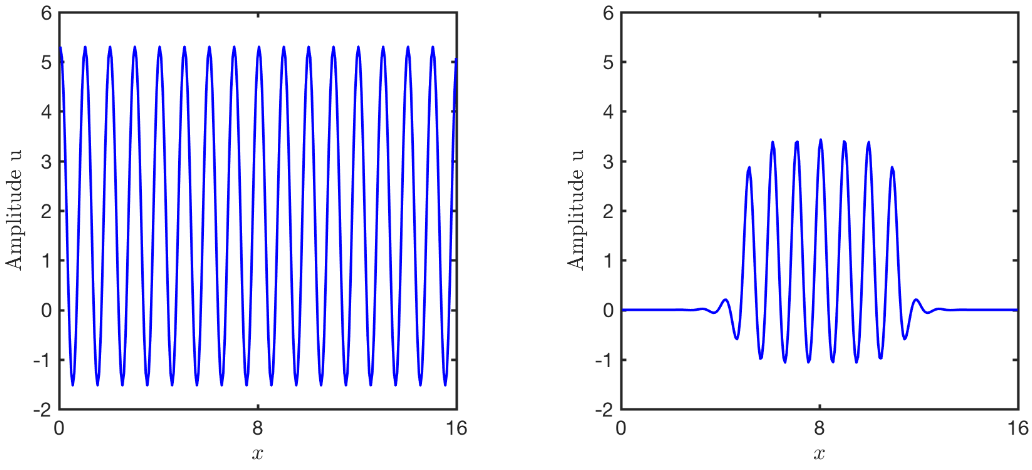

(a) **(b)**

Figure 1.4: Sample profiles of (a) extended steady state and (b) localized steady state solutions.

Indeed, the appearance of spatially localized steady states (LSS) can be understood in terms of the steady Swift–Hohenberg equation in one-dimension, treated as a fourth-order ordinary differential equation (ODE) in space [15, 20–23, 25, 27, 29, 44, 47, 116]

$$ru - (1 + \partial_{xx})^2 u + N(u; b) = 0. \tag{1.27}$$

The analysis shows that in bistable systems, localized states occur when the steady states (SS) pattern connects to the trivial state as $|x| \to \infty$. This indicates that the trivial state has both stable and unstable eigenvalues. These can be obtained from the linear problem of (1.27). The neutral stability curve of steady state solutions of the form $u = u_0 e^{\lambda x}$, is:

$$r = \left(1 + \lambda^2\right)^2, \tag{1.28}$$

where λ is the spatial eigenvalues of the trivial state $u_0 = 0$. Near $r = 0$ there

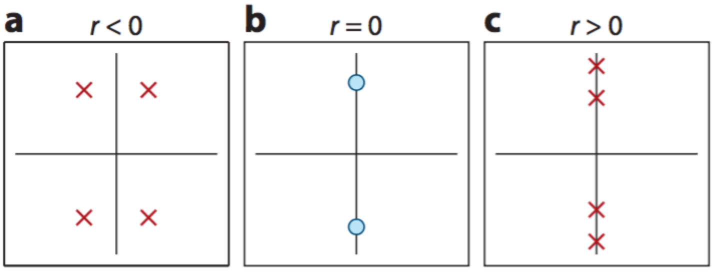

Figure 1.5: Spatial eigenvalues of the trivial state in the complex plane when (a) $r < 0$, (b) $r = 0$, and (c) $r > 0$ from [53].

are four spatial eigenvalues given by

$$\lambda = \pm i \pm \frac{\sqrt{-r}}{2} + O(r). \tag{1.29}$$

For $r < 0$, there are four eigenvalues with two positive and two negative real parts. This indicates that when $r < 0$ the amplitude of solutions close to the trivial state $u = 0$ will grow or decay. For $r > 0$, all the eigenvalues lie on the imaginary axis. At $r = 0$, there is a pair of imaginary eigenvalues ($\pm i$). The bifurcation at $r = 0$ is considered as a Hamiltonian–Hopf bifurcation in a reversible system since the four complex eigenvalues become pure imaginary as r passes through zero. Figure 1.5 shows the behaviour of spatial eigenvalues at a Hamiltonian–Hopf bifurcation.

The spatial analysis of localized states suggests that in a subcritical bifurcation and when the control parameter r is varied there are heteroclinic tangencies between the stable (W^s) and unstable (W^u) manifolds of a saddle-focus equilibrium (the trivial state O) and a saddle-type periodic state L (see Figure 1.6 and [25, 27, 44, 116]). At some point the unstable manifold $W^u(O)$ to the origin intersects with the stable manifold $W^s(O)$ leading to a homoclinic connection to the trivial state (Figure 1.6 b). At this point, the trajectories leave the trivial state as x increases from $-\infty$ and return to trivial state as $x \to \infty$ (as in Figure 1.4 b). There is an infinite number of different localized solutions in this region

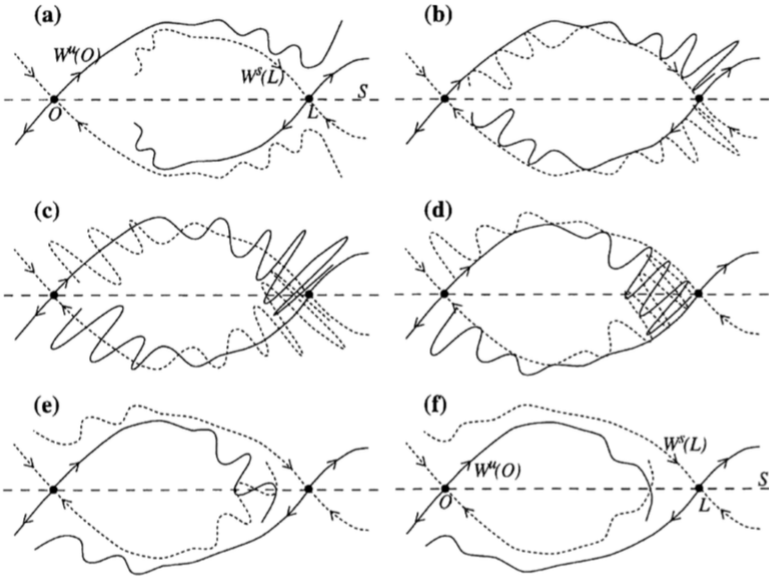

Figure 1.6: Illustrating graphic of the stable and unstable manifolds of the trivial state O and the periodic state L from [116]. The panels (a-f) show the heteroclinic tangencies between a saddle-focus point O and a saddle-type periodic orbit L as the bifurcation parameter r varies. The dashed and solid line indicate to the stable and unstable manifolds, respectively.

of heteroclinic tangencies (Figure 1.6 c), bounded between the first (Figure 1.6 b) and last (Figure 1.6 d) tangencies between the unstable manifold $W^u(O)$ to the origin and stable manifold $W^s(L)$ to the periodic state. This region is called the snaking region. Outside the snaking region, only a finite (possibly zero) number of localized states can be present.

This analysis is confirmed by solving the Swift–Hohenberg equation numerically. Figure 1.7 shows an example of localized states in the one dimensional Swift–Hohenberg equation with N_{23} nonlinearity from [18]. The figure shows a pair of branches of spatially localized states with odd L_0 and even L_1 number of peaks that bifurcate subcritically from the trivial state in a system of infinite domain. Both branches start with a small amplitude and with a large number of peaks. With decreasing the control parameter r, the localized solutions grow in amplitude and shrink in width. Each branch adds an oscillation on each side

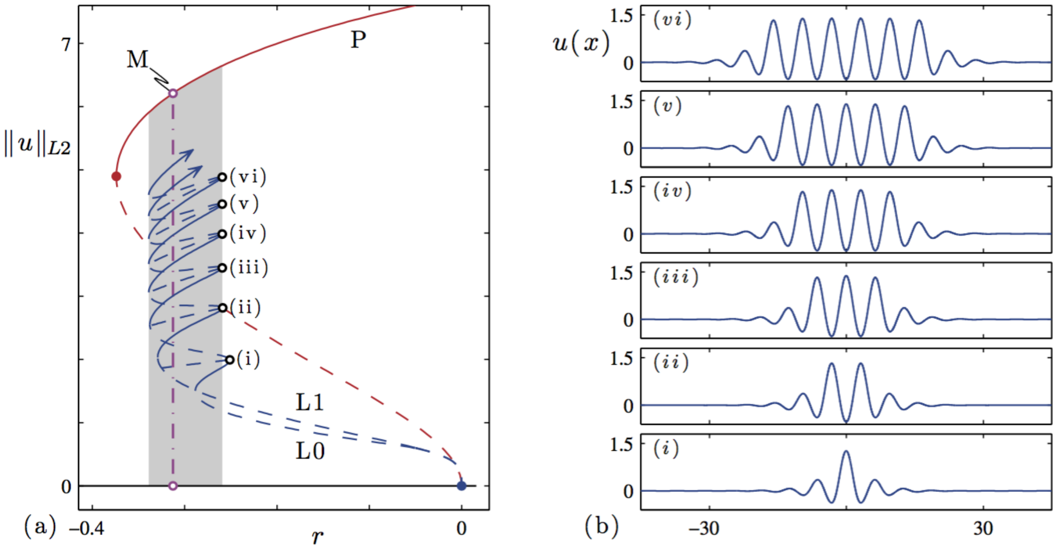

Figure 1.7: Bifurcation diagram showing the two homoclinic branches with odd L_0 and even L_1 peaks of the Swift–Hohenberg equation with the nonlinearities N_{23} from [18], where $b = 1.8$. P refers to the branch of spatially periodic patterns with the Maxwell point M, the value of r at which the flat and spatially periodic state have equal free energies. The right panel (b) shows several sizes of localized solutions along the two branches. The shaded region refers to the snaking region. The solid and dashed lines indicate stable and unstable solutions, respectively.

at each saddle-node bifurcation as it snakes back and forth producing homoclinic snaking. In a system of finite domain, both branches terminate at the saddle-node bifurcation of the subcritical periodic state with amplitude and width comparable to the periodic state [42].

Similar localized structures are found in the Swift–Hohenberg equation with the N_{35} nonlinearity [23]. Localized states are also obtained in the extended Swift–Hohenberg equation with nonlinearity that includes spatial derivatives such as $(u_x)^2$, $|u_{xx}|^2$, and uu_{xx} [18, 31, 64]. The bifurcation structure of localized states has also been explored in two-dimensional [67, 68] and three-dimensional investigations [73] of the Swift–Hohenberg equation. Localized spot and hexagon patches have been found [67, 68] in the two-dimensional Swift–Hohenberg equation.

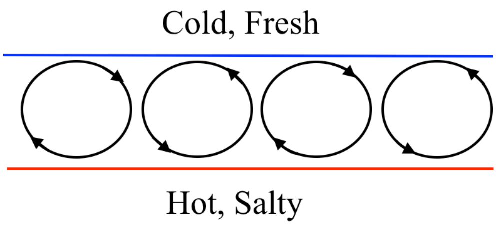

Figure 1.8: Schematic diagram of convection cells occurring in two-dimensional thermosolutal convection in a layer of fluid that is warm and salty on the bottom and cold and fresh on the top.

The aim of this dissertation is to understand the pattern-forming instability and localized patterns in convection systems that have two driving gradients; such systems are called double-diffusive convection. This is explained further in the next section.

1.3 Double-diffusive convection

In thermal convection, the fluid is driven by temperature gradients between the top and bottom layer, as we mentioned in Section 1.1. When the fluid is driven by two different gradients, it is called double-diffusive convection. The two gradients can be temperature and concentration in thermosolutal [33, 45, 78, 79, 99] and binary convection [52, 54, 112], or temperature and magnetic field in magnetoconvection [4, 26, 86, 92, 115].

Thermosolutal convection, for example, occurs in fluids subject to gradients both in temperature and solute in a layer of fluid that is warm and salty on the bottom and cold and fresh on the top (see Figure 1.8). Magnetoconvection occurs in electrically conducting fluids, such as the core of the Sun, that imposing a vertical magnetic field on a convecting layer. Depending on the strength of the gradients and the relative diffusivities, the convection patterns can be steady or oscillatory. In this dissertation, we focus on convection where steady flows and oscillations occur at the same critical wavenumber, as happens in thermosolutal and binary convection. In magnetoconvection [4, 26, 86, 92, 115] and rotating convection [109, 110, 121], a steady state and oscillation occur at different critical wavenumbers, which is more complicated. In the next section, we introduce the governing equations of thermosolutal and binary convection and implement a linear stability analysis.

1.3.1 Governing equations

We consider the non-dimensional PDEs governing two-dimensional Boussinesq convection in a binary convection (case B) [10, 52, 54, 112] and thermosolutal convection (case T) [33, 45, 77, 79, 82] in a layer of fluid heated from below, with the motion confined to a container of depth d in the z-direction and width L in the x-direction. We considering two-dimensional fluid that dependent on x and z only with no y-dependence and assuming that the fluid in incompressible based on Boussinesq approximation. Then the PDEs are expressed in terms of the equations of stream-function ψ (1.2), temperature perturbation θ and concentration Σ as follows:

$$\begin{aligned}
\frac{\partial \nabla^2 \psi}{\partial t} + J\left(\psi, \nabla^2 \psi\right) &= Pr \nabla^4 \psi + Pr Ra \frac{\partial \theta}{\partial x} + \begin{cases} -Pr Rs \frac{\partial \Sigma}{\partial x} & \text{case T,} \\ \\ Pr Ra S \frac{\partial \Sigma}{\partial x} & \text{case B,} \end{cases} \\
\frac{\partial \theta}{\partial t} + J(\psi, \theta) &= \frac{\partial \psi}{\partial x} + \nabla^2 \theta, \qquad\qquad (1.30) \\
\frac{\partial \Sigma}{\partial t} + J(\psi, \Sigma) &= \frac{\partial \psi}{\partial x} + \begin{cases} \zeta \nabla^2 \Sigma & \text{case T,} \\ \\ -\tau \nabla^2 \theta + \tau \nabla^2 \Sigma & \text{case B.} \end{cases}
\end{aligned}$$

The Laplacian ∇^2 and the Jacobian operator J are defined by (1.5) and (1.6). The variables in the governing equations are in dimensionless form; the x and

z are scaled by the depth d and time is scaled by $\frac{d^2}{\kappa}$, where κ is the thermal diffusivity. The temperature θ and concentration are scaled by the temperature difference $\Delta\theta$ and the concentration difference $\Delta\Sigma$. In fact, θ and Σ have a linear gradient subtracted off, so the true dimensionless temperature is $1 - z + \theta$ and concentration is $1 - z + \Sigma$. The dimensionless parameters in (1.30) are the Rayleigh number Ra and the Prandtl number Pr, given by (1.7), Rs and ζ are the solutal Rayleigh and Prandtl numbers, respectively

$$\begin{aligned} Rs &= \frac{g\beta\Delta\Sigma d^3}{\kappa\nu}, \\ \zeta &= \frac{\kappa_s}{\kappa}, \end{aligned} \tag{1.31}$$

S and τ are the separation ratio and Lewis number, respectively

$$\begin{aligned} S &= \frac{\beta\gamma_2}{D\alpha}, \\ \tau &= \frac{D}{\kappa}, \end{aligned} \tag{1.32}$$

where κ, κ_s and D are the thermal, solute, and concentration diffusivity, respectively, ν is the kinematic viscosity, g is the acceleration due to gravity, d is the fluid depth, β is the solutal expansion coefficient, γ_2 is the coefficient of the Soret effect and α is the coefficient of thermal expansion.

The momentum, heat and concentration in the governing equation (1.30) all diffuse and are transported by the fluid motion. The temperature gradients and concentration gradients in the momentum equation give rise to buoyancy forces. The separation ratio is a measure of the coupling between the temperature and concentration term and can take both positive and negative sign depending on the sign of the Soret effect [84]. The Soret effect is the ability of two mixtures to mix depending on the temperature. In the negative Soret effect case, thermal and concentration gradients are of opposite sign and since the thermal gradient is destabilizing the concentration gradient stabilizing, then the heavier component is condensed near the hotter boundary. The onset of convection then is driven by the temperature difference much greater than for a pure fluid Rayleigh–Bénard convection.

1.3.2 Boundary conditions

Similar to Rayleigh–Bénard convection, we solve the equations of convection system (1.30) in the region $(0 \leqslant x \leqslant L; 0 \leqslant z \leqslant 1)$ and we impose periodic boundary conditions appropriate to a cell of width L. Therefore, we consider stress-free boundary conditions for which no tangential stresses act on the surfaces with no flow and no heat and solutal flux through the sides of the boundary and the temperatures are fixed at the top $z = 1$ and bottom $z = 0$ boundaries. Therefore, we consider the following boundary condition

$$\begin{aligned}
\psi = 0 \quad & \text{at} \quad z = 0, \quad z = 1 \quad \text{and} \quad x = 0, \quad x = L,\\
\theta = \Sigma = 0 \quad & \text{at} \quad z = 0, \quad \text{and} \quad z = 1,\\
\frac{\partial^2 \psi}{\partial z^2} = 0 \quad & \text{at} \quad z = 0, \quad z = 1 \quad \text{and} \quad x = 0, \quad x = L,\\
\frac{\partial \theta}{\partial x} = \frac{\partial \Sigma}{\partial x} = 0 \quad & \text{at} \quad x = 0, \quad \text{and} \quad x = L.
\end{aligned} \tag{1.33}$$

With these boundary conditions the equations describing the two-dimensional convection (1.30) are equivariant with respect to reflections symmetry in a vertical plane, the Z_2 symmetry. The system also has a further symmetry, it is invariant under the transformation $(x, z, \psi, \theta, \Sigma) \to (x, 1 - z, -\psi, -\theta, -\Sigma)$ and $(x, z, \psi, \theta, \Sigma) \to (L - x, z, -\psi, -\theta, -\Sigma)$. The system described above has the static (conductive) solution $\psi = \theta = \Sigma = 0$.

1.3.3 Linear stability analysis

Let us consider the linear stability analysis of the above equations (1.30) by deleting all the nonlinearities and assuming the eigenfunctions of the linearized problem that satisfy the boundary conditions are

$$\begin{aligned}\psi(x,z,t) &= \psi_0 e^{\sigma t}\sin\frac{\pi x}{L}\sin\pi z,\\ \theta(x,z,t) &= \theta_0 e^{\sigma t}\cos\frac{\pi x}{L}\sin\pi z,\\ \Sigma(x,z,t) &= \Sigma_0 e^{\sigma t}\cos\frac{\pi x}{L}\sin\pi z,\end{aligned}\tag{1.34}$$

where σ is the growth rate that determines the stability of the system and $\frac{\pi}{L}$ is the horizontal wavenumber of the mode. By differentiating (1.34) and plugging into the PDEs (1.30), we get

$$\begin{aligned}\sigma\psi_0 a^2 &= -Pra^4\psi_0 + kPrRa\theta_0 + \begin{cases} -kPrRs\Sigma_0 & \text{case T,}\\ \\ kPrRaS\Sigma_0 & \text{case B,}\end{cases}\\ \sigma\theta_0 &= k\psi_0 - a^2\theta_0,\\ \sigma\Sigma_0 &= k\psi_0 + \begin{cases} -\zeta a^2\Sigma_0 & \text{case T,}\\ \\ +\tau a^2\theta_0 - \tau a^2\Sigma_0 & \text{case B.}\end{cases}\end{aligned}\tag{1.35}$$

This can be written in matrix form for thermosolutal convection as

$$\begin{pmatrix} \sigma a^2 + Pra^4 & -kRaPr & kPrRs \\ -k & \sigma + a^2 & 0 \\ -k & 0 & \sigma + \zeta a^2 \end{pmatrix}\begin{pmatrix}\psi_0\\ \theta_0\\ \Sigma_0\end{pmatrix} = \begin{pmatrix}0\\0\\0\end{pmatrix},\tag{1.36}$$

and for binary convection as

$$\begin{pmatrix} \sigma a^2 + Pra^4 & -kRaPr & -kRaPrS \\ -k & \sigma + a^2 & 0 \\ -k & -\tau a^2 & \sigma + \tau a^2 \end{pmatrix} \begin{pmatrix} \psi_0 \\ \theta_0 \\ \Sigma_0 \end{pmatrix} = \begin{pmatrix} 0 \\ 0 \\ 0 \end{pmatrix}, \tag{1.37}$$

where $a^2 = (k^2 + \pi^2)$, and $k = \frac{\pi}{L}$. The eigenvalues are obtained by setting the determinant to be zero which leads to the dispersion relation. In the thermosolutal case this is

$$\begin{aligned} \sigma^3 + a^2 \left(1 + \zeta + Pr\right) \sigma^2 + \Big(a^4 \left(\zeta + Pr\left(1 + \zeta\right)\right) - \tfrac{1}{a^2} \left(k^2 Pr \left(Ra - Rs\right)\right)\Big) \sigma \\ + \left(a^6 Pr\zeta - k^2 Pr \left(Ra\zeta - Rs\right)\right) = 0, \end{aligned} \tag{1.38}$$

and

$$\begin{aligned} \sigma^3 + a^2 \left(1 + \tau + Pr\right) \sigma^2 + \Big(a^4 \left(\tau + Pr\left(1 + \tau\right)\right) - \tfrac{1}{a^2} \left(k^2 RaPr \left(1 + S\right)\right)\Big) \sigma \\ + \left(a^6 Pr\tau - k^2 RaPr \left(\tau + S\left(\tau + 1\right)\right)\right) = 0 \end{aligned} \tag{1.39}$$

in the binary case. The dispersion relation (1.38) and (1.39) are cubic equations with real coefficients and there roots are either all real or have one real with complex-conjugate roots. The boundary of stability occurs when one of the roots equal zero (when $\sigma = 0$), gives the pitchfork bifurcation as follows:

$$Ra_{\mathrm{PF}} = \begin{cases} \frac{Rs}{\zeta} + Ra_0 & \text{case T}, \\ \\ \frac{\tau}{\tau + S(\tau+1)} Ra_0 & \text{case B}, \end{cases} \tag{1.40}$$

where

$$Ra_0 = \frac{a^6}{k^2}. \tag{1.41}$$

A Hopf bifurcation occurs when the pair of complex-conjugate roots cross the imaginary axis (when $\sigma = i\omega$). From the real and imaginary part, we get for the thermosolutal case

$$\begin{aligned} -a^2(1+\zeta+Pr)\omega^2 + a^6 Pr\zeta - k^2 Pr\,(Ra\zeta - Rs) &= 0, \qquad (1.42)\\ -\omega^3 + \left(a^4\,(\zeta + Pr\,(1+\zeta)) - \frac{1}{a^2}\left(k^2 Pr\,(Ra - Rs)\right)\right)\omega &= 0, \qquad (1.43) \end{aligned}$$

and for the binary case

$$\begin{aligned} -a^2(1+\tau+Pr)\omega^2 + a^6 Pr\tau - k^2 RaPr\,(\tau + S\,(\tau+1)) &= 0, \qquad (1.44)\\ -\omega^3 + \left(a^4\,(\tau + Pr\,(1+\tau)) - \frac{1}{a^2}\left(k^2 RaPr\,(1+S)\right)\right)\omega &= 0. \qquad (1.45) \end{aligned}$$

From (1.43) and (1.45), we get

$$\omega^2 = \begin{cases} a^4\Big[(\zeta + Pr\,(1+\zeta)) - \Big(\frac{Pr(Ra-Rs)}{Ra_0}\Big)\Big] \geq 0, & \text{case T,}\\[2ex] a^4\Big[(\tau + Pr\,(1+\tau)) - \Big(\frac{Pr(1+S)Ra}{Ra_0}\Big)\Big] \geq 0, & \text{case B,} \end{cases} \qquad (1.46)$$

where Ra_0 is given by (1.41). The system has a Hopf bifurcation which is found by substituting ω^2 in (1.42) for the thermosolutal case and in (1.44) for the binary case as follows:

$$Ra_{\text{Hopf}} = \begin{cases} \frac{\zeta+Pr}{1+Pr}Rs + \frac{(1+\zeta)(Pr+\zeta)}{Pr}Ra_0, & \text{case T,}\\[2ex] \frac{(1+\tau)(1+Pr)(\tau+Pr)}{Pr(1+Pr(1+S))}Ra_0, & \text{case B.} \end{cases} \qquad (1.47)$$

The Rayleigh number for the onset of convection is obtained by minimizing Ra with respect to k^2. In all cases, the wavenumber dependence comes only through Ra_0, which has a minimum value $\frac{27\pi^4}{4}$ at $k = k_c = \frac{\pi}{\sqrt{2}}$. Therefore, the critical numbers for the thermosolutal case are

$$\begin{aligned} Ra_{\mathrm{PF}} &= \frac{27\pi^4}{4} + \frac{Rs}{\zeta}, \\ Ra_{\mathrm{Hopf}} &= \frac{\zeta + Pr}{1 + Pr} Rs + \frac{27\pi^4}{4} \frac{(1+\zeta)(Pr+\zeta)}{Pr}. \end{aligned} \tag{1.48}$$

and

$$\begin{aligned} Ra_{\mathrm{PF}} &= \frac{27\pi^4}{4} \frac{\tau}{\tau + S\,(\tau+1)}, \\ Ra_{\mathrm{Hopf}} &= \frac{27\pi^4}{4} \frac{(1+\tau)\,(1+Pr)\,(\tau+Pr)}{Pr\,(1+Pr\,(1+S))} \end{aligned} \tag{1.49}$$

for the binary case. Linear stability analyses were considered by [5, 45] for thermosolutal convection and by [54] for binary convection. The analyses show that, when Rs and S are small, the first bifurcation as Ra increases is the pitchfork bifurcation, leading to steady patterns. The bifurcation changes to Hopf with oscillatory patterns when the second control parameter (the solutal Rayleigh number Rs in the thermosolutal case and the separation ratio S in the binary case) become stronger than a critical value (see Figure 1.9). The point where the bifurcation changes from steady to oscillatory is called the Taken–Bogdanov (TB) point. At this point, the pitchfork and Hopf bifurcations are coincident, and the system then has two zero eigenvalues when Ra reaches

$$\begin{aligned} Ra_{\mathrm{c}} =& \frac{(\zeta + Pr)}{Pr\,(1-\zeta)} Ra_0, \\ Rs_{\mathrm{c}} =& \frac{\zeta^2\,(1+Pr)}{Pr\,(1-\zeta)} Ra_0 \end{aligned} \tag{1.50}$$

for the thermosolutal case and

$$\begin{aligned} Ra_{\mathrm{c}} &= \frac{(\tau + Pr)}{Pr\,(1-\tau\,(1+S))} Ra_0, \\ S_{\mathrm{c}} &= \frac{-\tau^2\,(Pr+1)}{Pr + \tau\,(1+\tau)\,(Pr+1)} \end{aligned} \tag{1.51}$$

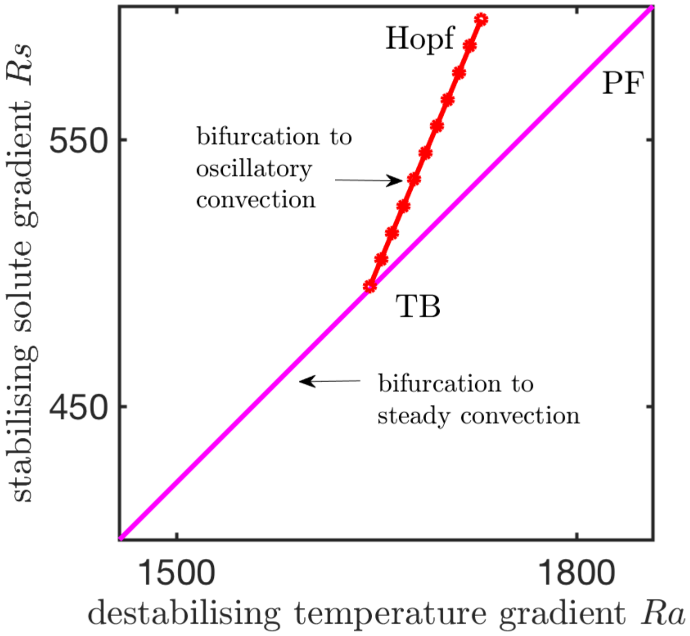

Figure 1.9: Unfolding diagram for the pitchfork (pink solid line) and Hopf (red line with star markets) in the (Ra, Rs)-plane from (1.48), when $\zeta = 0.5, Pr = 2$. At the co-dimension two Takens–Bogdanov point (TB), $(Ra_c, Rs_c) = (1647, 495)$, the Hopf and pitchfork bifurcations are coincident.

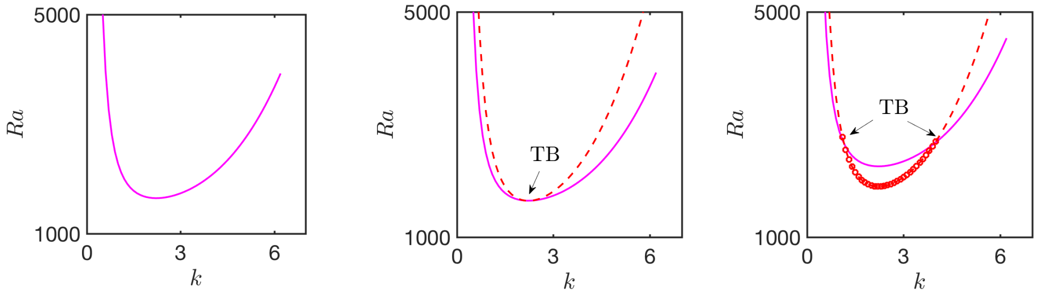

(a) $Rs < Rs_c$ **(b)** $Rs = Rs_c$ **(c)** $Rs > Rs_c$

Figure 1.10: Plot of the neutral stability curves for pitchfork and Hopf bifurcation from (1.40) and (1.47) for thermosolutal convection where $\zeta = 0.5, Pr = 2$. The pink solid line refers to the pitchfork bifurcation (the boundary of stability $\sigma = 0$), and the red circle line refers to the Hopf bifurcation where $\omega^2 \geq 0$. The dashed red line is the real eigenvalues of the Hopf bifurcation where $\omega^2 \leq 0$ and only pitchfork bifurcation exist. (a) $Rs < Rs_c$ where only the pitchfork exist, (b) $Rs = Rs_c = 495$ where the pitchfork and Hopf bifurcation are coincidence, and (c) $Rs > Rs_c$ where the pitchfork and Hopf bifurcation both exist.

in the binary case. Figure (1.10) shows the neutral stability curves for pitchfork and Hopf bifurcation for thermosolutal convection (a) for $Rs < Rs_c$ where only the pitchfork exist and (b) for $Rs = Rs_c$ where the pitchfork and Hopf bifurcation are coincidence at TB point, (c) for $Rs > Rs_c$ where the pitchfork and Hopf bifurcation both exist.

1.3.4 Nonlinear investigations

The nonlinear dynamics of double-diffusive convection has been of interest for many years. The nonlinear dynamics of double-diffusive convection is not fully understood due to the difficulty of the system. This difficulty inspired the idea of reducing the PDEs to a low order set of ordinary differential equations (ODEs) using a truncation method, which was introduced by [108]. The idea is to expand the variables of the state fluid in terms of a finite number of modes and substitute the expansion into the PDEs while neglecting the higher order nonlinearities. This leads to a fifth-order ODE that captures the qualitative features of the full system [56, 108]. Analytical investigations of the low order set of the thermosolutal problem show that the steady branch is subcritical and the oscillatory branch is supercritical and always terminates on the steady solution branch in a heteroclinic orbit (see Figure 5.1 a). These analytical results agree with the numerical results for the full PDEs system [33, 45, 77].

The low order set of ODEs are reduced further using weakly nonlinear theory [56], or perturbation theory [108] or centre-manifold theory [89] to the second order Van der Pol–Duffing equation [108]

$$\ddot{u} - u^3 - \lambda u = \epsilon\kappa\dot{u} + \epsilon N u^2 \dot{u} + O(\epsilon^2), \qquad \epsilon \ll 1, \tag{1.52}$$

where u is the amplitude of the lowest-order mode of the stream function, κ and λ are unfolding parameters, N is a constant, and the dot indicates the derivative with respect to time. The parameter ϵ controls how close the system is to the TB point. The equation (1.52) is the amplitude equation for two-dimensional double-diffusive convection with Z_2 symmetry. In the presence of periodic boundary conditions in the horizontal direction, the two-dimensional double-diffusive convection is invariant under the translations ($x \to x + d$), and invariant with respect to reflection symmetry in a vertical plane (the $O(2)$ symmetry). The system in this case is reduced to the Takens–Bogdanov normal form [34]

$$\ddot{Z} = \mu Z + A|Z|^2 Z + \epsilon\left(\nu\dot{Z} + C\left(\dot{Z}\bar{Z} + Z\dot{\bar{Z}}\right)Z + D|Z|^2\dot{Z}\right) + O(\epsilon^2), \qquad \epsilon \ll 1 \tag{1.53}$$

where Z is the complex amplitude of the pattern, μ and ν are the unfolding parameters, A, C and D are constants, the dot denotes differentiation with respect to time, and ϵ controls how close the system is to the TB point.

The linear part of the amplitude equation has two zero eigenvalues at the TB point. The amplitude equation is simple, which allows investigations of instability close to the onset of convection more easily than the full PDEs.

Different bifurcation scenarios obtained by the analysis of the amplitude equation are found close to onset [34, 52]. It is found that the oscillatory branch can bifurcate subcritically in a Hopf bifurcation. The analysis of the amplitude equation with $O(2)$ symmetry given by [34] can also distinguish the type of pattern: steady states (SS), travelling waves (TW), standing waves (SW) and modulated waves (MW). This is explained in more detail in Chapter 2. Extended TW, SW, and MW solutions have been found in the numerical investigations of thermosolutal convection [37, 98, 105]. A transition from SS to TW has been numerically discussed for the binary convection [7, 120]. Recently, a nonlinear SW solutions have been numerically obtained in binary convection [49, 72].

In the subcritical regime between the trivial state and the periodic SS, branches of LSS with homoclinic snaking have been obtained in numerical investigations of thermosolutal convection [12] and binary convection [11, 74, 75]. The snaking branches behave like those in the Swift–Hohenberg equation. At a given Rayleigh number, odd and even branch solutions of different widths can be found.

For binary convection, the system undergoes a subcritical Hopf bifurcation to TW for negative separation ratio S [62, 120]. In the parameter regime where the TW bifurcate subcritically from the conduction state, localized travelling waves (LTW) have also been obtained. The LTW solution refers to the spatially localized cells whose envelope moves with a characteristic speed in time with the surrounding trivial state. In contrast with LSS, the LTW have fixed and uniquely selected width, which was discovered in experimental [57, 59, 60, 83] and numerical [6, 8, 103] studies of binary convection, with a negative separation ratio $= -0.08$. This was also observed later in numerical simulations of the full system of binary convection with different but still small negative separation ratios $= -0.123$ [112] and -0.1 [120].

With different experimental parameters, LTW with different widths were also obtained by [6, 8, 101]. For separation ratio $S = -0.25$, the numerical investigation of the full system in [6] agreed with the experimental results obtained in a narrow annular box [101]. All the obtained LTW have the same amplitude and frequency, and they only differ slightly in the central part. The authors in [8] show numerical results from solving the full PDEs of binary convection at different scaled Rayleigh numbers $r = \frac{Ra}{Ra_c}$, with separation ratio $S = -0.25$. They found that in a narrow interval band of scaled Rayleigh numbers $(1.241 \leq r \leq 1.246)$, different LTW have different widths. For Rayleigh numbers above and below this interval the obtained LTW have fixed widths for the same parameter values.

The LTW branches are not easy to obtain numerically, as they are not translating version of an LSS. This is because the group velocity is not equal to the phase velocity in LTW solutions. The authors in [112–114] obtained a new numerical method which has two unknown variables: group velocity and temporal period, as well as other system parameters. They used the method of solving the PDEs of binary convection in the large but finite domain, and they found that the LTW branch does not snake while the LSS branches snake back and forth.

Moving localized steady states which are called moving convectons, have been found numerically in two-dimensional binary convection by [76]. In contract to LTW, the moving convectons have been obtained in a subcritical steady state and occur because the midplane reflection symmetry is broken by applying different boundary conditions at the top of the layer than at the bottom. While the LTW move because of a non-zero group speed and occur in a subcritical TW regime.

Other types of patterns such as undulating TW where the waves travel first to the left and then to the right, again and again, have been obtained recently in numerical investigations of binary convection [120]. Three-dimensional double-diffusive convection has been discussed numerically by [13, 14] where convection is driven by temperature and concentration differences imposed on a pair of opposite vertical boundaries. Two families of spatially localized steady states have been found in the subcritical bifurcation from the conduction state: a pair of primary branches that snake within a well-defined range of Rayleigh numbers and twisted convectons generate at the secondary snaking branches.

Overall, double-diffusive convection exhibits a variety of extended oscillation and localized patterns. So far, all the investigations that have been made in the PDE models of convection system, which is complicated and numerically expensive due to having to resolve the two PDEs for two functions of x, z and t. This led us to develop a new simple model similar to the Swift–Hohenberg equation. The model we aim to develop should replicate the linear behaviour of double-diffusive convection. Also, the linear part should reduce further to the Takens–Bogdanov equation, using weakly nonlinear analysis. The aim is to investigate the nonlinear behaviour near the Takens–Bogdanov point in a simple model which helps foster a better understanding. Numerically, the model should reproduce the same types of patterns which have been found in double-diffusive convection, including the extended and localized patterns.

1.4 Thesis outline

This dissertation has six chapters, including this one. In Chapter 2, we highlight some analysis obtained by [34] for the Takens–Bogdanov equation (1.53). This equation describes the behaviour of the solution near the onset of convection. The analysis obtained by [34] shows different bifurcation senarios and different types of solutions, including some related to the stability region. Therefore, this paper will be the basis for our investigations since we aim to attain the Takens–Bogdanov type solutions from the new model. We also show the derivation of the amplitude equation for the thermosolutal PDEs using a weakly nonlinear method.

In Chapter 3, we create the linear part of the model based on linear analysis of double-diffusive convection. Also, we discuss the nonlinearities which we can added to the model, taking into account Lyapunov stability and allowing up to two spatial derivatives. In this chapter, we choose simple nonlinearities $u^2, u^3, u^2 u_t$, and u_t^3 to simplify the model. The model reduces to the Takens–Bogdanov normal form equation after applying a weakly nonlinear analysis. When the model is reduced to the Taken–Bogdanov normal form, we are in a position to use the result obtained by [34]. The model with this choice of nonlinearities represents the case labelled II$-$ (with $A < 0$) in [34] in which only stable SS and TW exist (see Figures 3.6 and 4.3).

Although the linear part of the model captures the linear part of double-diffusive convection, we aim to make the model more generic to be relevant to other pattern-forming problems with a Takens–Bogdanov normal form. Therefore in Chapter 4, we extend our choice of nonlinearities to match many cases obtained by [34]. The new nonlinear term in this chapter is uu_{xx}, in addition to the previous nonlinearities in Chapter 3. These choices allow the model to match more cases obtained by the normal form [34], where the amplitude equation shows stable extended SW and MW as well as TW and SS. We numerically solve the model using the spectral method and the second order exponential time differencing (ETD) method. We show the stability region and the types of solutions for two cases labelled II− (with $A < 0$) and III− (with $A < 0$) in [34] (see Figures 4.4 and 4.5). We also compare the stability region and the types of solutions we obtained from numerical integrations with the stability region obtained by the normal form [34]. Numerically, we obtain the SS, TW and SW but not the MW, which only occur in the normal form in a narrow region between the half lines L_H (Hopf bifurcation of MW from TW) and L_{s2} (Hopf bifurcation of MW from SW) (see Figure 4.5).

In Chapter 5, we aim to obtain localized solutions from the model. The previous nonlinearities in Chapter 3 and 4 allow only supercritical bifurcations. In order to obtain the subcritical regime, we extend the nonlinearities further. By adding more nonlinearities $(u_x)^2u_t$ and uu_xu_{xt}, the model then allows subcritical bifurcation for the pitchfork and Hopf bifurcation branches. Thus, the model we consider in this dissertation with all nonlinearities is

$$\begin{aligned}\frac{\partial^2 u}{\partial t^2} &= \left(\mu - \left(1 + \frac{\partial^2}{\partial x^2}\right)^2\right) u + \left(\nu - b\left(1 + \frac{\partial^2}{\partial x^2}\right)^2\right)\frac{\partial u}{\partial t} \\ &\qquad + Q_1u^2 + Q_3uu_{xx} + C_1u^3 + C_2u^2u_t + C_4u_t^3 + C_5(u_x)^2u_t + C_6uu_xu_{tx}.\end{aligned} \tag{1.54}$$

where μ and ν are the control parameters and the coefficients $Q_1, Q_3, C_1, C_2, C_4, C_5$, and C_6 are constants, constrained only by Lyapunov stability. The coefficients Q_2 and C_3 for the terms u_t^2 and uu_t^2 have been dropped from the model (see Chapter

3 and Chapter 4).

The two cases we consider in Chapter 5 are labelled IV$-$ (with $A > 0$) and I$-$ (with $A < 0$) in [34] (see Figure 5.1). The case I$-$ (with $A < 0$) allows a subcritical SS branch from a pitchfork bifurcation, and the case IV$-$ (with $A > 0$) allows a subcritical TW branch from a Hopf bifurcation. We numerically solve the model in a small domain to check the stability and the type of solution compared with the normal form (see Figures 5.2, 5.3, 5.10 and 5.11). Then, we increase the domain size to obtain localized solutions.

In the case with a subcritical pitchfork bifurcation, we find a LSS with homoclinic snaking (see Figures 5.6, and 5.7) and isolated branches (see Figure 5.8) for two different distances from the onset of convection. The LSS branches are obtained by continuation using Newton iteration. The snaking behaves like the Swift–Hohenberg equation where the snaking region occurs away from the Hopf bifurcation band. However, in the absence of the saddle-node, the isolated branches start in the region where bistability can be observed between the trivial and periodic state to the region where the trivial state becomes unstable, passing the Hopf bifurcation point. A new type of localization is obtained in the region where the small-amplitude SW coexist with large-amplitude SS producing LSS with an MW background (see Figure 5.5 b).

In the case with a subcritical Hopf bifurcation, we find a LTW where the envelope structure changes with time (see Figure 5.12). All the LTW we find have the same width, regardless of initial conditions. In the region where the small-amplitude SS and large-amplitude TW coexist, we find LTW with SS backgrounds (see Figure 5.13).

Further discussion and conclusions are presented in Chapter 6.

Chapter 2

Takens–Bogdanov normal form

2.1 Introduction

The normal form that describes the amplitude behaviour near the onset of convection is called the Takens–Bogdanov (TB) equation. Close to the TB point, the bifurcation changes from a pitchfork bifurcation (leading to steady patterns) to a Hopf bifurcation (leading to oscillatory patterns) with the same wavenumber. The equations describing two-dimensional double-diffusive convection with periodic boundary conditions are equivariant under the $O(2)$ symmetry. In the $O(2)$ symmetry the system is invariant under translations ($x \to x + d$) for any constant d, and invariant with respect to reflection about $x = 0$. At a Hopf bifurcation, there are two solution branches bifurcating from the trivial state; travelling wave (TW) and standing wave (SW). In the absence of the translation symmetry, the symmetry group is Z_2 and only steady state (SS) and standing wave (SW) can occur [33, 55, 56].

The normal form equation that describes the nonlinear dynamics near the codimension-two bifurcation point for system with $O(2)$ symmetry has been discussed extensively by Dangelmayr and Knobloch (DK) [34]. Their analysis obtained a wide variety of states including: steady state (SS), travelling wave (TW), standing wave (SW), and modulated wave (MW) as well as the trivial state. The transitions and bifurcations between these states were also obtained. Since we aim to extend the Takens–Bogdanov problem, in this chapter we recall some relevant results from [34] in Section 2.2. We will not change notation in order to simplify the comparison later in Chapter 3, 4 and 5. In Section 2.4, we show the derivation of the normal form for the PDEs of thermosolutal convection with $O(2)$ symmetry using weakly nonlinear theory.

2.2 The analysis of the normal form

Throughout this section, we follow [34] closely. The normal form that describes the amplitude close to the TB point for a system with $O(2)$ symmetry is

$$\ddot{z} = \mu z + A|z|^2 z + \epsilon \left(\nu \dot{z} + C \left(\dot{z}\bar{z} + z\dot{\bar{z}}\right) z + D|z|^2 \dot{z}\right) + O(\epsilon^2), \qquad \epsilon \ll 1 \tag{2.1}$$

where $z(t)$ is the complex amplitude of the pattern, μ and ν are the unfolding parameters, A, C and D are constants, the dot denotes to differentiation with respect to time, ϵ controls how close the system is to the TB point. The fourth order normal form (2.1) can be reduced to third order by expressing z in terms of real variables (r, ϕ) as follows

$$z = re^{i\phi}. \tag{2.2}$$

Plugging (2.2) into (2.1) and taking the real and imaginary part, we get

$$\begin{aligned} \ddot{r} - r\dot{\phi}^2 &= \mu r + Ar^3 + \epsilon \left(\nu + Mr^2\right) \dot{r} + O(\epsilon^2), \\ r\ddot{\phi} + 2\dot{r}\dot{\phi} &= \epsilon \left(\nu + Dr^2\right) r\dot{\phi} + O(\epsilon^2), \end{aligned} \tag{2.3}$$

where $M = 2C + D$. Let us introduce the "*angular momentum*"

$$L = r^2\dot{\phi}. \tag{2.4}$$

Then (2.3) can be written as a third-order ODE as follows

$$\begin{aligned} \dot{r} &= s, \\ \dot{s} &= \mu r + Ar^3 + \frac{L^2}{r^3} + \epsilon\left(\nu + Mr^2\right)s + O(\epsilon^2), \\ \dot{L} &= \epsilon\left(\nu + Dr^2\right)L + O(\epsilon^2). \end{aligned} \tag{2.5}$$

Five types of solutions are found from (2.5), including SS, TW, SW and MW as well as the trivial state, as follows:

- **Trivial solution (T)**: The trivial solutions occur when r and L vanish ($z = 0$). Its stability is determined by the linearization of (2.1) resulting in a characteristic equation for the growth rate λ

  $$\lambda^2 - \epsilon\nu\lambda - \mu = 0. \tag{2.6}$$

  The pitchfork bifurcation occurs when one eigenvalue is zero along the line

  $$L_0 : \qquad \mu = 0, \tag{2.7}$$

  leading to SS solutions. A Hopf bifurcation occurs when eigenvalues are complex with zero real part, along the half line

  $$H_0 : \qquad \nu = 0, \ \mu < 0. \tag{2.8}$$

  leading to TW and SW solutions. The trivial solution is stable when μ and ν are both negative.

- **Steady states (SS)**: The steady state solutions occur when $r > 0$, $L = 0$, and there is no oscillation in the radial direction ($\dot{r} = s = \dot{L} = 0$) (see Figure 4.2 a). Thus from (2.5), the amplitude of SS solutions is

$$r_0 = \sqrt{\frac{-\mu}{A}}. \tag{2.9}$$

- **Travelling waves (TW)**: The travelling wave solutions occur when $r > 0$, $L \neq 0$, and there is no oscillation in the radial direction ($\dot{r} = s = 0$) (see Figure 4.2 b). The amplitude and frequency of the travelling wave solutions are constant. Since L and r are constants, $\dot{\phi}$ is constant, so travelling wave solutions have the form

$$z = r_0 e^{i\omega_0 t}, \tag{2.10}$$

where r_0 is the amplitude and $\dot{\phi} = \omega_0$ is the frequency. Substituting in the normal form equation (2.1), we get

$$-\omega_0^2 = \mu + i\nu\omega_0 + Ar_0^2 + i\omega_0 D r_0^2. \tag{2.11}$$

From the imaginary part the amplitude is

$$r_0 = \sqrt{\frac{-\nu}{D}}, \tag{2.12}$$

where the real part represents the frequency

$$\omega_0^2 = -\left(\mu + Ar_0^2\right). \tag{2.13}$$

- **Standing waves (SW)**: The standing wave solutions occur when $L = 0$, and there is an oscillation in the radial direction $\dot{r} \neq 0$ (see Figure 4.2 c).

- **Modulated waves (MW)**: The modulated wave solutions occur when $L \neq 0$, and there is an oscillation in the radial direction $\dot{r} \neq 0$. The modulated

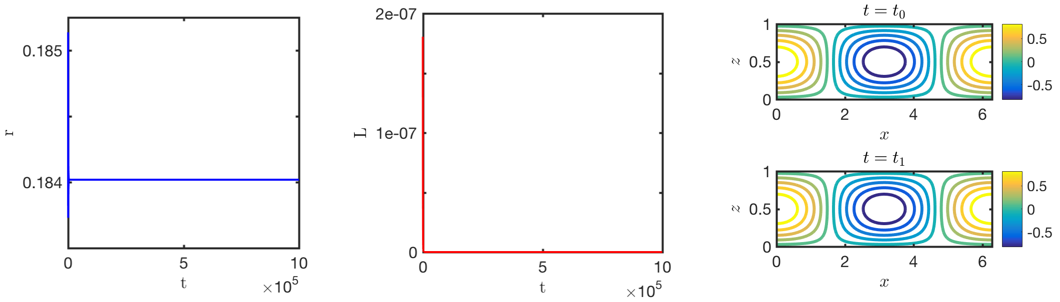

(a) Steady state

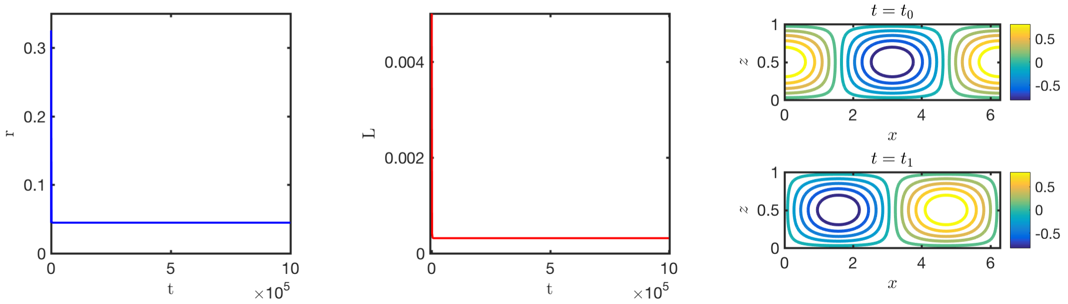

(b) Travelling wave

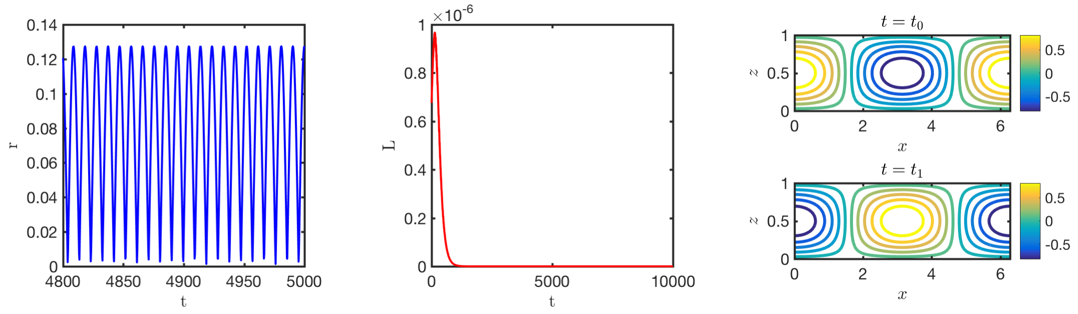

(c) Standing wave in the asymptotic state

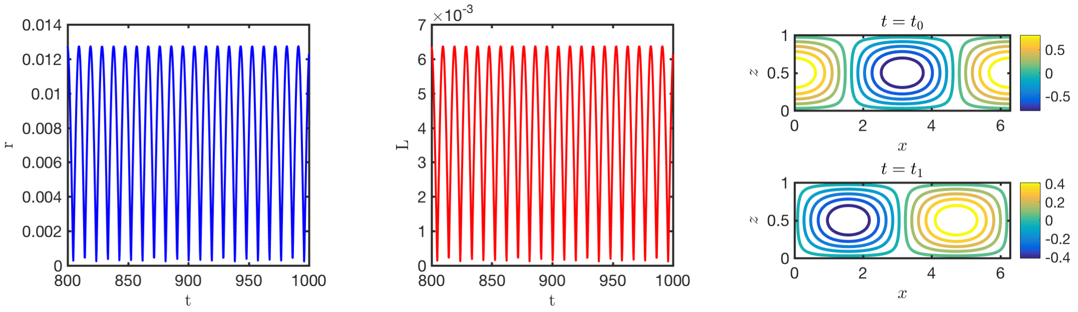

(d) Modulated wave in the asymptotic state

Figure 2.1: Sketch of the type of solutions for TB normal form (2.1) where the left-hand and middle panels represent r and L, respectively. The right-hand panels represent sketch of the stream-function in double-diffusive convection for each type of solutions.

wave solutions have two frequency one for orbital motion L and the other for radial oscillations r (see Figure 4.2 d).

The amplitude of SW and MW solutions can only be computed approximately close to the Hopf bifurcation but otherwise can be expressed in terms of elliptic integrals (see below) or can be found numerically.

DK [34] developed an approximation method based on averaging the equations in the limit of small ϵ, to reduced the dimension of the normal form further. They defined an "energy" E:

$$E = \frac{1}{2}s^2 + \frac{1}{2}\frac{L^2}{r^2} - \frac{1}{2}\mu r^2 - \frac{1}{4}Ar^4, \tag{2.14}$$

and found averaged equations for $\dot{E}$ and $\dot{L}$:

$$\dot{E} = \epsilon f(E, L^2) + O(\epsilon^2), \tag{2.15}$$

$$\dot{L} = \epsilon L g(E, L^2) + O(\epsilon^2), \tag{2.16}$$

where f, g are expressed as elliptic integrals. The averaging procedure reduced the third order ODEs in (r, s, L) to second order ODEs for the variables (E, L). The SW solutions were determined by the solutions of $f(E, 0) = 0$ with $L = 0$, while the MW solutions were determined by the solutions of $f(E, L^2) = 0 = g(E, L^2)$.

DK [34] also discussed the stability analysis for each type of solution in considerable detail. The bifurcation diagrams are divided into different regions depending on the value of the ratio $\frac{D}{M}$ (where $M = 2C + D$), as well as the sign of A (see Figure 2.2). For $A > 0$, they found four non-degeneracy conditions ($D \neq 0, M \neq 0, \frac{D}{M} \neq \frac{1}{2}$ and $\frac{D}{M} \neq \frac{1}{5}$) that divided the (M, D)-plane into eight regions. For $A < 0$, the (M, D)-plane divided into 18 different regions with the non-degeneracy conditions ($\frac{D}{M} \neq c$ where $c = 0, \frac{1}{2}, \frac{3}{5}, c \approx 0.7, 0.74, c = \frac{3}{4}, \frac{4}{5}, 1, \infty$).

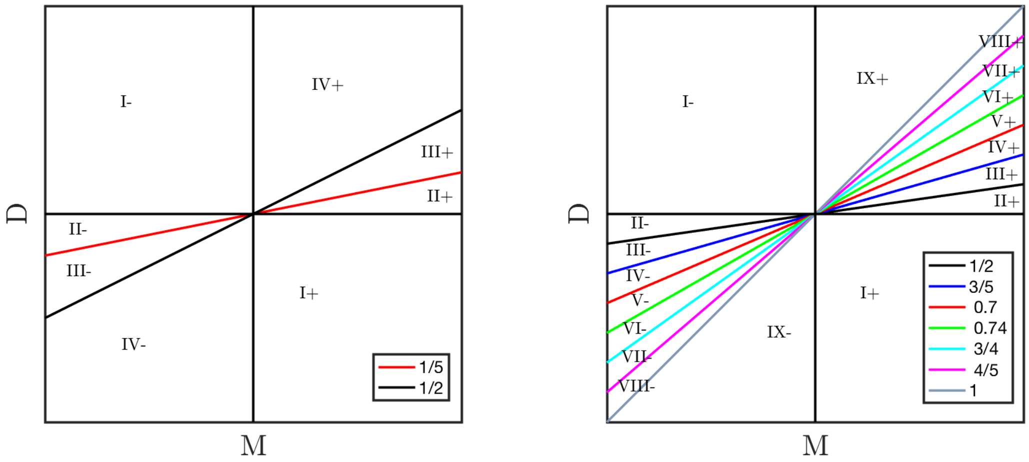

(a) $A > 0$ **(b)** $A < 0$

Figure 2.2: Division of (M, D)-plane from [34] with similar notation, (a) when $A > 0$ showing 8 regions and (b) when $A < 0$ showing 18 different regions.

The regions are labelled with roman numeral according to I$\pm -$ IX$\pm$ where $+$ and $-$ refers to the sign of M. Each region has a different bifurcation structure and possesses different types of solutions. In the next section, we recall the main bifurcation lines obtained by [34].

2.3 The bifurcations from DK

The SS solutions bifurcate from a pitchfork when $\mu = 0$, which is subcritical when $A > 0$ and supercritical when $A < 0$. The pitchfork bifurcation from SS to TW occur when

$$L_m : \qquad \mu = \frac{A}{D}\nu, \qquad \text{with} \qquad A\mu < 0. \tag{2.17}$$

When $A < 0$, a Hopf bifurcation from SS to SW can also occur. There are two type of SW solutions denoted by SW_2 and SW_3. In SW_2 the oscillations occur about the trivial state and in SW_3 the oscillations occur about the SS. The Hopf bifurcation from SS to SW$_3$ occurs when

$$L_M: \qquad \mu = \frac{A}{M}\nu, \qquad \text{with} \qquad \mu > 0, \qquad A < 0. \tag{2.18}$$

The SW$_2$ undergoes saddle node point at

$$SN_{s2}: \qquad \mu \approx \frac{A}{0.74M}\nu, \qquad \text{with} \qquad \mu > 0, \qquad A < 0, \tag{2.19}$$

and join smoothly to SW$_3$ in a gluing (homoclinic) bifurcation when

$$SL_s: \qquad \mu \approx \frac{5A}{4M}\nu, \qquad \text{with} \qquad \mu > 0. \tag{2.20}$$

When $A < 0$, a secondary bifurcation from SW$_2$ to MW occurs when

$$L_{S2}: \qquad \mu \approx \frac{A}{2D\left(\frac{\Phi(k)-k'}{k^2-k'^2}\right)}\nu, \qquad \text{with} \qquad \mu < 0, \qquad A < 0, \tag{2.21}$$

where k satisfies

$$\frac{D}{M} = \frac{-k'^2(1+k'^2) + 2(k'^2+k^4)\Phi(k)}{5(\Phi(k)-k'^2)(k'^2+(k^2-k'^2)\Phi(k))}, \tag{2.22}$$

with $k'^2 = 1 - k^2$ and $0 \leq k \leq 1$. The function $\Phi(k)$ is expressed as

$$\Phi(k) = \frac{\xi(k)}{\varkappa(k)},$$

where $\xi(k)$ and $\varkappa(k)$ are integrals given by

$$\begin{aligned} \xi(k) &= \int_{k'^2}^{1} \frac{\sigma d\sigma}{\sqrt{\sigma(\sigma-1)(\sigma-k'^2)}}, \\ \varkappa(k) &= \int_{k'^2}^{1} \frac{d\sigma}{\sqrt{\sigma(\sigma-1)(\sigma-k'^2)}}. \end{aligned} \tag{2.23}$$

For $A > 0$, the SW branch bifurcates from the Hopf bifurcation at $\nu = 0$, $\mu < 0$ and terminates on the subcritical SS branch in a heteroclinic bifurcation when

$$SL_s : \qquad \mu \approx \frac{5A}{M}\nu, \qquad\qquad \text{with} \qquad \mu < 0, \qquad A > 0. \tag{2.24}$$

The Hopf bifurcation from TW to MW occurs for both $A > 0$ and $A < 0$ when

$$L_H : \qquad \mu = \frac{3M - 5D}{2M - 4D}\frac{A}{D}\nu, \qquad\qquad \text{with} \qquad \mu < \frac{A}{D}\nu, \quad A > 0, \quad \text{or} \quad A < 0, \tag{2.25}$$

The notation here is similar to [34], to simplify comparisons later in this thesis. Cases labelled IV− with $A > 0$ and I−, II−, and III− with $A < 0$ from [34] are shown in Chapter 3, 4 and 5. For each case we show and discuss the bifurcation and stability diagrams separately.

Our interest in this dissertation is to model the Takens–Bogdanov primary bifurcation in two-dimensional double-diffusive convection problem. For this purpose, in the next section we show the derivation of the Takens–Bogdanov normal form for thermosolutal convection.

2.4 Derivation of the amplitude equation for thermosolutal convection

In this section, we derive the normal form equation for the PDEs for thermosolutal convection case (T) in (1.30) using weakly nonlinear analysis. We follow the method for a quite similar calculation for binary convection [52]. Similar to [52], we introduce a small parameter ϵ such that $Ra - Ra_c$, $Rs - Rs_c$ are both $O(\epsilon^2)$ and we expand the variable ψ, θ and Σ in power of small ϵ as will see below. We substitute the expansion into the governing equation and then we solve the leading order equations using Fredholm Alternative theorem when we have a solvability condition to obtain the amplitude equation which set at $O(\epsilon^4)$. However, the method we obtained is different from [52] where they used the iterative procedure by substituting the expansion into the governing equation and equating terms of the same spatial structure to obtain a set of ordinary differential equations and then seek a solution to the system as an expansion in powers of ϵ with ignoring the higher order term.

Recall the dimensionless equations for θ, Σ and ψ are:

$$\begin{aligned}\frac{\partial \nabla^2 \psi}{\partial t} + J\left(\psi, \nabla^2 \psi\right) &= Pr \nabla^4 \psi + Pr Ra \frac{\partial \theta}{\partial x} - Pr Rs \frac{\partial \Sigma}{\partial x},\\ \frac{\partial \theta}{\partial t} + J\left(\psi, \theta\right) &= \frac{\partial \psi}{\partial x} + \nabla^2 \theta,\\ \frac{\partial \Sigma}{\partial t} + J\left(\psi, \Sigma\right) &= \frac{\partial \psi}{\partial x} + \zeta \nabla^2 \Sigma,\end{aligned} \tag{2.26}$$

where Ra, Pr are the Rayleigh and Prandtl number given by (1.7), Rs and ζ are the solutal Rayleigh and Prandtl number given by (1.31), and J is the Jacobian operator defined by

$$J(f,g) = \frac{\partial f}{\partial x}\frac{\partial g}{\partial z} - \frac{\partial f}{\partial z}\frac{\partial g}{\partial x}. \tag{2.27}$$

We solve (2.26) in a horizontally layer subject to periodic boundary condition

$$\psi = \psi_{zz} = \theta = \Sigma = 0, \qquad \text{at} \qquad z = 0, 1, \tag{2.28}$$

and fixed temperature and concentration at the top and bottom boundary. Therefore, we seek spatially periodic solutions of horizontal period $L = \frac{2\pi}{k}$.

For simplicity, we write the system (2.26) in matrix form as follows

$$\frac{\partial}{\partial t}\begin{pmatrix} \nabla^2 \psi \\ \theta \\ \Sigma \end{pmatrix} = \begin{pmatrix} Pr\nabla^4 & PrRa\partial_x & -PrRs\partial_x \\ \partial_x & \nabla^2 & 0 \\ \partial_x & 0 & \zeta\nabla^2 \end{pmatrix}\begin{pmatrix} \psi \\ \theta \\ \Sigma \end{pmatrix} - \begin{pmatrix} J(\psi, \nabla^2\psi) \\ J(\psi, \theta) \\ J(\psi, \Sigma) \end{pmatrix},$$

For weakly nonlinear theory, we suppose Ra and Rs are close to the Takens–Bogdanov point (Ra_c, Rs_c) as follows

$$\begin{aligned} Ra &= Ra_0(a_c + \kappa\epsilon^2), \\ Rs &= Ra_0(s_c + \lambda\epsilon^2), \end{aligned} \tag{2.29}$$

where $Ra_c = Ra_0 a_c$, $Rs_c = Ra_0 s_c$ and a_c, s_c, Ra_0 given by

$$\begin{aligned} a_c &= \frac{(\zeta + Pr)}{Pr\,(1-\zeta)}, \\ s_c &= \frac{\zeta^2\,(1+Pr)}{Pr\,(1-\zeta)}, \\ Ra_0 &= \frac{(k^2+\pi^2)^3}{k^2} = \frac{p^3}{k^2}, \end{aligned} \tag{2.30}$$

where $p = (k^2 + \pi^2)$, with κ and λ are parameters of order 1 and $\epsilon^2 \ll 1$. The scaling of time is

$$\frac{\partial}{\partial t} \to \epsilon\frac{\partial}{\partial t}.$$

We expand ψ, θ and Σ in power of ϵ as follows:

$$\psi = \quad \epsilon\psi_1 + \epsilon^2\psi_2 + \epsilon^3\psi_3 + ..., \tag{2.31}$$

$$\theta = \quad \epsilon\theta_1 + \epsilon^2\theta_2 + \epsilon^3\theta_3 + ..., \tag{2.32}$$

$$\Sigma = \quad \epsilon\Sigma_1 + \epsilon^2\Sigma_2 + \epsilon^3\Sigma_3 + ... \tag{2.33}$$

Substituting these expansions into the PDEs, results in a series of equations at each order in ϵ. At $O(\epsilon)$, we get

$$\mathbf{L}\begin{pmatrix} \psi_1 \\ \theta_1 \\ \Sigma_1 \end{pmatrix} = \mathbf{0}, \tag{2.34}$$

where $\mathbf{L}$ refers to the linear part at the Takens–Bogdanov point:

$$\mathbf{L} = \begin{pmatrix} Pr\nabla^4 & \frac{p^3}{k^2}a_cPr\partial_x & -\frac{p^3}{k^2}s_cPr\partial_x \\ \partial_x & \nabla^2 & 0 \\ \partial_x & 0 & \zeta\nabla^2 \end{pmatrix}. \tag{2.35}$$

We assume solutions satisfy the boundary conditions with $O(2)$ symmetry as follows:

$$\begin{pmatrix} \psi_1 \\ \theta_1 \\ \Sigma_1 \end{pmatrix} = \begin{pmatrix} F_1 \\ F_2 \\ F_3 \end{pmatrix} e^{ikx}\sin(\pi z) + \begin{pmatrix} \bar{F_1} \\ \bar{F_2} \\ \bar{F_3} \end{pmatrix} e^{-ikx}\sin(\pi z). \tag{2.36}$$

where $F_1(t), F_2(t), F_3(t)$ and the complex conjugate $\bar{F_1}(t), \bar{F_2}(t), \bar{F_3}(t)$ are time-dependent amplitudes. Substituting (2.36) into (2.34), we get

$$\mathbf{L_0}\begin{pmatrix} F_1 \\ F_2 \\ F_3 \end{pmatrix} e^{ikx}\sin(\pi z) = \mathbf{0} \qquad \text{and} \qquad \bar{\mathbf{L}}_\mathbf{0}\begin{pmatrix} \bar{F_1} \\ \bar{F_2} \\ \bar{F_3} \end{pmatrix} e^{-ikx}\sin(\pi z) = \mathbf{0}, \tag{2.37}$$

where $\mathbf{L_0}$ and $\bar{\mathbf{L}}_\mathbf{0}$ are the linear operators

$$\mathbf{L_0} = \begin{pmatrix} p^2Pr & \frac{ip^3}{k}a_cPr & -\frac{ip^3}{k}s_cPr \\ ik & -p & 0 \\ ik & 0 & -p\zeta \end{pmatrix}, \ \bar{\mathbf{L}}_\mathbf{0} = \begin{pmatrix} p^2Pr & -\frac{ip^3}{k}a_cPr & \frac{ip^3}{k}s_cPr \\ -ik & -p & 0 \\ -ik & 0 & -p\zeta \end{pmatrix}. \tag{2.38}$$

From the second and third row of (2.37), we obtain

$$\begin{aligned} F_2 &= \frac{ik}{p}F_1 & \bar{F_2} &= \frac{-ik}{p}\bar{F_1}, \\ F_3 &= \frac{ik}{p\zeta}F_1 & \bar{F_3} &= \frac{-ik}{p\zeta}\bar{F_1}. \end{aligned} \tag{2.39}$$

Therefore, the solutions ψ_1, θ_1 and Σ_1 can be written as follows:

$$\begin{pmatrix} \psi_1 \\ \theta_1 \\ \Sigma_1 \end{pmatrix} = \begin{pmatrix} 1 \\ \frac{ik}{p} \\ \frac{ik}{p\zeta} \end{pmatrix} F_1 e^{ikx} \sin(\pi z) + \begin{pmatrix} 1 \\ \frac{-ik}{p} \\ \frac{-ik}{p\zeta} \end{pmatrix} \bar{F}_1 e^{-ikx} \sin(\pi z). \tag{2.40}$$

where $\begin{pmatrix} 1 \\ \frac{ik}{p} \\ \frac{ik}{p\zeta} \end{pmatrix} e^{ikx} \sin(\pi z)$ and $\begin{pmatrix} 1 \\ \frac{-ik}{p} \\ \frac{-ik}{p\zeta} \end{pmatrix} e^{-ikx} \sin(\pi z)$ are eigenvectors of $\mathbf{L_0}$ and $\bar{\mathbf{L}}_\mathbf{0}$, respectively. Thus, (2.37) becomes

$$\mathbf{L_0} \begin{pmatrix} 1 \\ \frac{ik}{p} \\ \frac{ik}{p\zeta} \end{pmatrix} F_1 e^{ikx} \sin(\pi z) = \mathbf{0}, \qquad \text{and} \qquad \bar{\mathbf{L}}_\mathbf{0} \begin{pmatrix} 1 \\ \frac{-ik}{p} \\ \frac{-ik}{p\zeta} \end{pmatrix} \bar{F}_1 e^{-ikx} \sin(\pi z) = \mathbf{0}. \tag{2.41}$$

The linear operators $\mathbf{L_0}$ and $\bar{\mathbf{L}}_\mathbf{0}$ have two zero eigenvalues, and at a later stage in the calculation, we need the associated generalized eigenvector $\begin{pmatrix} w_1 \\ w_2 \\ w_3 \end{pmatrix}$ which is found by solving

$$\mathbf{L_0} \begin{pmatrix} w_1 \\ w_2 \\ w_3 \end{pmatrix} = \begin{pmatrix} 1 \\ \frac{ik}{p} \\ \frac{ik}{p\zeta} \end{pmatrix} e^{ikx} \sin(\pi z), \tag{2.42}$$

along with its complex conjugate. From the second and third row, we get

$$\begin{aligned} w_2 &= \frac{ik}{p} w_1 - \frac{ik}{p^2} e^{ikx} \sin(\pi z), \\ w_3 &= \frac{ik}{p\zeta} w_1 - \frac{ik}{(p\zeta)^2} e^{ikx} \sin(\pi z). \end{aligned} \tag{2.43}$$

For simplicity, we choose $w_1 = 0$. Then the generalized eigenvector of $\mathbf{L_0}$ is

$$\begin{pmatrix} w_1 \\ w_2 \\ w_3 \end{pmatrix} = \begin{pmatrix} 0 \\ -\frac{ik}{p^2} \\ -\frac{ik}{(p\zeta)^2} \end{pmatrix} e^{ikx}\sin(\pi z), \tag{2.44}$$

At $O(\epsilon^2)$, we get

$$\mathbf{L}\begin{pmatrix} \psi_2 \\ \theta_2 \\ \Sigma_2 \end{pmatrix} = \frac{\partial}{\partial t}\begin{pmatrix} \nabla^2\psi_1 \\ \theta_1 \\ \Sigma_1 \end{pmatrix} + \begin{pmatrix} \psi_{1_x}\nabla^2\psi_{1_z} - \psi_{1_z}\nabla^2\psi_{1_x} \\ \psi_{1_x}\theta_{1_z} - \psi_{1_z}\theta_{1_x} \\ \psi_{1_x}\Sigma_{1_z} - \psi_{1_z}\Sigma_{1_x} \end{pmatrix}. \tag{2.45}$$

We can separate (2.45) and solve the time derivative and the nonlinear parts separately. From (2.40), we obtain the nonlinear part as follows:

$$\mathbf{L}\begin{pmatrix} \psi_2 \\ \theta_2 \\ \Sigma_2 \end{pmatrix} = 2\begin{pmatrix} 0 \\ \frac{\pi k^2}{p} \\ \frac{\pi k^2}{p\zeta} \end{pmatrix} |F_1|^2\sin(2\pi z). \tag{2.46}$$

We note that, the nonlinear terms are functions of z only. Therefore, we assume ψ_2, θ_2 and Σ_2 are function of z only:

$$\psi_2 = \psi_2(z),\ \theta_2 = \theta_2(z),\ \Sigma_2 = \Sigma_2(z). \tag{2.47}$$

From the second and third row in (2.46) and by integrating θ_2 and Σ_2 twice with respect to z, we get ψ_2, θ_2 and Σ_2 from the nonlinear part as follows:

$$\begin{pmatrix} \psi_2 \\ \theta_2 \\ \Sigma_2 \end{pmatrix} = -\frac{1}{2}\begin{pmatrix} 0 \\ \frac{k^2}{\pi p} \\ \frac{k^2}{\pi p\zeta^2} \end{pmatrix} |F_1|^2\sin(2\pi z). \tag{2.48}$$

From the generalized eigenvector (2.44) and the nonlinear part (2.48) we can write the solution at $O(\epsilon^2)$ as follows:

$$\begin{aligned}\begin{pmatrix}\psi_2\\ \theta_2\\ \Sigma_2\end{pmatrix} &= \begin{pmatrix}0\\ \frac{-ik}{p^2}\\ \frac{-ik}{(p\zeta)^2}\end{pmatrix}\frac{\partial F_1}{\partial t}e^{ikx}\sin(\pi z) + \begin{pmatrix}0\\ \frac{ik}{p^2}\\ \frac{ik}{(p\zeta)^2}\end{pmatrix}\frac{\partial \bar{F}_1}{\partial t}e^{-ikx}\sin(\pi z)\\ &\quad -\frac{1}{2}\begin{pmatrix}0\\ \frac{k^2}{\pi p}\\ \frac{k^2}{\pi p\zeta^2}\end{pmatrix}|F_1|^2\sin(2\pi z)\\ &\quad +\begin{pmatrix}1\\ \frac{ik}{p}\\ \frac{ik}{p\zeta}\end{pmatrix}G_1e^{ikx}\sin(\pi z) + \begin{pmatrix}1\\ \frac{-ik}{p}\\ \frac{-ik}{p\zeta}\end{pmatrix}\bar{G}_1e^{-ikx}\sin(\pi z),\end{aligned} \tag{2.49}$$

where $G_1(t)$ and the complex conjugate $\bar{G}_1(t)$ are time-dependent amplitudes. In many calculations the G_1 term could be set to zero, but this problem requires going to fourth order, so we include $G_1(t) \neq 0$ here.

At $O(\epsilon^3)$, we get

$$\mathbf{L}\begin{pmatrix}\psi_3\\ \theta_3\\ \Sigma_3\end{pmatrix} = \frac{\partial}{\partial t}\begin{pmatrix}\nabla^2\psi_2\\ \theta_2\\ \Sigma_2\end{pmatrix} - \frac{p^3}{k^2}Pr\begin{pmatrix}\kappa\theta_{1_x} - \lambda\Sigma_{1_x}\\ 0\\ 0\end{pmatrix} + \begin{pmatrix}\psi_{1_x}\nabla^2\psi_{2_z} - \psi_{1z}\nabla^2\psi_{2_x}\\ \psi_{1_x}\theta_{2_z} - \psi_{1_z}\theta_{2_x}\\ \psi_{1_x}\Sigma_{2_z} - \psi_{1_z}\Sigma_{2_x}\end{pmatrix}. \tag{2.50}$$

From (2.40) and (2.49), we get

$$\mathbf{L}\begin{pmatrix}\psi_3\\ \theta_3\\ \Sigma_3\end{pmatrix} = \begin{pmatrix}0\\ \frac{-ik}{p^2}\\ \frac{-ik}{(p\zeta)^2}\end{pmatrix}\frac{\partial^2 F_1}{\partial t^2}e^{ikx}\sin(\pi z) + \begin{pmatrix}0\\ \frac{ik}{p^2}\\ \frac{ik}{(p\zeta)^2}\end{pmatrix}\frac{\partial^2 \bar{F}_1}{\partial t^2}e^{-ikx}\sin(\pi z)$$

$$
\begin{aligned}
&-\begin{pmatrix} 0 \\ \frac{k^2\pi}{p^2}+\frac{k^2}{2p\pi} \\ \frac{k^2\pi}{p^2\zeta^2}+\frac{k^2}{2p\pi\zeta^2} \end{pmatrix}\left(F_1\frac{\partial \bar{F}_1}{\partial t}+\bar{F}_1\frac{\partial F_1}{\partial t}\right)\sin(2\pi z) \\
&+\begin{pmatrix} 1 \\ \frac{ik}{p} \\ \frac{ik}{p\zeta} \end{pmatrix}\frac{\partial G_1}{\partial t}e^{ikx}\sin(\pi z)+\begin{pmatrix} 1 \\ \frac{-ik}{p} \\ \frac{-ik}{p\zeta} \end{pmatrix}\frac{\partial \bar{G}_1}{\partial t}e^{-ikx}\sin(\pi z) \\
&-\begin{pmatrix} 0 \\ \frac{ik^3}{2p} \\ \frac{ik^3}{2p\zeta^2} \end{pmatrix}F_1^2\bar{F}_1e^{ikx}\left(\sin(3\pi z)-\sin(\pi z)\right) \\
&+\begin{pmatrix} 0 \\ \frac{ik^3}{2p} \\ \frac{ik^3}{2p\zeta^2} \end{pmatrix}\bar{F_1}^2F_1e^{-ikx}\left(\sin(3\pi z)-\sin(\pi z)\right) \\
&+\begin{pmatrix} 0 \\ \frac{\pi k^2}{p} \\ \frac{\pi k^2}{p\zeta} \end{pmatrix}\left(F_1\bar{G}_1+\bar{F}_1G_1\right)\sin(2\pi z) \\
&-\begin{pmatrix} p^2Pr(\kappa-\frac{\lambda}{\zeta}) \\ 0 \\ 0 \end{pmatrix}F_1e^{ikx}\sin(\pi z)-\begin{pmatrix} p^2Pr(\kappa-\frac{\lambda}{\zeta}) \\ 0 \\ 0 \end{pmatrix}\bar{F}_1e^{-ikx}\sin(\pi z).
\end{aligned}
\tag{2.51}
$$

For simplicity, we write the last equation as follows:

$$\mathbf{L}V_3 = RHS, \tag{2.52}$$

where $\mathbf{L}$ is the linear operator given by (2.35), V_3 is the eigenvector $\begin{pmatrix} \psi_3 \\ \theta_3 \\ \Sigma_3 \end{pmatrix}$ and RHS refers to the right-hand side of equation (2.51), which includes time derivatives and nonlinearities. There is a solvability condition needed to solve this equation. Applying the Fredholm Alternative theorem [65], we need the adjoint linear operator $\mathbf{L}^\dagger$. First, we define an inner product between two function f and g by

$$\langle \mathbf{f}(x,z), \mathbf{g}(x,z) \rangle = \frac{1}{L}\int_0^1 \int_0^L \bar{\mathbf{f}}(x,z)\mathbf{g}(x,z)dx\,dz, \tag{2.53}$$

where $\bar{\mathbf{f}}$ is the complex conjugate of $\mathbf{f}$ and L is the spatial domain ($L = \frac{2\pi}{k}$). The adjoint operator $\mathbf{L}^\dagger$, requiring that

$$\langle \mathbf{f}, \mathbf{L}\mathbf{g} \rangle = \langle \mathbf{L}^\dagger \mathbf{f}, \mathbf{g} \rangle \tag{2.54}$$

for all $\mathbf{f}$ and $\mathbf{g}$ where

$$\mathbf{f} = \begin{pmatrix} f_1 \\ f_2 \\ f_3 \end{pmatrix}, \qquad \mathbf{g} = \begin{pmatrix} g_1 \\ g_2 \\ g_3 \end{pmatrix}. \tag{2.55}$$

Applying the inner product to solve

$$\langle \mathbf{f}, \mathbf{L}\mathbf{g} \rangle = \langle \begin{pmatrix} f_1 \\ f_2 \\ f_3 \end{pmatrix}, \begin{pmatrix} Pr\nabla^4 & \frac{p^3}{k^2}a_c Pr\partial_x & -\frac{p^3}{k^2}s_c Pr\partial_x \\ \partial_x & \nabla^2 & 0 \\ \partial_x & 0 & \zeta\nabla^2 \end{pmatrix} \begin{pmatrix} g_1 \\ g_2 \\ g_3 \end{pmatrix} \rangle,$$

we obtain

$$\begin{aligned} \langle \mathbf{f}, \mathbf{L}\mathbf{g} \rangle = \frac{1}{L}\int_0^1 \int_0^L \Big[\bar{f}_1 \left(Pr\nabla^4 g_1 + \frac{p^3}{k^2}a_c Pr\partial_x g_2 - \frac{p^3}{k^2}s_c Pr\partial_x g_3 \right) \\ + \bar{f}_2 \left(\partial_x g_1 + \nabla^2 g_2 \right) + \bar{f}_3 \left(\partial_x g_1 + \zeta\nabla^2 g_3 \right) \Big] \, dx\,dz. \end{aligned} \tag{2.56}$$

For the terms with Laplacian operator ∇^2 we apply the Green's second order identity:

$$\int_D \left(\bar{f}_i \nabla^2 g_i - g_i \nabla^2 \bar{f}_i \right) dV = \int_c \left(\bar{f}_i \nabla g_i - g_i \nabla \bar{f}_i \right) \cdot \mathbf{n}\, ds, \qquad i = 2, 3, \tag{2.57}$$

and similarly

$$\int_D \left(\bar{f}_1 \nabla^4 g_1 - g_1 \nabla^4 \bar{f}_1\right) dV = \int_c \left(\bar{f}_1 \nabla^2 g_1 - g_1 \nabla^2 \bar{f}_1\right) \cdot \mathbf{n}\, ds, \tag{2.58}$$

where c the boundary of D and $\mathbf{n}$ is the outward pointing unit normal of surface element ds and by integrating the integral of the form $\int_0^1 \int_0^L \bar{f} \partial_x g\, dx\, dz$ by part with respect to x, we get

$$\int_0^L \bar{f} \partial_x g\, dx = \bar{f} g|_0^L - \int_0^L g \partial_x \bar{f}\, dx. \tag{2.59}$$

Sine the functions $\mathbf{f}$ and $\mathbf{g}$ satisfy the periodic boundary condition (2.28) then the right-hand side of (2.57) and (2.58) and the first term of the right-hand side of (2.59) will vanish and then (2.56) becomes

$$\begin{aligned} \langle \mathbf{f}, \mathbf{L}\mathbf{g} \rangle = \frac{1}{L} \int_0^1 \int_0^L \Big[& \left(Pr g_1 \nabla^4 \bar{f}_1 - \frac{p^3}{k^2} a_c Pr g_2 \partial_x \bar{f}_1 + \frac{p^3}{k^2} s_c Pr g_3 \partial_x \bar{f}_1 \right) \\ & + \left(-g_2 \partial_x \bar{f}_2 + g_2 \nabla^2 \bar{f}_2 \right) + \left(-g_1 \partial_x \bar{f}_3 + \zeta g_3 \nabla^2 \bar{f}_3 \right) \Big]\, dx\, dz, \end{aligned} \tag{2.60}$$

which can be written using the inner product as following

$$\langle \begin{pmatrix} Pr\nabla^4 & -\partial_x & -\partial_x \\ -\frac{p^3}{k^2} a_c Pr \partial_x & \nabla^2 & 0 \\ \frac{p^3}{k^2} s_c Pr \partial_x & 0 & \zeta \nabla^2 \end{pmatrix} \begin{pmatrix} f_1 \\ f_2 \\ f_3 \end{pmatrix}, \begin{pmatrix} g_1 \\ g_2 \\ g_3 \end{pmatrix} \rangle = \langle \mathbf{L}^\dagger \mathbf{f}, \mathbf{g} \rangle,$$

where

$$\mathbf{L}^\dagger = \begin{pmatrix} Pr\nabla^4 & -\partial_x & -\partial_x \\ -\frac{p^3}{k^2} a_c Pr \partial_x & \nabla^2 & 0 \\ \frac{p^3}{k^2} s_c Pr \partial_x & 0 & \zeta \nabla^2 \end{pmatrix}. \tag{2.61}$$

Based on the Fredholm Alternative theorem, if there exist a nontrivial solution to the homogenous equation $\mathbf{L}^\dagger V^\dagger = 0$, then the original equation (2.51) has a solution only if

$$\begin{aligned}\langle V^\dagger, \mathbf{L}V_3\rangle =& \langle V^\dagger, RHS\rangle && (2.62)\\ =& \langle \mathbf{L}^\dagger V^\dagger, V_3\rangle = 0 && (2.63)\end{aligned}$$

where $V^\dagger$ is the adjoint eigenvector. In this problem, we have two independent eigenvectors

$$\begin{pmatrix} F_1 \\ F_2 \\ F_3 \end{pmatrix} e^{ikx}\sin(\pi z) \qquad \text{and} \qquad \begin{pmatrix} \bar{F}_1 \\ \bar{F}_2 \\ \bar{F}_3 \end{pmatrix} e^{-ikx}\sin(\pi z). \tag{2.64}$$

and two adjoint eigenvectors as follows:

$$V^\dagger = \begin{pmatrix} \psi^\dagger \\ \theta^\dagger \\ \Sigma^\dagger \end{pmatrix} = \begin{pmatrix} F_1^\dagger \\ F_2^\dagger \\ F_3^\dagger \end{pmatrix} e^{-ikx}\sin(\pi z), \qquad \text{and} \qquad \bar{V}^\dagger = \begin{pmatrix} \bar{\psi}^\dagger \\ \bar{\theta}^\dagger \\ \bar{\Sigma}^\dagger \end{pmatrix} = \begin{pmatrix} \bar{F_1}^\dagger \\ \bar{F_2}^\dagger \\ \bar{F_3}^\dagger \end{pmatrix} e^{ikx}\sin(\pi z). \tag{2.65}$$

By solving $\mathbf{L}^\dagger V^\dagger = 0$, we get

$$V^\dagger = \begin{pmatrix} \psi^\dagger \\ \theta^\dagger \\ \Sigma^\dagger \end{pmatrix} = \begin{pmatrix} 1 \\ \frac{ip^2}{k} a_c Pr \\ \frac{-ip^2}{\zeta k} s_c Pr \end{pmatrix} e^{-ikx}\sin(\pi z). \tag{2.66}$$

Now, we impose

$$\langle V^\dagger, \mathbf{L}V_3\rangle = \langle V^\dagger, RHS\rangle = 0, \tag{2.67}$$

to obtain the amplitude equation at third order of ϵ as follows

$$\frac{\partial^2 F_1}{\partial t^2} = \frac{pk^2}{2} F_1^2 \bar{F}_1 - p^2 N F_1 - R\frac{\partial G_1}{\partial t}. \tag{2.68}$$

where

$$\begin{aligned} N &= \frac{\kappa - \frac{\lambda}{\zeta}}{a_c - \frac{s_c}{\zeta^3}}, \\ R &= 1 - pa_cPr + pPr\frac{s_c}{\zeta^2}. \end{aligned} \tag{2.69}$$

From (2.30) the coefficients N and R can be written in term of Prandtl number Pr and solutal Prandtl number ζ as follows:

$$\begin{aligned} N &= \frac{Pr(\lambda - \zeta\kappa)}{Pr + \zeta + 1}, \\ R &= \frac{1+p}{Pr + \zeta + 1}. \end{aligned} \tag{2.70}$$

The normal form (2.1) has terms $|F_1|\frac{\partial F_1}{\partial t}$ and $F_1^2\frac{\partial \bar{F}_1}{\partial t}$ which are not in the third order amplitude equation. Therefore, we need to go to fourth order in ϵ. This requires to determine V_3, so we assume V_3 as follows:

$$\begin{aligned} V_3 = \begin{pmatrix} \psi_3 \\ \theta_3 \\ \Sigma_3 \end{pmatrix} &= \begin{pmatrix} H_1 \\ H_2 \\ H_3 \end{pmatrix} e^{ikx}\sin(\pi z) + \begin{pmatrix} \bar{H}_1 \\ \bar{H}_2 \\ \bar{H}_3 \end{pmatrix} e^{-ikx}\sin(\pi z) \\ &+ \begin{pmatrix} 0 \\ Q_2 \\ Q_3 \end{pmatrix} \sin(2\pi z) + \begin{pmatrix} 0 \\ R_2 \\ R_3 \end{pmatrix} e^{ikx}\sin(3\pi z) + \begin{pmatrix} 0 \\ \bar{R}_2 \\ \bar{R}_3 \end{pmatrix} e^{-ikx}\sin(3\pi z). \end{aligned} \tag{2.71}$$

Then, we obtain $\mathbf{L}V_3$ as follows:

$$\begin{aligned} \mathbf{L}V_3 = &\begin{pmatrix} p^2Pr & \frac{ip^3}{k}a_cPr & -\frac{ip^3}{k}s_cPr \\ ik & -p & 0 \\ ik & 0 & -p\zeta \end{pmatrix} \begin{pmatrix} H_1 \\ H_2 \\ H_3 \end{pmatrix} e^{ikx}\sin(\pi z) \\ + &\begin{pmatrix} p^2Pr & -\frac{i}{k}p^3a_cPr & \frac{ip^3}{k}s_cPr \\ -ik & -p & 0 \\ -ik & 0 & -p\zeta \end{pmatrix} \begin{pmatrix} \bar{H}_1 \\ \bar{H}_2 \\ \bar{H}_3 \end{pmatrix} e^{-ikx}\sin(\pi z) \end{aligned}$$

$$
\begin{aligned}
&+\begin{pmatrix} 0 & 0 & 0 \\ 0 & -4\pi^2 & 0 \\ 0 & 0 & -\pi^2\zeta \end{pmatrix}\begin{pmatrix} 0 \\ Q_2 \\ Q_3 \end{pmatrix}\sin(2\pi z) \\
&+\begin{pmatrix} 0 & \frac{ip^3}{k}a_cPr & -\frac{i}{k}p^3 s_c Pr \\ 0 & -(k^2+9\pi^2) & 0 \\ 0 & 0 & -(k^2+9\pi^2)\zeta \end{pmatrix}\begin{pmatrix} 0 \\ R_2 \\ R_3 \end{pmatrix} e^{ikx}\sin(3\pi z) \\
&+\begin{pmatrix} 0 & -\frac{ip^3}{k}a_cPr & s_cPr\frac{ip^3}{k} \\ 0 & -(k^2+9\pi^2) & 0 \\ 0 & 0 & -\zeta-(k^2+9\pi^2) \end{pmatrix}\begin{pmatrix} 0 \\ \bar{R}_2 \\ \bar{R}_3 \end{pmatrix} e^{-ikx}\sin(3\pi z). \qquad (2.72)
\end{aligned}
$$

By comparing the coefficient of $e^{ikx}\sin(\pi z)$ and $e^{-ikx}\sin(\pi z)$ from (2.51) and (2.72), we have

$$
\begin{pmatrix} H_1 \\ H_2 \\ H_3 \end{pmatrix} = \begin{pmatrix} 0 \\ \frac{ik}{p^3} \\ \frac{ik}{p^3\zeta^3} \end{pmatrix}\frac{\partial^2 F_1}{\partial t^2} - \begin{pmatrix} 0 \\ \frac{ik^3}{2p^2} \\ \frac{ik^3}{2p^2\zeta^3} \end{pmatrix} F_1^2\bar{F}_1 - \begin{pmatrix} 0 \\ \frac{ik}{p^2} \\ \frac{ik}{p^2\zeta^2} \end{pmatrix}\frac{\partial G_1}{\partial t}, \qquad (2.73)
$$

and

$$
\begin{pmatrix} \bar{H}_1 \\ \bar{H}_2 \\ \bar{H}_3 \end{pmatrix} = -\begin{pmatrix} 0 \\ \frac{ik}{p^3} \\ \frac{ik}{\tau^3p^3} \end{pmatrix}\frac{\partial^2 \bar{F}_1}{\partial t^2} + \begin{pmatrix} 0 \\ \frac{ik^3}{2p^2} \\ \frac{ik^3}{2p^2\zeta^3} \end{pmatrix} \bar{F}_1{}^2 F_1 + \begin{pmatrix} 0 \\ \frac{ik}{p^2} \\ \frac{ik}{p^2\zeta^2} \end{pmatrix}\frac{\partial \bar{G}_1}{\partial t}. \qquad (2.74)
$$

By comparing the coefficient of $\sin(2\pi z)$, we get

$$
\begin{pmatrix} 0 \\ Q_2 \\ Q_3 \end{pmatrix} = \begin{pmatrix} 0 \\ \frac{1}{4\pi^2}\left(\frac{k^2\pi}{p^2}+\frac{k^2}{2p\pi}\right) \\ \frac{1}{4\pi^2}\left(\frac{k^2\pi}{p^2\zeta^2}+\frac{k^2}{2p\pi\zeta^2}\right) \end{pmatrix}\left(F_1\frac{\partial \bar{F}_1}{\partial t}+\bar{F}_1\frac{\partial F_1}{\partial t}\right) - \begin{pmatrix} 0 \\ \frac{k^2}{4\pi p} \\ \frac{k^2}{4\zeta^2\pi p} \end{pmatrix}\left(F_1\bar{G}_1+\bar{F}_1G_1\right). \qquad (2.75)
$$

By comparing the coefficient of $e^{ikx}\sin(3\pi z)$ and $e^{-ikx}\sin(3\pi z)$, we get

$$\begin{pmatrix} 0 \\ R_2 \\ R_3 \end{pmatrix} = \begin{pmatrix} 0 \\ \frac{ik^3}{2p(k^2+9\pi^2)} \\ \frac{ik^3}{2\zeta^3 p(k^2+9\pi^2)} \end{pmatrix} F_1^2 \bar{F}_1, \tag{2.76}$$

and

$$\begin{pmatrix} 0 \\ \bar{R}_2 \\ \bar{R}_3 \end{pmatrix} = - \begin{pmatrix} 0 \\ \frac{ik^3}{2p(k^2+9\pi^2)} \\ \frac{ik^3}{2\zeta^3 p(k^2+9\pi^2)} \end{pmatrix} \bar{F_1}^2 F_1. \tag{2.77}$$

From the term that fourth order in ϵ, we have

$$\mathbf{L} \begin{pmatrix} \psi_4 \\ \theta_4 \\ \Sigma_4 \end{pmatrix} = \frac{\partial}{\partial t} \begin{pmatrix} \nabla^2 \psi_3 \\ \theta_3 \\ \Sigma_3 \end{pmatrix} - \frac{p^3}{k^2} Pr \begin{pmatrix} \kappa \partial_x \theta_2 - \lambda \partial_x \Sigma_2 \\ 0 \\ 0 \end{pmatrix} + \begin{pmatrix} \psi_{1x} \nabla^2 \psi_{3z} - \psi_{1z} \nabla^2 \psi_{3_x} \\ \psi_{1x} \theta_{3_z} - \psi_{1_z} \theta_{3_x} \\ \psi_{1_x} \Sigma_{3_z} - \psi_{1_z} \Sigma_{3_x} \end{pmatrix}. \tag{2.78}$$

At fourth order of ϵ, the normal form can be obtained from imposing the solvability condition $\langle V^\dagger, \mathbf{L} V_4 \rangle = 0$, which only involves the coefficient of $e^{ikx}\sin(\pi z)$. Therefore in next equation we only show the terms with the coefficient $e^{ikx}\sin(\pi z)$

as follows:

$$
\begin{aligned}
\mathbf{L}\begin{pmatrix}\psi_4\\ \theta_4\\ \Sigma_4\end{pmatrix} = \Bigg[& \begin{pmatrix}0\\ \frac{ik}{p^3}\\ \frac{ik}{p^3\zeta^3}\end{pmatrix}\frac{\partial^3 F_1}{\partial t^3} - \begin{pmatrix}0\\ \frac{ik^3}{2p^2}\\ \frac{ik^3}{2p^2\zeta^3}\end{pmatrix}(2|F_1|^2\frac{\partial F_1}{\partial t} + F_1^2\frac{\partial \bar{F}_1}{\partial t}) \\
& - \begin{pmatrix}0\\ \frac{ik}{p^2}\\ \frac{ik}{p^2\zeta^2}\end{pmatrix}\frac{\partial^2 G_1}{\partial t^2} - \begin{pmatrix}pPr(\kappa - \frac{\lambda}{\zeta^2})\frac{\partial F_1}{\partial t} - p^2 Pr(\kappa - \frac{\lambda}{\zeta})G_1\\ 0\\ 0\end{pmatrix} \\
& - \begin{pmatrix}0\\ \frac{ik}{4\pi}\left(\frac{k^2\pi}{p^2} + \frac{k^2}{2p\pi}\right)\\ \frac{ik}{4\pi}\left(\frac{k^2\pi}{p^2\zeta^2} + \frac{k^2}{2p\pi\zeta^2}\right)\end{pmatrix}\left(F_1^2\frac{\partial \bar{F}_1}{\partial t} + |F_1|^2\frac{\partial F_1}{\partial t}\right) \\
& - \begin{pmatrix}0\\ \frac{ik^3}{4p}\\ \frac{k^2}{4p\zeta^2}\end{pmatrix}\left(F_1^2\bar{G}_1 + |F_1|^2 G_1\right)\Bigg] e^{ikx}\sin(\pi z).
\end{aligned}
\tag{2.79}
$$

Applying the inner product $\langle V^{\dagger}, \mathbf{L}V_4\rangle = 0$, we have the amplitude equation

$$
\begin{aligned}
\frac{\partial^2 G_1}{\partial t^2} = & -p^2 N G_1 + \frac{1}{p}S\frac{\partial^3 F_1}{\partial t^3} + pB\frac{\partial F_1}{\partial t} - \frac{k^2}{2}S\left(2|F_1|^2\frac{\partial F_1}{\partial t} + F_1^2\frac{\partial \bar{F}_1}{\partial t}\right) \\
& - \frac{k^2}{4}(1 + \frac{p}{2\pi^2})S\left(|F_1|^2\frac{\partial F_1}{\partial t} + F_1^2\frac{\partial \bar{F}_1}{\partial t}\right) + \frac{k^2 p}{4}\left(F_1^2\bar{G}_1 + |F_1|^2 G_1\right).
\end{aligned}
\tag{2.80}
$$

where N is given by (2.69), and B and S are

$$
\begin{aligned}
B &= \frac{(\kappa - \frac{\lambda}{\zeta^2})}{(a_c - \frac{s_c}{\zeta^3})}, \\
S &= \frac{(a_c - \frac{s_c}{\zeta^4})}{(a_c - \frac{s_c}{\zeta^3})}.
\end{aligned}
\tag{2.81}
$$

From (2.30) the coefficients B and S can be written in term of Prandtl number

Pr and solutal Prandtl number ζ as follows:

$$\begin{aligned} B &= \frac{Pr\,(\lambda-\zeta^2\kappa)}{\zeta\,(Pr+\zeta+1)}, \\ S &= 1+\frac{Pr+1}{\zeta\,(Pr+\zeta+1)}. \end{aligned} \tag{2.82}$$

To eliminate the third derivative $\frac{\partial^3 F_1}{\partial t^3}$ from (2.80), we differentiate (2.68) with respect to t to get

$$\frac{\partial^3 F_1}{\partial t^3} = \frac{pk^2}{2}\left(2|F_1|^2\frac{\partial F_1}{\partial t} + F_1^2\frac{\partial \bar{F}_1}{\partial t}\right) - p^2 N\frac{\partial F_1}{\partial t} - R\frac{\partial^2 G_1}{\partial t^2}. \tag{2.83}$$

By substituting (2.83) in (2.80), we get

$$\begin{aligned} \frac{\partial^2 G_1}{\partial t^2} = &-\frac{k^2}{4}S(1+\frac{p}{2\pi^2})\left(|F_1|^2\frac{\partial F_1}{\partial t} + F_1^2\frac{\partial \bar{F}_1}{\partial t}\right) + p(B-SN)\frac{\partial F_1}{\partial t} \\ &- p^2 N G_1 + \frac{k^2 p}{4}\left(F_1^2\bar{G}_1 + |F_1|^2 G_1\right) - \frac{1}{p}SR\frac{\partial^2 G_1}{\partial t^2}, \end{aligned} \tag{2.84}$$

which can be written in the form

$$\begin{aligned} \frac{\partial^2 G_1}{\partial t^2} = &-\frac{k^2}{4}\frac{S}{1+\frac{1}{p}SR}(1+\frac{p}{2\pi^2})\left(|F_1|^2\frac{\partial F_1}{\partial t} + F_1^2\frac{\partial \bar{F}_1}{\partial t}\right) + p\frac{B-SN}{1+\frac{1}{p}SR}\frac{\partial F_1}{\partial t} \\ &- p^2\frac{N}{1+\frac{1}{p}SR}G_1 + \frac{k^2 p}{4}\frac{1}{1+\frac{1}{p}SR}\left(F_1^2\bar{G}_1 + |F_1|^2 G_1\right), \end{aligned} \tag{2.85}$$

We want to combine the equations (2.68) and (2.85) to one equation, the normal form equation, by using a reconstitution procedure [91]. We assume

$$z = \epsilon F_1 + \epsilon^2 G_1, \tag{2.86}$$

and unscale time and the parameters in (2.68) and (2.85) according to

$$\frac{\partial}{\partial t} \to \frac{1}{\epsilon}\frac{\partial}{\partial t}\ \kappa \to \frac{1}{\epsilon^2}\kappa \ \text{ and } \lambda \to \frac{1}{\epsilon^2}\lambda. \tag{2.87}$$

Note here that κ and λ appear in (2.68) and (2.85) through the coefficients N (2.70), and B (2.82). Then we get

$$\begin{aligned}\frac{\partial^2 z}{\partial t^2} &= -p^2 N F_1 + \epsilon^3 \frac{p}{2} k^2 F_1^2 \bar{F}_1 - \epsilon^2 R \frac{\partial G_1}{\partial t} + \epsilon p \frac{B - SN}{1 + \frac{1}{p} SR} \frac{\partial F_1}{\partial t} \\ &- \epsilon^3 \frac{k^2}{4} \frac{S}{1 + \frac{1}{p} SR} (1 + \frac{p}{2\pi^2}) \left(|F_1|^2 \frac{\partial F_1}{\partial t} + F_1^2 \frac{\partial \bar{F}_1}{\partial t} \right) \\ &- \epsilon^2 p^2 \frac{N}{1 + \frac{1}{p} SR} G_1 + \epsilon^4 \frac{k^2 p}{4} \frac{1}{1 + \frac{1}{p} SR} \left(F_1^2 \bar{G}_1 + |F_1|^2 G_1 \right).\end{aligned} \tag{2.88}$$

Substituting $F_1 = \frac{z}{\epsilon} - \epsilon G_1$, in equation (2.88) and neglecting all the terms of order ϵ, we get the Takens–Bogdanov normal form

$$\frac{\partial^2 z}{\partial t^2} = -p^2 N z + \frac{p}{2} k^2 |z|^2 z + p \frac{B - SN}{1 + \frac{1}{p} SR} \frac{\partial z}{\partial t} - \frac{k^2}{4} \frac{S}{1 + \frac{1}{p} SR} (1 + \frac{p}{2\pi^2}) \left(\bar{z} \frac{\partial z}{\partial t} + z \frac{\partial \bar{z}}{\partial t} \right) z. \tag{2.89}$$

To reduce the parameters in last equation we scale time and z as follows

$$\frac{\partial}{\partial t} \to p \frac{\partial}{\partial t} \qquad z \to \frac{\sqrt{2p}}{k} z. \tag{2.90}$$

With this scaling the amplitude equation (2.90) becomes

$$\frac{\partial^2 z}{\partial t^2} = -N z + |z|^2 z + \frac{B - SN}{1 + \frac{1}{p} SR} \frac{\partial z}{\partial t} - \frac{1}{2} (1 + \frac{2}{\varpi}) \frac{S}{1 + \frac{1}{p} SR} \left(\bar{z} \frac{\partial z}{\partial t} + z \frac{\partial \bar{z}}{\partial t} \right) z. \tag{2.91}$$

where

$$\varpi = \frac{4\pi^2}{p}, \tag{2.92}$$

N and R are given by (2.70), and B and S are given by (2.82).

Comparing the coefficients of the normal form obtained from thermosolutal convection (2.91) with the normal from (2.1) discussed by [34], we get

$$\begin{aligned}
\mu &= -N,\\
\nu &= \frac{B - SN}{1 + \frac{1}{p}SR},\\
A &= 1,\\
C &= -\frac{1}{2}\left(1 + \frac{2}{\varpi}\right)\frac{S}{1 + \frac{1}{p}SR},\\
D &= 0.
\end{aligned} \tag{2.93}$$

We note that the coefficient D vanishes in the amplitude equation of thermosolutal convection (2.91). This coefficient controls the amplitude of TW solutions as we mentioned in Section 2.2. Having $D = 0$, the normal form becomes degenerate which require higher order terms in the weakly nonlinear analysis. Furthermore, the term D also vanishes for two-dimensional Boussinesq convection in binary convection [52, 54]. This issue is discussed by [52], where it was suggested that D should be taken to have a small value with negative or positive sign, to control the TW solutions and break this degeneracy.

Also, we note that the coefficient $A > 0$ in the thermosolutal normal form (2.91) which allows thermosolutal convection to match all cases with $A > 0$ in [52] (see Figure 2.2). Specifically, the cases with $M < 0$ since $M = 2C + D = -\left(1 + \frac{2}{\varpi}\right)\frac{S}{1+\frac{1}{p}SR}$.

2.5 Conclusion

In this chapter we have summarized the results of the amplitude equation given by [34]. Five types of solutions including T, SS, TW, SW and MW have been discussed in the normal form analysis together with the averaging method. The main transitions and bifurcations between states have been given, and are shown in more detail for cases IV$-$ with $A > 0$ and I$-$, II$-$, and III$-$ with $A < 0$ in Chapter 3, 4 and 5.

The normal form equation that describes the nonlinear dynamics near the codimension-two bifurcation point for a system of thermosoltual convection with $O(2)$ symmetry have also been computed using weakly nonlinear analysis. We find that the coefficient that controls the TW bifurcation vanishes in the normal form derivation. Normally this could be resolved by going to higher order in the analysis, but TW, SW, and MW solutions have been found in numerical investigations of the PDEs for thermosolutal convection [37, 98, 105], so we will break the degeneracy by assuming D is small with positive or negative sign.

Chapter 3

A model PDE for thermosolutal convection

3.1 Introduction

For many years, the Swift–Hohenberg equation has been considered as a simple model for the onset of thermal convection in fluids. Although it was originally conceived as a model of the effects of thermal fluctuations close to the onset of convection [43, 102], it is now regarded as a model of pattern formation in many physical problems [23, 32, 35] as it reproduces many universal features of pattern formation and it is much easier to investigate than the PDEs for Rayleigh–Bénard convection.

This dissertation aims to develop a new and as simple as possible model based on the Swift–Hohenberg equation that can describe double-diffusive convection. In particular, we are interested in a system in which the amplitude equation shows two marginally stable/unstable modes, one steady and one oscillatory, at the same critical wavenumber similar to observations of thermosolutal convection

[45, 52, 54, 79, 112].

Our criteria for developing the model consists of five important points.

- We want to replicate the linear stability behaviour close to onset of thermosolutal convection in our model.
- By adding simple nonlinearities, the model should be able to be reduced further to the Takens–Bogdanov (TB) normal form equation (2.1).
- When the model is reduced to the TB normal form equation, we can use the results given by [34]. We want the model to allow most of the cases listed in [34] including all cases that are relevant to thermosolutal convection, in particular, the cases with $A > 0$ in the TB normal form equation.
- We want the model to be Lyapunov stable, i.e., when $|u| \to \infty$ we want $\frac{d}{dt}|u| \leq 0$. Without this, investigating the model is difficult as trajectories can sometimes go to infinity.
- We are developing a model that will be a useful description of the qualitative features of thermosolutal convection. But by allowing our model to be more general, we could make the model relevant to other pattern-forming problems with a TB normal form.

In Section 3.2 we will explain in more detail the way we develop the model starting from the linear part of the thermosolutal convection equations. Then, in Section 3.3 we will discuss the nonlinearities we can add to the model, taking into account Lyapunov stability. In Section 3.4 we apply weakly nonlinear analysis to reduce the model to the TB normal form equation. In order to investigate the weakly nonlinear behaviour in Section 3.5, we relate the model to the results given by [34].

3.2 Derivation of the linear part of the model

The starting point for developing the model comes from the linear behaviour of thermosolutal convection. As explained in Chapter 1, thermosolutal convection is influenced by two different density gradients. A measure for thermal gradients is the thermal Rayleigh number Ra and a measure for concentration gradients is the solutal Rayleigh number Rs. When $Rs < Rs_c$, as the temperature gradient Ra increases, a pitchfork bifurcation occurs leading to steady convection when $Ra = Ra_{\mathrm{PF}}$, where

$$Ra_{\mathrm{PF}} = Ra_0 + \frac{Rs}{\zeta}, \qquad (Rs < Rs_c)\,, \tag{3.1}$$

and

$$Ra_0 = \frac{(k^2+\pi^2)^3}{k^2}.$$

When $Rs > Rs_c$, the bifurcation changes to a Hopf bifurcation leading to oscillatory convection when Ra reaches Ra_{Hopf} (see Figure 1.9), where

$$Ra_{\mathrm{Hopf}} = \frac{(1+\zeta)(Pr+\zeta)}{Pr} Ra_0 + \frac{Pr+\zeta}{1+Pr} Rs, \qquad (Rs > Rs_c)\,, \tag{3.2}$$

Pr and ζ are the Prandtl number and the solutal diffusivity ratio ($0 < \zeta < 1$), respectively. Thus, a new model requires two control parameters in the linear part, let say r and q, where r corresponds to the thermal Rayleigh number Ra and q corresponds to the solutal Rayleigh number Rs. We want $(r, q) = (0, 0)$ when $(Ra, Rs) = (Ra_c, Rs_c)$ (see Figure 3.1) where Ra_c, Rs_c are the critical values at which the pitchfork and Hopf bifurcations coincide, the TB point, given by

$$\begin{aligned} Ra_c &= \frac{(Pr+\zeta)}{Pr\,(1-\zeta)} Ra_0, \\ Rs_c &= \frac{\zeta^2\,(1+Pr)}{Pr\,(1-\zeta)} Ra_0. \qquad 0 < \zeta < 1. \end{aligned} \tag{3.3}$$

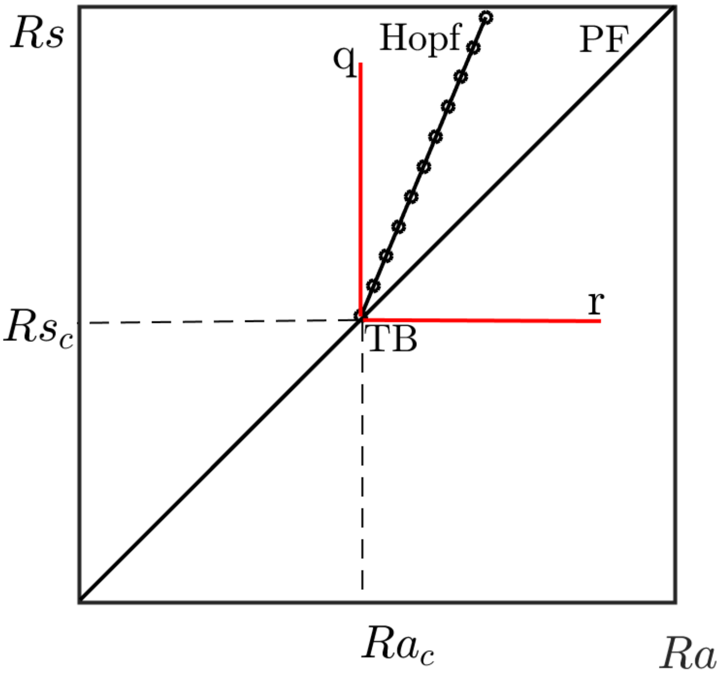

Figure 3.1: The (Ra, Rs)-plane of thermosolutal convection showing the pitchfork and Hopf bifurcation. The TB point (Ra_c, Rs_c) is mapped to $(r_c, q_c) = (0, 0)$ in (r, q)-plane.

We also want Ra and Rs to depend linearly on r and q. Therefore, we suppose

$$\begin{aligned} Ra &= Ra_c + Ar, \\ Rs &= Rs_c + Bq, \end{aligned} \tag{3.4}$$

where we will choose the value of A and B in order to simplify later expressions. Substituting (3.4) into (3.1) and (3.2) to determine the pitchfork and Hopf bifurcations, we get

$$\begin{aligned} r_{\mathrm{PF}} &= \frac{1}{A}\left(Ra_0 + \frac{Rs_c}{\zeta} - Ra_c\right) + \frac{B}{A\zeta}q, \\ r_{\mathrm{Hopf}} &= \frac{1}{A}\left(\frac{(1+\zeta)(Pr+\zeta)}{Pr}Ra_0 + \frac{Pr+\zeta}{1+Pr}Rs_c - Ra_c\right) + \frac{B(Pr+\zeta)}{A(1+Pr)}q. \end{aligned} \tag{3.5}$$

Substituting Ra_c and Rs_c from (3.3) into (3.5), we find that the terms that do not depend on q vanish and we get

$$\begin{aligned} r_{\mathrm{PF}} &= \frac{B}{A\zeta}q, \\ r_{\mathrm{Hopf}} &= \frac{B(Pr+\zeta)}{A(1+Pr)}q. \end{aligned} \tag{3.6}$$

For simplicity, we can choose $B = \zeta A$ then we get

$$\begin{aligned} r_{\mathrm{PF}} &= q, \\ r_{\mathrm{Hopf}} &= \frac{\zeta\,(Pr+\zeta)}{1+Pr}q. \end{aligned} \tag{3.7}$$

This is equivalent to

$$\begin{aligned} r_{\mathrm{PF}} &= q, \\ r_{\mathrm{Hopf}} &= aq, \end{aligned} \tag{3.8}$$

where

$$a = \frac{\zeta\,(Pr+\zeta)}{1+Pr}.$$

From the bifurcation diagram for thermosolutal convection (Figure 1.9), it is notable that the slope of the Hopf bifurcation line is larger than the slope of the pitchfork bifurcation line, which implies that a should be less than 1. In fact, since $0 < \zeta < 1$, $Pr + \zeta < Pr + 1$, this ensures that $0 < a < 1$.

Next, we relate the parameters (r, q) to the linear parameters in the TB normal form, (ν, μ). As we discussed in Chapter 2, close to the TB point, the amplitude equation shows that the pitchfork bifurcation occurs when $\mu = 0$ and a Hopf bifurcation occurs when $\nu = 0$ and $\mu < 0$. If $\mu < 0$ and $\nu < 0$, the zero solution is stable since it has two eigenvalues with negative real part. This allows us to express μ and ν in terms of r and q as follows:

$$\begin{aligned} \mu &= r - q, \\ \nu &= r - aq. \end{aligned} \tag{3.9}$$

We will use (ν, μ) as the parameters in our model, since we are investigating the pitchfork and Hopf bifurcations. This indicates that the pitchfork bifurcation occurs when $\mu = 0$, i.e., $r = q$ and the Hopf bifurcation occurs when $\nu = 0$ and $\mu < 0$, i.e., $r = aq$ and $r < q$ since $a < 1$ this implies $q > 0$.

Using (ν, μ) as the parameters in the model implies that the behaviour of the model does not depend on a. However, the mapping between (r, q) and (ν, μ) does depend on a, as shown in Figure 3.2. This figure has (a,b) with $0 < a < 1$ and (c,d) with $a < 0$, showing (a,c) the (r, q)-plane and (b,d) the (ν, μ)-plane. For $q > 0$, the first bifurcation as r increases is a Hopf bifurcation, (below diagonal in (ν, μ)-plane). For $q < 0$, the first bifurcation as r increases is a pitchfork bifurcation, (above diagonal in (ν, μ)-plane). This indicates that in the (ν, μ)-plane the bifurcations still occur in the same order as in thermosolutal convection for both $0 < a < 1$ and $a < 0$. Even though thermosolutal convection has $0 < a < 1$, in our model we allow $a < 0$ as well.

The pitchfork and Hopf bifurcation expressions (3.1) and (3.2) show Ra and Rs depend on k through a common factor of Ra_0. Ra_0 has a minimum at $k = k_c = \frac{\pi}{\sqrt{2}}$. Near k_c, Ra_0 is expanded as

$$Ra_0(k^2) \approx Ra_0 + \frac{Ra_0''}{8k_c^2}(k_c^2 - k^2)^2, \tag{3.10}$$

where $Ra_0'' = \frac{d^2 Ra_0}{dk^2}$. Therefore, close to this minimum we can incorporate k into

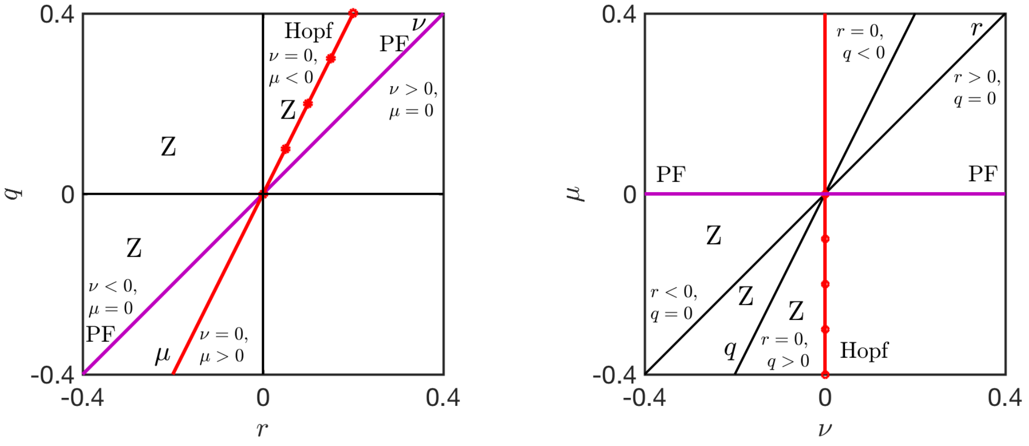

(a) **(b)**

$0 < a < 1$

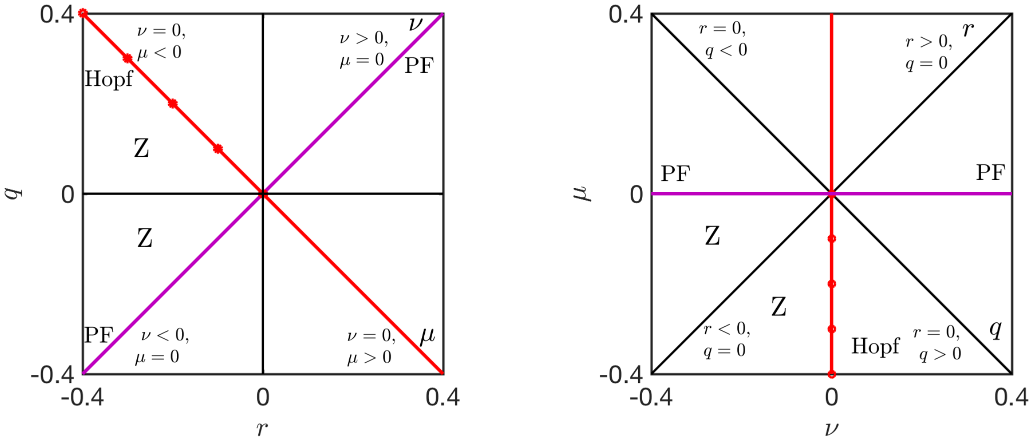

(c) **(d)**

$a < 0$

Figure 3.2: Plot (r, q)-plane from (3.8) (a) with $0 < a < 1$ and (c) with $a < 0$. Plot (ν, μ) from (3.9) (b) with $0 < a < 1$ and (d) with $a < 0$. The axes labelled with (r, q) or (ν, μ) with the label close to the positive end of the axis. The solid pink line refers to the pitchfork bifurcation and the red line with star markers refers to the Hopf bifurcation. The Z denotes to the zero stable solution.

r_{PF} and r_{Hopf} by writing r_{PF} and r_{Hopf} in terms of $(k_c^2 - k^2)$ as

$$\begin{aligned} r_{\text{PF}} &= q + (k_{\text{cPF}}^2 - k^2)^2, \\ r_{\text{Hopf}} &= aq + b(k_{\text{cHopf}}^2 - k^2)^2, \end{aligned} \tag{3.11}$$

where b is a constant, and k_{cPF} and k_{cHopf} are the critical wavenumbers for the pitchfork and Hopf bifurcation, respectively. The coefficient in front of $(k_{\mathrm{cPF}}^2 - k^2)^2$ in r_{PF} can be scaled to 1 by scaling other parameters. Comparing with the pitchfork and Hopf bifurcation expressions in equations (3.1) and (3.2) for thermosolutal convection leads us to conclude that $b = \frac{(1+\zeta)(Pr+\zeta)}{Pr}$ which is greater than 1. Thus, for later calculations we take $b > 1$.

Now, we want to write the linear part of the new model based on Van der Pol–Duffing equation (1.52). The linear part of Van der Pol–Duffing equation is

$$\ddot{u} - \kappa\dot{u} - \lambda u = 0, \tag{3.12}$$

where u is the amplitude of the lowest-order mode of the stream function in two-dimensional double-diffusive convection, κ and λ are unfolding parameters. For this linear equation, we can assume a solution of the form $u = e^{\sigma t}$, where σ is the growth rate. The characteristic equation then takes the following form

$$\sigma^2 - \kappa\sigma - \lambda = 0. \tag{3.13}$$

This is equivalent to an eigenvalue problem for σ of the form

$$\sigma \begin{bmatrix} 1 \\ \sigma \end{bmatrix} = \begin{bmatrix} 0 & 1 \\ \lambda & \kappa \end{bmatrix} \begin{bmatrix} 1 \\ \sigma \end{bmatrix} = \mathcal{L} \begin{bmatrix} 1 \\ \sigma \end{bmatrix}. \tag{3.14}$$

A pitchfork bifurcation (with one zero eigenvalue) occurs when the determinant is zero, i.e., $\lambda = 0$, and a Hopf bifurcation (with purely imaginary eigenvalues) occurs when the trace is zero and the determinant is positive, i.e., $\kappa = 0$ and $\lambda < 0$. At the TB point, the system has two zero eigenvalues, i.e. $\kappa = \lambda = 0$. Now we want to relate the relations in (3.11) to this two-dimensional dynamical system. If we set

$$\begin{aligned}\lambda &= r - q - (k_{\text{cPF}}^2 - k^2)^2,\\ \kappa &= r - aq - b(k_{\text{cHopf}}^2 - k^2)^2,\end{aligned} \tag{3.15}$$

then $\lambda = 0$ when $r = r_{\text{PF}}$, and $\kappa = 0$ when $r = r_{\text{Hopf}}$. The linear operator $\mathcal{L}$ in (3.14) in terms of (3.15) is then given as

$$\mathcal{L} = \begin{bmatrix} 0 & 1 \\ r - q - (k_{\text{cPF}}^2 - k^2)^2 & r - aq - b(k_{\text{cHopf}}^2 - k^2)^2 \end{bmatrix}. \tag{3.16}$$

Consequently, we can write the linear equation (3.12) as

$$\ddot{u} - \left(r - aq - b(k_{\text{cHopf}}^2 - k^2)^2\right)\dot{u} - \left(r - q - (k_{\text{cPF}}^2 - k^2)^2\right)u = 0, \tag{3.17}$$

where $u(t)$ is the amplitude at lowest order mode e^{ikx}. This equation in Fourier space can be converted into a PDE by replacing k^2 with $-\frac{\partial^2}{\partial x^2}$ and considering u to be a function of x and t. Then the ODE (3.17) can be converted to PDE as

$$u_{tt} - \left(r - aq - b\left(k_{\text{cHopf}}^2 + \frac{\partial^2}{\partial x^2}\right)^2\right)u_t - \left(r - q - \left(k_{\text{cPF}}^2 + \frac{\partial^2}{\partial x^2}\right)^2\right)u = 0, \tag{3.18}$$

where $u_{tt} = \frac{\partial^2 u}{\partial t^2}$ and $u_t = \frac{\partial u}{\partial t}$ are the derivatives with respect to scaled time, and the parameters k_{cPF} and k_{cHopf} are the wavenumbers for the pitchfork and Hopf bifurcations. If $k_{\text{cPF}} \neq k_{\text{cHopf}}$ then this model could be relevant to other problems where the pitchfork and Hopf bifurcation have different critical wavenumbers, for example magnetoconvection [4, 26, 86, 92, 115] and rotating convection [28, 109, 110, 121]. Since we are interested in the linear behaviour of thermosolutal convection, where the pitchfork and Hopf bifurcations have the same critical wavenumbers (see Figures 1.9 and 1.10), thus we let $k_{\text{cPF}} = k_{\text{cHopf}} = k_c$. Applying the transformation

$$t \to \frac{1}{k_c^2}t, \qquad r \to k_c^4 r, \qquad q \to k_c^4 q, \qquad x \to \frac{1}{k_c}x \tag{3.19}$$

to (3.18) we get the same equation with $k_{\mathrm{cPF}} = k_{\mathrm{cHopf}} = k_c = 1$. Then the linear second order partial differential equation that models thermosolutal convection takes the following from:

$$u_{tt} - \left(r - aq - b\left(1 + \frac{\partial^2}{\partial x^2}\right)^2\right) u_t - \left(r - q - \left(1 + \frac{\partial^2}{\partial x^2}\right)^2\right) u = 0, \qquad (3.20)$$

with $a < 1$ and $b > 1$. We can use (3.9) to write the PDE in terms of μ and ν instead of r and q as

$$u_{tt} - \left(\nu - b\left(1 + \frac{\partial^2}{\partial x^2}\right)^2\right) u_t - \left(\mu - \left(1 + \frac{\partial^2}{\partial x^2}\right)^2\right) u = 0. \qquad (3.21)$$

Figure 3.3 summarizes the type of motion at the onset of convection for the model (3.20) for a mode with $k_{\mathrm{cPF}} = k_{\mathrm{cHopf}} = 1$. With $q < q_c$, as r increases the pitchfork bifurcation occurs at $r = q$ leading to steady convection. With $q > q_c$, the first bifurcation as r increases is a Hopf bifurcation at $r = aq$ leading to oscillatory convection. The zero solution is stable for $r < \min(q, aq)$. Figure 3.4 shows the neutral stability curve for pitchfork and Hopf bifurcation from (3.11) with $k_{\mathrm{cPF}} = k_{\mathrm{cHopf}} = 1$. From the figure we can see that the pitchfork bifurcation occurs when $q < q_c$, the Hopf bifurcation occurs when $q > q_c$ and they coincide when $q = q_c$ at the same critical wavenumber, $k_{\mathrm{cPF}} = k_{\mathrm{cHopf}} = 1$. This replicates the neutral stability curve of thermosolutal convection (Figure 1.10). The dispersion relation can be determined by studying the eigenvalues of the model given by

$$\sigma(k) = \frac{\left(r - aq - b\left(1 - k^2\right)^2\right) \pm \sqrt{\left(r - aq - b\left(1 - k^2\right)^2\right)^2 + 4\left(r - q - \left(1 - k^2\right)^2\right)}}{2}. \qquad (3.22)$$

Since the growth rate σ depends on the wavenumber k, some modes could decay and some could grow. If all eigenvalues for all k have negative real parts the evolution decays and the zero solution is linearly stable. If any eigenvalue for

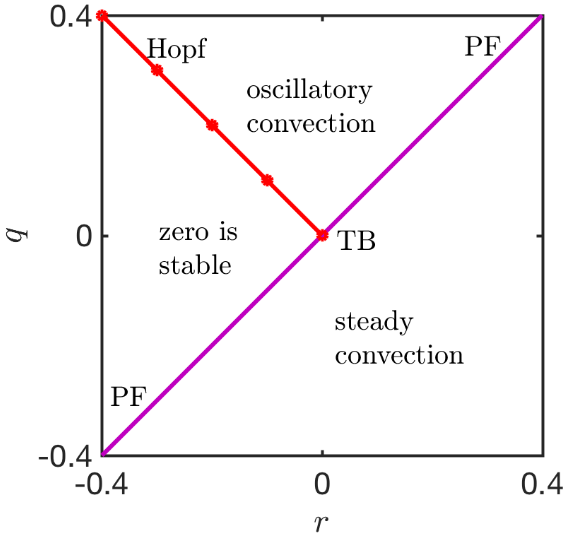

Figure 3.3: Bifurcation diagram r versus q from (3.8) for $k_{\text{cPF}} = k_{\text{cHopf}} = 1$. The diagram shows the type of motion close to the TB point where the Hopf (red line with star markets) and pitchfork (solid pink line) are coincident. We have chosen the illustrative value $a = -1$.

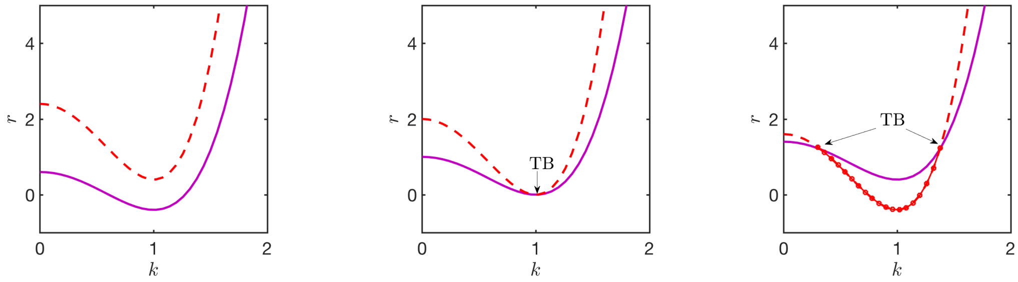

(a) $q = -0.4$ **(b)** $q = 0$ **(c)** $q = 0.4$

Figure 3.4: Plot of the neutral stability curves from (3.11) for $b = 2$ and $a = -1$. The figure shows that there is TB point similar to the stability curves of thermosolutal convection Figure 1.10 when $q \geq 0$. The solid pink line refers to pitchfork bifurcation and closed circle red line refers to Hopf bifurcation where the determinant r_{PF} is negative. The dashed line indicates to the Hopf bifurcation curve where the determinant r_{PF} is positive and so the Hopf bifurcation is not exist.

any k has positive real part the evolution grows and the zero solution is linearly unstable. Figure 3.5 shows a plot of the real part of the dispersion relation, $Re(\sigma)$, as a function of wavenumber k. A pitchfork bifurcation occurs when $q < 0$. When r is lower than the pitchfork bifurcation curve in Figure 3.4, we can see that

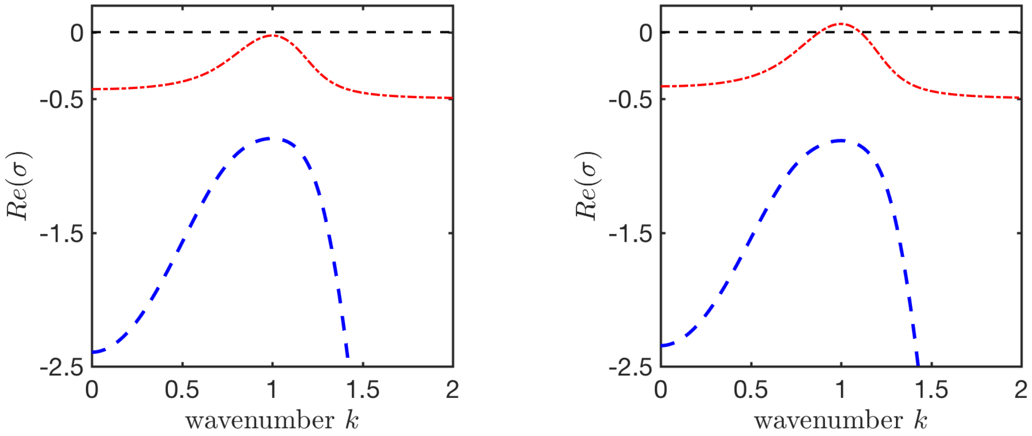

(a) $q = -0.4, r < r_{\text{PF}}$ **(b)** $q = -0.4, r > r_{\text{PF}}$

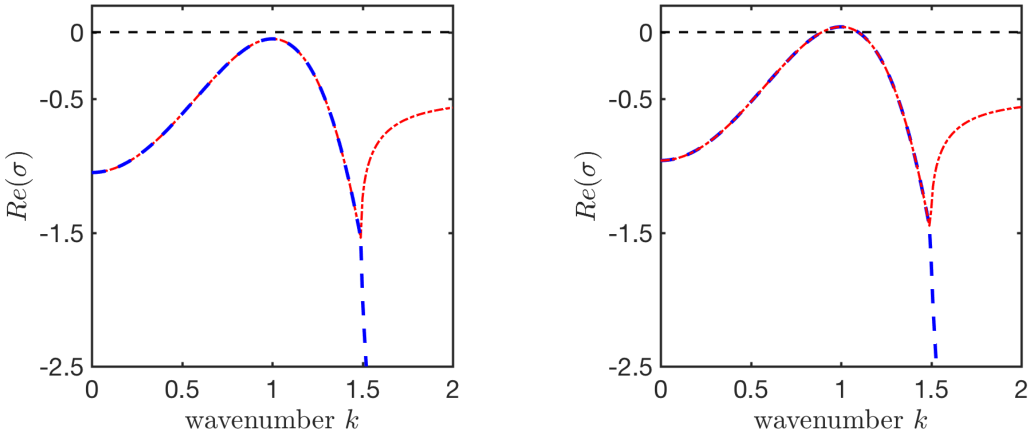

(c) $q = 0.4, r < r_{\text{Hopf}}$ **(d)** $q = 0.4, r > r_{\text{Hopf}}$

Figure 3.5: The real growth rates σ_+ in dash-dot red and σ_- in dash blue as a function of wavenumber k from (3.22) where $a = -1$ and $b = 2$. Panels (a,b) show the real growth rates for $q < 0$, a pitchfork bifurcation occurs at $r = r_{\text{PF}} = q$. (a) $r < r_{\text{PF}}$, all growth rates are negative and the zero solution is stable and (b) $r > r_{\text{PF}}$, the instability occurs since there are some modes with positive σ. Panels (c,d) show the real part of complex conjugate growth rates for $q > 0$, a Hopf bifurcation occurs at $r = r_{\text{Hopf}} = aq$. (c) $r < r_{\text{Hopf}}$ all growth rates have negative real part and the zero solution is stable, (d) $r > r_{\text{Hopf}}$, instability occurs leading to oscillatory convection.

$Re(\sigma) < 0$ for all wavenumber k, and so the trivial solution is linearly stable. For r greater than the pitchfork bifurcation value, we have instability since there are some $Re(\sigma) > 0$ with wavenumber k close to 1. A Hopf bifurcation occurs when $q > 0$, and similarly all real growth rates are negative when r is lower than the Hopf bifurcation and the zero solution is stable. For r greater than the Hopf bifurcation there are some positive growth rates and the zero solution becomes unstable leading to oscillatory convection.

3.3 Nonlinear part of the model

Linear stability analysis in general is valid for perturbations of small amplitude for which nonlinearities are negligible. Once the zero solution is unstable, exponential growth means that nonlinear terms will become important. After developing the linear part of our model, in this section we will discuss the nonlinearities that we will add to the model, which should satisfy the criteria we have mentioned in Section 3.1.

The model (3.20) is a partial differential equation second order in time so having nonlinearities with first order time derivative u_t terms is possible. Since we aim to make the model a useful description of double-diffusive convection, in choosing the nonlinearities we consider the $O(2)$ symmetry of the physical system of interest but that system can be reduced to Takens–Bogdanov normal form (2.1). Therefore, we choose the nonlinearities containing up two spatial derivatives and satisfy the symmetry $u(x) = u(-x)$. The nonlinearities also should allow us to obtain the Takens–Bogdanov normal form. To keep the model as simple as possible, we will choose the nonlinearities to be quadratic and cubic in u and u_t. Some possible quadratic terms in u and u_t are

$$u^2, uu_t, u_t^2, uu_{xx}, (u_x)^2, uu_{txx}, u_tu_{xx}, u_xu_{tx}, \tag{3.23}$$

and some cubic terms in u and u_t are

$$u^3, uu_t^2, u^2u_t, u_t^3, (uu_{xx})u_t, (u_x)^2u_t, u^2u_{txx}, uu_tu_{xx}, uu_xu_{tx}. \tag{3.24}$$

Similar terms (without the u_t contributions) have been incorporated into various generalisation of the Swift–Hohenberq equation [18, 31, 64]. Including all the nonlinearities mentioned would make the model very complicated. The aim of developing the model is

- to make the model as simple as possible.
- to reduce the model to TB normal form equation (2.1), which has the cubic terms $|z|^2 z, |z|^2 z_t$ and $z^2 \bar{z}_t$.
- when the model is reduced to the TB normal form, the behaviour depends on the coefficients of the cubic terms $|z|^2 z, |z|^2 z_t$ and $z^2 \bar{z}_t$ in (2.1). The model should allow a wide range of weakly nonlinear behaviour including all behaviour exhibited by thermosolutal convection.
- to be easy to solve numerically.

It is important to consider the global stability, since for some choices of nonlinear terms, trajectories go to infinity, preventing numerical solution. We will ensure global stability using a Lyapunov stability function, based on the Lyapunov function for the Swift–Hohenberg equation. We start with the quadratic–cubic nonlinearity $gu^2 - u^3$. The Swift–Hohenberg equation is

$$\frac{\partial u}{\partial t} = ru - \left(1 + \frac{\partial^2}{\partial x^2}\right)^2 u + gu^2 - u^3, \tag{3.25}$$

where r is the control parameter and g is a constant. The Swift–Hohenberg equation possesses a Lyapunov functional given by

$$F(t) = \int_0^L \left[-\frac{1}{2} r u^2 + \frac{1}{2} \left[(1 + \frac{\partial^2}{\partial x^2}) u \right]^2 - \frac{1}{3} g u^3 + \frac{1}{4} u^4 \right] dx, \tag{3.26}$$

where L is the length of the periodic domain. F is bounded below because

$\frac{1}{2}\left(u+u_{xx}\right)^2 \geq 0$ and $\left(-\frac{1}{2}ru^2-\frac{1}{3}gu^3+\frac{1}{4}u^4\right)$ is a quartic with positive u^4 coefficient. By differentiating F with respect to time, we get

$$\begin{aligned}\frac{dF}{dt} &= \int_0^L \left[-ru+\left(1+\frac{\partial^2}{\partial x^2}\right)^2 u - gu^2+u^3\right] u_t\, dx \\ &= \int_0^L -\left(\frac{\partial u}{\partial t}\right)^2 dx \leq 0.\end{aligned} \tag{3.27}$$

This indicates that along any trajectory F does not increase in time, so all trajectories go to stationary points of F, and minima of F are stable.

Following this, as a first step we will add the same quadratic and cubic terms u^2 and u^3 to our model. The PDE (3.21) then takes the following form

$$\frac{\partial^2 u}{\partial t^2} = \left(\mu-\left(1+\frac{\partial^2}{\partial x^2}\right)^2\right)u+\left(\nu-b\left(1+\frac{\partial^2}{\partial x^2}\right)^2\right)\frac{\partial u}{\partial t}+Q_1u^2+C_1u^3, \tag{3.28}$$

where Q_1 and C_1 are constants. We try a Lyapunov function for the PDE (3.28) of the form

$$F(t) = \int_0^L \left[\frac{1}{2}u_t^2-\frac{1}{2}\mu u^2+\frac{1}{2}\left[\left(1+\frac{\partial^2}{\partial x^2}\right)u\right]^2-\frac{1}{3}Q_1u^3-\frac{1}{4}C_1u^4\right]dx. \tag{3.29}$$

If $C_1 < 0$ then $\frac{1}{4}u^2\left(-C_1u^2-\frac{4}{3}Q_1u-2\mu\right)$ is a quartic that is (as a function of u) bounded below whether μ or Q_1 is positive or negative. By differentiating F with respect to time and integrating by parts, we get

$$\begin{aligned}\frac{dF}{dt} &= \int_0^L \left[u_tu_{tt}-\mu uu_t+\left[\left(1+\frac{\partial^2}{\partial x^2}\right)^2 u\right]u_t-Q_1u^2u_t-C_1u^3u_t\right]dx \\ &= \int_0^L \left[u_{tt}-\mu u+\left(1+\frac{\partial^2}{\partial x^2}\right)^2 u-Q_1u^2-C_1u^3\right]u_t\, dx.\end{aligned} \tag{3.30}$$

From (3.28), we can rewrite the last equation as follows:

$$\frac{dF}{dt} = \int_0^L \left[\nu u_t^2 - b\left(\left(1 + \frac{\partial^2}{\partial x^2}\right) u_t \right)^2 \right] dx, \tag{3.31}$$

since, using integration by parts

$$\int_0^L \left[u_t \left(1 + \frac{\partial^2}{\partial x^2}\right)^2 u_t \right] dx = \int_0^L \left[\left(\left(1 + \frac{\partial^2}{\partial x^2}\right) u_t \right)^2 \right] dx. \tag{3.32}$$

From Section 3.2, we know that $b > 1$. Therefore, if ν is negative then $F(t)$ does not increase in time. Requiring ν to be negative is too strict a condition (it precludes the Hopf bifurcation), so in order to allow the global stability for ν positive or negative we modify the model by adding more nonlinearities. We start with the simplest additional cubic terms u^2u_t, uu_t^2 and u_t^3. Then the PDE becomes

$$\begin{aligned} \frac{\partial^2 u}{\partial t^2} = &\left(\mu - \left(1 + \frac{\partial^2}{\partial x^2}\right)^2\right) u + \left(\nu - b\left(1 + \frac{\partial^2}{\partial x^2}\right)^2\right) \frac{\partial u}{\partial t} + Q_1 u^2 + C_1 u^3 \\ &+ C_2 u^2 u_t + C_3 u u_t^2 + C_4 u_t^3, \end{aligned}$$

where Q_1, C_1, C_2, C_3 and C_4 are constant coefficients. Applying the same Lyapunov function as before (3.29), we can write (3.30) with the new nonlinearities as

$$\begin{aligned} \frac{dF}{dt} &= \int_0^L \left[u_{tt} - \mu u + \left(1 + \frac{\partial^2}{\partial x^2}\right)^2 u - Q_1 u^2 - C_1 u^3 \right] u_t \, dx \qquad (3.33) \\ &= \int_0^L \left[\nu u_t - b\left(1 + \frac{\partial^2}{\partial x^2}\right)^2 u_t + C_2 u^2 u_t + C_3 u u_t^2 + C_4 u_t^3 \right] u_t \, dx. \qquad (3.34) \end{aligned}$$

This is equivalent to

$$\frac{dF}{dt} = \int_0^L \left[\nu u_t^2 - b\left(\left(1 + \frac{\partial^2}{\partial x^2}\right) u_t \right)^2 + C_2 u^2 u_t^2 + C_3 u u_t^3 + C_4 u_t^4 \right] dx. \tag{3.35}$$

If $u_t = 0$ for all x, then $\frac{dF}{dt} = 0$ and we have an equilibrium. Now, we want to prove that, for large non-equilibrium u and u_t, all trajectories have F decreasing in time for ν negative or positive. For large u and u_t, the last three terms dominate as they are quartic, so let us write the last three terms as follows:

$$T = \int_0^L \left[C_2 u^2 u_t^2 + C_3 u u_t^3 + C_4 u_t^4 \right] dx. \tag{3.36}$$

We write

$$u(x,t) = R\cos\phi, \quad u_t(x,t) = R\sin\phi, \tag{3.37}$$

where $R(x,t)$ is a large radius and $\phi(x,t)$ is an angle. Substituting (3.37) into (3.36), we get

$$T = \int_0^L \left[R^4 \left(C_2 \cos^2\phi + C_3 \cos\phi \ \sin\phi + C_4 \sin^2\phi \right) \sin^2\phi \right] dx. \tag{3.38}$$

Using trigonometric identities, we can write this equation as

$$T = \int_0^L \left[R^4 \left(\frac{1}{2}\left(C_2 + C_4\right) + \frac{1}{2}\left(C_2 - C_4\right)\cos 2\phi + \frac{1}{2} C_3 \sin 2\phi \right) \sin^2\phi \right] dx. \tag{3.39}$$

If trajectories are to remain bounded for any choice of ν, $\frac{dF}{dt}$ must be negative for any (u, u_t) large enough as long as u_t is not zero for all x. This is guaranteed if $T < 0$ for any ϕ as long as $\sin\phi$ is not zero for all x, which requires

$$C_2 + C_4 < 0$$

and

$$0 < \sqrt{\left(\frac{1}{2}\left(C_2 - C_4\right)\right)^2 + \left(\frac{1}{2}C_3\right)^2} < -\frac{1}{2}\left(C_2 + C_4\right),$$

which implies

$$C_2 C_4 - \frac{1}{4} C_3^2 > 0.$$

To make the model simple we let $C_3 = 0$, then $\frac{dF}{dt}$ is strictly negative for large

(u, u_t) non-equilibrium if and only if

$$C_2 + C_4 < 0 \ \text{ and } \ C_2C_4 > 0,$$

which implies $C_2 < 0$ and $C_4 < 0$. Therefore the model second order partial differential equation takes the following form

$$\frac{\partial^2 u}{\partial t^2} = \left(\mu - \left(1 + \frac{\partial^2}{\partial x^2}\right)^2\right) u + \left(\nu - b\left(1 + \frac{\partial^2}{\partial x^2}\right)^2\right) \frac{\partial u}{\partial t} + Q_1 u^2 + C_1 u^3$$
$$+ C_2 u^2 u_t + C_4 u_t^3, \tag{3.40}$$

where μ and ν are the control parameters, $b > 1$, Q_1, C_1, C_2 and C_4 are constants coefficients with $C_1 < 0$ to make F bounded below, and $C_2 < 0$ and $C_4 < 0$ to make F decrease for large u or u_t.

Weakly nonlinear theory (in Section 3.4) will show that the current model has only a limited range of possibilities in the TB normal form. Later in Chapter 4 and 5, we will add more nonlinearities in order to access other possibilities.

3.4 Weakly nonlinear theory

In this section, we use weakly nonlinear theory to reduce the PDE (3.40) to the TB normal form. In the weakly nonlinear calculation, we consider small amplitude solutions close to TB point, so $\mu \ll 1, \nu \ll 1$ and $u \ll 1$. In addition, we look for solutions with wavenumber $k = k_c = 1$. We introduce a small parameter ϵ to control the amplitude of the solution ($u = O(\epsilon)$). At this point the scaling is not obvious, so we scale time and the parameters μ and ν as follows:

$$\frac{\partial}{\partial t} \to \epsilon^{\eta} \frac{\partial}{\partial t}, \ \mu \to \epsilon^m \mu_m, \ \nu \to \epsilon^n \nu_n. \tag{3.41}$$

where $\eta > 0, m > 0$ and $n > 0$ are to be determined. We assume u is $O(\epsilon)$ and expand as

$$u = \epsilon u_1 + \epsilon^2 u_2 + \epsilon^3 u_3 + \epsilon^4 u_4 + \cdots . \tag{3.42}$$

By substituting the scaling and (3.42) into the governing equation (3.40), we get

$$\begin{aligned}
\epsilon^{2\eta+1}\frac{\partial^2 u_1}{\partial t^2} + \epsilon^{2\eta+2}\frac{\partial^2 u_2}{\partial t^2} + \epsilon^{2\eta+3}\frac{\partial^2 u_3}{\partial t^2} + \cdots = {} & \mu_m \left(\epsilon^{m+1} u_1 + \epsilon^{m+2} u_2 + \epsilon^{m+3} u_3 + \cdots\right) \\
& - \left(1 + \frac{\partial^2}{\partial x^2}\right)^2 \left(\epsilon u_1 + \epsilon^2 u_2 + \epsilon^3 u_3 + \cdots\right) \\
& + \nu_n \left(\epsilon^{\eta+n+1}\frac{\partial u_1}{\partial t} + \epsilon^{\eta+n+2}\frac{\partial u_2}{\partial t} + \epsilon^{\eta+n+3}\frac{\partial u_3}{\partial t} + \cdots\right) \\
& - b\left(1 + \frac{\partial^2}{\partial x^2}\right)^2 \left(\epsilon^{\eta+1}\frac{\partial u_1}{\partial t} + \epsilon^{\eta+2}\frac{\partial u_2}{\partial t} + \epsilon^{\eta+3}\frac{\partial u_3}{\partial t} + \cdots\right) \\
& + Q_1 \left(\epsilon^2 u_1^2 + 2\epsilon^3 u_1 u_2 + \epsilon^4 u_2^2 + \cdots\right) \\
& + C_1 \left(\epsilon^3 u_1^3 + 3\epsilon^4 u_1^2 u_2 + \cdots\right) \\
& + C_2 \left(\epsilon^{\eta+3} u_1^2 \frac{\partial u_1}{\partial t} + \epsilon^{\eta+4}\left(u_1^2\frac{\partial u_2}{\partial t} + 2u_1 u_2 \frac{\partial u_1}{\partial t}\right) + \cdots\right) \\
& + C_4 \left(\epsilon^{3\eta+3}\left(\frac{\partial u_1}{\partial t}\right)^3 + \cdots\right).
\end{aligned} \tag{3.43}$$

The lowest order in ϵ is $O(\epsilon)$, and the equation at this order is

$$0 = -\left(1 + \frac{\partial^2}{\partial x^2}\right)^2 u_1. \tag{3.44}$$

We define the linear operator $\mathcal{L}$ as

$$\mathcal{L} = -\left(1 + \frac{\partial^2}{\partial x^2}\right)^2, \tag{3.45}$$

and so $\mathcal{L}$ acts on modes e^{ikx} as

$$\mathcal{L}e^{ikx} = -\left(1 - k^2\right)^2 e^{ikx}. \tag{3.46}$$

Solving $\mathcal{L}u_1 = 0$ implies u_1 is a linear combination of e^{ix} and e^{-ix} with $k = 1$. Insisting that u_1 is real leads to

$$u_1(x,t) = F_1(t)e^{ix} + \bar{F}_1(t)e^{-ix}, \tag{3.47}$$

where F_1 is a time-dependent complex amplitude. The next biggest order terms in ϵ give the equation

$$\begin{aligned}\epsilon^{2\eta+1}\frac{\partial^2 u_1}{\partial t^2} &= \epsilon^{m+1}\mu_m u_1 + \epsilon^2\mathcal{L}u_2 + \epsilon^{\eta+n+1}\nu_n\frac{\partial u_1}{\partial t} + \epsilon^{\eta+1}b\mathcal{L}\frac{\partial u_1}{\partial t}\\ &+ \epsilon^2 Q_1 u_1^2 + \epsilon^3 C_1 u_1^3 + \epsilon^{\eta+3}C_2 u_1^2\frac{\partial u_1}{\partial t}.\end{aligned} \tag{3.48}$$

If we substitute (3.47) into (3.48), and if we look at the e^{ix} component, then any term that includes $\mathcal{L}$ will vanish. Then an equation that involves F_1 and its time derivatives is

$$\begin{aligned}\epsilon^{2\eta+1}\frac{\partial^2 F_1}{\partial t^2} &= \epsilon^{m+1}\mu_m F_1 + \epsilon^{\eta+n+1}\nu_n\frac{\partial F_1}{\partial t} + \epsilon^3 C_1|F_1|^2F_1 + \epsilon^{\eta+3}C_2F_1^2\frac{\partial \bar{F}_1}{\partial t}\\ &+ 2\epsilon^{\eta+3}C_2|F_1|^2\frac{\partial F_1}{\partial t}.\end{aligned} \tag{3.49}$$

In weakly nonlinear theory we want the time derivative, the linear term and the nonlinear term to be of the same order of magnitude. Balancing $F_{1_{tt}}, \mu_m F_1$ and $|F_1|^2F_1$ requires $\eta = 1$ and $m = 2$. In the TB normal form, $\nu_n F_{1_t}$ and $F_1^2\bar{F}_{1_t}$ appear one order in ϵ higher, so we set $n = 2$. Substituting $\eta = 1, m = 2$ and $n = 2$ into (3.43) we get

$$\begin{aligned}\frac{\partial^2}{\partial t^2}\left(\epsilon^3 u_1 + \epsilon^4 u_2 + \epsilon^5 u_3 + ...\right) &= \mu_2\left(\epsilon^3 u_1 + \epsilon^4 u_2 + \epsilon^5 u_3 + ...\right)\\ &- \left(1 + \frac{\partial^2}{\partial x^2}\right)^2\left(\epsilon u_1 + \epsilon^2 u_2 + \epsilon^3 u_3 + ...\right)\\ &+ \nu_2\left(\epsilon^4\frac{\partial u_1}{\partial t} + \epsilon^5\frac{\partial u_2}{\partial t} + \epsilon^6\frac{\partial u_3}{\partial t} + ...\right)\end{aligned}$$

$$
\begin{aligned}
&- b\left(1+\frac{\partial^2}{\partial x^2}\right)^2\left(\epsilon^2\frac{\partial u_1}{\partial t}+\epsilon^3\frac{\partial u_2}{\partial t}+\epsilon^4\frac{\partial u_3}{\partial t}+...\right)\\
&+ Q_1\left(\epsilon^2u_1^2+2\epsilon^3u_1u_2+\epsilon^4u_2^2+...\right)\\
&+ C_1\left(\epsilon^3u_1^3+3\epsilon^4u_1^2u_2+...\right)\\
&+ C_2\left(\epsilon^4u_1^2\frac{\partial u_1}{\partial t}+\epsilon^5\left(u_1^2\frac{\partial u_2}{\partial t}+2u_1u_2\frac{\partial u_1}{\partial t}\right)+...\right)\\
&+ C_4\left(\epsilon^6\left(\frac{\partial u_1}{\partial t}\right)^3+...\right). \qquad (3.50)
\end{aligned}
$$

At $O(\epsilon^2)$, we have

$$0=\mathcal{L}u_2+b\mathcal{L}\frac{\partial u_1}{\partial t}+Q_1u_1^2. \qquad (3.51)$$

The term $\mathcal{L}\frac{\partial u_1}{\partial t}$ is zero since there are just $e^{\pm ix}$ components in $\frac{\partial u_1}{\partial t}$. To solve (3.51) for u_2 we suppose u_2 to be of the form

$$u_2(x,t)=G_2(t)e^{2ix}+G_1(t)e^{ix}+G_0(t)+\bar{G_1}(t)e^{-ix}+\bar{G_2}(t)e^{-2ix}. \qquad (3.52)$$

where G_0, G_1, G_2 and the complex conjugate $\bar{G_1}, \bar{G_2}$ are time-dependent amplitudes. Substituting (3.52) and (3.47) into (3.51) and comparing the coefficients of the Fourier modes, we obtain

$$u_2=\frac{Q_1F_1^2}{9}e^{2ix}+G_1e^{ix}+2Q_1|F_1|^2+\bar{G_1}e^{-ix}+\frac{Q_1\bar{F_1}^2}{9}e^{-2ix}, \qquad (3.53)$$

where G_1 is going to be determined later. At $O(\epsilon^3)$, we have

$$\frac{\partial^2u_1}{\partial t^2}=\mu_2u_1+\mathcal{L}u_3+b\mathcal{L}\frac{\partial u_2}{\partial t}+2Q_1u_1u_2+C_1u_1^3, \qquad (3.54)$$

where u_3 is unknown in this equation. Since the nonlinear terms generate wavenumbers up to ±3, we suppose u_3 to be of the form

$$
\begin{aligned}
u_3(x,t)=&H_3(t)e^{3ix}+H_2(t)e^{2ix}+H_1(t)e^{ix}+H_0(t)+\bar{H_1}(t)e^{-ix}\\
&+\bar{H_2}(t)e^{-2ix}+\bar{H_3}(t)e^{-3ix}.
\end{aligned} \qquad (3.55)
$$

where H_0, H_1, H_2, H_3 and the complex conjugate $\bar{H}_1, \bar{H}_2, \bar{H}_3$ are time-dependent amplitudes. This equation has a solvability condition coming from the e^{ix} terms. By multiplying (3.47) by (3.52) to get the product u_1u_2 and substituting (3.47) and (3.55) into (3.54) and collecting the coefficients of $k = 1$ mode, we get

$$\frac{\partial^2 F_1}{\partial t^2} = \mu_2 F_1 + A|F_1|^2 F_1, \tag{3.56}$$

where $A = \frac{38}{9}Q_1^2 + 3C_1$. This is the leading order part of the TB normal form.

The TB normal form includes the terms $F_1^2\bar{F}_{1_t}$ and $F_{1_t}|F_1|^2$, which are found by going to $O(\epsilon^4)$. Thus, we need to solve (3.54) for u_3 by comparing the coefficients of Fourier modes:

$$\begin{aligned} u_3 = {} & \frac{1}{64}\left(\frac{2}{9}Q_1^2 + C_1\right) F_1^3 e^{3ix} + \frac{2}{9}Q_1\left(F_1G_1 - bF_1F_{1_t}\right)e^{2ix} + H_1e^{ix} \\ & + 2Q_1\left(F_1\bar{G}_1 + \bar{F}_1G_1 - b(F_{1_t}\bar{F}_1 + F_1\bar{F}_{1_t})\right) \\ & + \frac{1}{64}\left(\frac{2}{9}Q_1^2 + C_1\right)\bar{F}_1^{\,3}e^{-3ix} + \frac{2}{9}Q_1\left(\bar{F}_1\bar{G}_1 - b\bar{F}_1\bar{F}_{1_t}\right)e^{-2ix} + \bar{H}_1e^{-ix}. \end{aligned} \tag{3.57}$$

At $O(\epsilon^4)$, we have

$$\frac{\partial^2 u_2}{\partial t^2} = \mu_2 u_2 + \mathcal{L}u_4 + \nu_2\frac{\partial u_1}{\partial t} + b\mathcal{L}\frac{\partial u_3}{\partial t} + Q_1\left(u_2^2 + 2u_1u_3\right) + 3C_1u_1^2u_2 + C_2u_1^2\frac{\partial u_1}{\partial t}. \tag{3.58}$$

In the last equation u_4 is unknown. If we consider the $k = 1$ component of this equation, then $\mathcal{L}u_4$ gives no contribution and we get

$$\begin{aligned} \frac{\partial^2 G_1}{\partial t^2} = {} & \mu_2 G_1 + \nu_2\frac{\partial F_1}{\partial t} + \left(\frac{2}{9}Q_1^2 + 3C_1\right)F_1^2\bar{G}_1 + \left(\frac{40}{9}Q_1^2 + 6C_1\right)|F_1|^2G_1 \\ & + 4Q_1^2\left(F_1\bar{G}_1 + \bar{F}_1G_1\right) + \left(-4bQ_1^2 + C_2\right)\left(F_{1_t}\bar{F}_1 + F_1\bar{F}_{1_t}\right)F_1 \\ & + \left(-\frac{4}{9}bQ_1^2 + C_2\right)|F_1|^2F_{1_t}. \end{aligned} \tag{3.59}$$

We want to combine the equations (3.56) and (3.59) to one equation, the normal form equation, by using a reconstitution procedure [91]. Assuming

$$z = \epsilon F_1 + \epsilon^2 G_1, \tag{3.60}$$

and by unscaling time and the parameters according to

$$\frac{\partial}{\partial t} \to \frac{1}{\epsilon}\frac{\partial}{\partial t} \; \mu_2 \to \frac{1}{\epsilon^2}\mu \;\text{ and }\nu_2 \to \frac{1}{\epsilon^2}\nu, \tag{3.61}$$

we get

$$\begin{aligned}\frac{\partial^2 z}{\partial t^2} &= \mu z + \epsilon\nu\frac{\partial F_1}{\partial t} + \epsilon^3 A|F_1|^2 F_1 + \epsilon^4\left(\frac{2Q_1^2}{9} + 3C_1\right) F_1^2\bar{G}_1 \\ &+ \epsilon^4\left(\frac{40Q_1^2}{9} + 6C_1\right)|F_1|^2 G_1 + 4\epsilon^4 Q_1^2\left(F_1\bar{G}_1 + \bar{F}_1 G_1\right) \\ &+ \epsilon^3\left(-4bQ_1^2 + C_2\right)\left(F_{1_t}\bar{F}_1 + F_1\bar{F}_{1t}\right)F_1 + \epsilon^3\left(-\frac{4}{9}bQ_1^2 + C_2\right)|F_1|^2 F_{1_t}.\end{aligned} \tag{3.62}$$

Substituting $F_1 = \frac{z}{\epsilon} - \epsilon G_1$, in (3.62) and neglecting all the terms of $O(\epsilon)$, we get the amplitude equation

$$\frac{\partial^2 z}{\partial t^2} = \mu z + \nu\frac{\partial z}{\partial t} + A|z|^2 z + C(\frac{\partial z}{\partial t}\bar{z} + z\frac{\partial \bar{z}}{\partial t})z + D|z|^2\frac{\partial z}{\partial t}, \tag{3.63}$$

where

$$A = \frac{38}{9}Q_1^2 + 3C_1,\; C = -4bQ_1^2 + C_2,\; D = -\frac{4}{9}bQ_1^2 + C_2. \tag{3.64}$$

Note that A is the same as the coefficient of the amplitude equation for the Swift–Hohenberg equation [20, 69]. Note also that C_4, the coefficient of u_t^3, does not appear at this order but it is important in Lyapunov stability as mentioned in Section 3.3. Equation (3.63) is the TB normal form [34].

So far, the model (3.40) is simple and replicates the linear behaviour of thermosolutal convection. The model satisfies Lyapunov stability and can be reduced to the TB normal form equation (3.63). Thus, we are now in a position to use the results given by [34] to predict the weakly nonlinear behaviour.

3.5 Relating the model to the cases in DK

In last section, we have seen that the model (3.40) with the nonlinearities u^2, u^3, $u^2 u_t$ and u_t^3 can be reduced using weakly nonlinear theory to TB normal form equation with coefficients specified in (3.64). The normal form equation has been studied by [34] as we discussed in Chapter 2. Their work shows that the bifurcation diagrams are divided into different regions depending on the value of the ratio $\frac{D}{M}$ (where $M = 2C + D$), as well as the sign of A (see Figure 2.2). Each case shows different types of stable and unstable solutions. In this section we want to relate our model to the work given by [34] in order to predict the types of solutions. Lyapunov stability require C_1 to be negative and if Q_1 is small then A in (3.64) will be negative. This shows that our model lies in the case where $A < 0$ provided Q_1 is not too large. To determine the case we find the ratio

$$\frac{D}{M} = \frac{\frac{-4}{9} b Q_1^2 + C_2}{2(-4bQ_1^2 + C_2) + \frac{-4}{9} b Q_1^2 + C_2} = \frac{-4bQ_1^2 + 9C_2}{-76bQ_1^2 + 27C_2}. \tag{3.65}$$

We know from Lyapunov stability that C_2 has to be negative and so $D < 0$ and $M < 0$, which refers to the minus cases in [34]. The fraction $\frac{D}{M}$ is always bounded between

$$\frac{1}{19} < \frac{D}{M} < \frac{1}{3}.$$

This indicate that the only case in [34] that can be accessed with $\frac{D}{M}$ in this range is case II$-$ with $A < 0$ (see Figure 2.2).

Figure 3.6 shows the stability diagram for case II$-$ with $A < 0$ from [34]. The trivial solution $z = 0$ is stable when μ and ν are both negative, it loses stability in a pitchfork bifurcation when $L_0 : \mu = 0$ leading to stable SS and in a Hopf

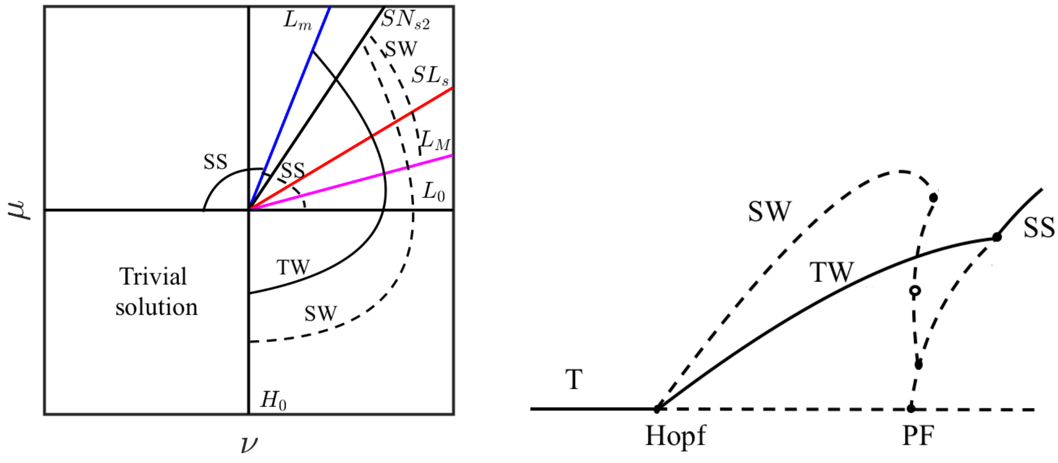

(a) **(b)**

Figure 3.6: (a) Sketch of the stability diagram for case II− with $A < 0$ from [34]; (b) the corresponding bifurcation diagram. The notation is explained in Chapter 2.

bifurcation when $H_0 : \nu = 0$ with $\mu < 0$ leading to stable TW and unstable SW. The pitchfork bifurcation from SS to TW occurs when

$$L_m : \mu = \frac{A}{D}\nu, \qquad \text{with} \qquad A\mu < 0. \tag{3.66}$$

This indicates that the model (3.40) exhibits stable SS and TW solutions only provided Q_1 is not too large. Since we are interested in finding stable SW and MW, which occur in other cases with different values of $\frac{D}{M}$, we will modify our model in the next chapter to allow these cases. Also, we will solve the model (3.40) numerically to obtain the SS and TW solutions.

3.6 Conclusion

A new second order PDE that replicates the linear behaviour of thermosolutal convection has been presented. Just as the Swift–Hohenberg equation is a model for the onset of steady convection, our new model can describe the onset of both steady and oscillatory convection in a simple PDE. Using weakly nonlinear theory, the model can be reduced to the TB normal form equation in which the pitchfork and Hopf bifurcation coincide at the TB point.

Based on the criteria we have mentioned in Section 3.3, the model is simple and reduces to the TB normal form equation. However, the model does not allow stable SW behaviour close to onset. Our model so far gives only the case labelled II$-$ with $A < 0$ by [34], in which only stable SS and TW exist. Our interest in the next chapter is to allow the model to obtain different solutions such as SW and MW, which exist in the normal form when A, D and M are still negative but the fraction $\frac{D}{M}$ take a wider range of values. We are going to modify the model by adding more nonlinearities that will affect the fraction $\frac{D}{M}$ to allow additional cases and then additional solutions.

Chapter 4

The model with different nonlinearities

4.1 Introduction

Thermosolutal convection can exhibit a variety of oscillations including travelling wave (TW), standing wave (SW), modulated wave (MW), as well as steady state (SS). The transitions between these states have been observed both in numerical [36, 52, 62] and experimental [61, 85] investigations. In Chapter 3, we have seen that the PDE (3.40) with the nonlinearities u^2, u^3, u^2u_t and u_t^3 can be reduced to the TB normal form equation using weakly nonlinear analysis and is Lyapunov stable. With this choice of nonlinearities, the TB normal form equation with the coefficients A, C and D (3.64) is limited to the region $0 < \frac{D}{M} < 0.5$ and $A < 0$. In this region (known as case II$-$ in [34]), the normal form predicts stable SS and TW only.

Our interest in this chapter is to make the model more generic in order to access a wide range of cases available in the normal form, as exhibited by thermosolutal and binary convection and the potentially by other problems. Therefore, we want to allow the fraction $\frac{D}{M}$ to match other cases mentioned in [34] and to allow $A > 0$ as well. Since the coefficients D and M are affected by the nonlinearities, in this chapter we will modify the model by adding more nonlinearities, while preserving Lyapunov stability. The model (3.40) with the nonlinearities u^2, u^3, u^2u_t and u_t^3 is Lyapunov stable if the coefficients C_2 and C_4 of u^2u_t and u_t^3 are negative, with the Lyapunov function bounded from below when the coefficient C_1 of u^3 is negative. This indicates that for any new quadratic nonlinearities the model still satisfies Lyapunov stability as long as the cubic terms are dominant. Therefore, in this chapter we will discuss only the quadratic nonlinear terms u_t^2 and uu_{xx}, which come into weakly nonlinear theory. It turns out that the term u_t^2 does not affect the fraction $\frac{D}{M}$, and so it will be removed. In Chapter 5, we will extend the model further by adding cubic nonlinearities $(u_x)^2u_t$ and uu_xu_{xt}.

In Section 4.2 we will apply weakly nonlinear theory as before to identify the coefficients A, C and D. In Section 4.3, we will compute the fraction $\frac{D}{M}$ and discuss the possible cases obtained compared with [34]. In Section 4.4 we will solve the model numerically using Fourier spectral methods and the exponential time differencing (ETD) method. We will show numerical solutions for two cases labelled II$-$ and III$-$ with $A < 0$ in [34]. We will compare the amplitude obtained from weakly nonlinear theory with the amplitude from the numerical solutions. Also, we will compare the stability region obtained from solving the model numerically with the stability region shown in [34].

4.2 Weakly nonlinear theory

In this section, we will use weakly nonlinear theory as before to determine the coefficients A, C, D and M in the normal form (see Section 3.4). Adding the quadratic nonlinear terms u_t^2 and uu_{xx} to the PDE (3.40), we get

$$\begin{aligned}\frac{\partial^2 u}{\partial t^2} = \left(\mu - \left(1+\frac{\partial^2}{\partial x^2}\right)^2\right)u + \left(\nu - b\left(1+\frac{\partial^2}{\partial x^2}\right)^2\right)u_t + Q_1u^2 \\ + Q_2u_t^2 + Q_3uu_{xx} + C_1u^3 + C_2u^2u_t + C_4u_t^3,\end{aligned} \tag{4.1}$$

where μ and ν are the control parameters, Q_1, Q_2, Q_3, C_1, C_2 and C_4 are order 1 constants and $b > 1$. In the weakly nonlinear analysis we use the same scaling we use in Chapter 3

$$\frac{\partial}{\partial t} \to \epsilon\frac{\partial}{\partial t},\ \mu \to \epsilon^2\mu_2,\ \nu \to \epsilon^2\nu_2, \tag{4.2}$$

and expand u as a power series in ϵ as (3.42). We substitute the scaling and the expansion (3.42) into the PDE (4.1), and get the following equation

$$\begin{aligned}&\epsilon^3\frac{\partial^2 u_1}{\partial t^2} + \epsilon^4\frac{\partial^2 u_2}{\partial t^2} + \cdots = \mu_2\left(\epsilon^3u_1 + \epsilon^4u_2 + \cdots\right) \\ &- \left(1+\frac{\partial^2}{\partial x^2}\right)^2\left(\epsilon u_1 + \epsilon^2u_2 + \epsilon^3u_3 + \epsilon^4u_4 + \cdots\right) \\ &+ \nu_2\left(\epsilon^4\frac{\partial u_1}{\partial t} + \cdots\right) - b\left(1+\frac{\partial^2}{\partial x^2}\right)^2\left(\epsilon^2\frac{\partial u_1}{\partial t} + \epsilon^3\frac{\partial u_2}{\partial t} + \epsilon^4\frac{\partial u_3}{\partial t} + \cdots\right) \\ &+ Q_1\left(\epsilon^2u_1^2 + 2\epsilon^3u_1u_2 + \epsilon^4\left(u_2^2 + u_1u_3\right) + \cdots\right) \\ &+ Q_2\left(\epsilon^4\left(\frac{\partial u_1}{\partial t}\right)^2 + \cdots\right) \\ &+ Q_3\left(\epsilon^2u_1\frac{\partial^2 u_1}{\partial x^2} + \epsilon^3\left(u_1\frac{\partial^2 u_2}{\partial x^2} + u_2\frac{\partial^2 u_1}{\partial x^2}\right) + \epsilon^4\left(u_1\frac{\partial^2 u_3}{\partial x^2} + u_2\frac{\partial^2 u_2}{\partial x^2} + u_3\frac{\partial^2 u_1}{\partial x^2}\right) + \cdots\right) \\ &+ C_1\left(\epsilon^3u_1^3 + 3\epsilon^4u_1^2u_2 + \cdots\right) + C_2\left(\epsilon^4u_1^2\frac{\partial u_1}{\partial t} + \cdots\right) + C_4\left(\epsilon^6\frac{\partial u_1}{\partial t} + \cdots\right).\end{aligned} \tag{4.3}$$

As before, at $O(\epsilon)$ we have

$$0 = \mathcal{L}u_1, \tag{4.4}$$

where

$$\mathcal{L} = -\left(1 + \frac{\partial^2}{\partial x^2}\right)^2. \tag{4.5}$$

Solving $\mathcal{L}u_1 = 0$ implies u_1 is a linear combination of e^{ix} and e^{-ix} with $k = 1$ as follows:

$$u_1(x,t) = F_1(t)e^{ix} + \bar{F_1}(t)e^{-ix}, \tag{4.6}$$

At $O(\epsilon^2)$, we get

$$0 = \mathcal{L}u_2 + b\mathcal{L}\frac{\partial u_1}{\partial t} + Q_1 u_1^2 + Q_3 u_1 \frac{\partial^2 u_1}{\partial x^2}. \tag{4.7}$$

There are no e^{ix} terms in (4.7) so we have no solvability condition to satisfy. We solve this by supposing u_2 is of the form

$$u_2(x,t) = G_2(t)e^{2ix} + G_1(t)e^{ix} + G_0(t) + \bar{G_1}(t)e^{-ix} + \bar{G_2}(t)e^{-2ix}, \tag{4.8}$$

where G_0, G_1, G_2 and the complex conjugates $\bar{G_1}, \bar{G_2}$ are time-dependent amplitudes. Substituting (4.6) and (4.8) into (4.7) and comparing the coefficients of the Fourier modes, we get

$$u_2 = \frac{(Q_1 - Q_3)}{9} F_1^2 e^{2ix} + G_1 e^{ix} + 2(Q_1 - Q_3)|F_1|^2 + \bar{G_1} e^{-ix} + \frac{(Q_1 - Q_3)}{9} \bar{F_1}^2 e^{-2ix}. \tag{4.9}$$

At $O(\epsilon^3)$, we have

$$\frac{\partial^2 u_1}{\partial t^2} = \mu_2 u_1 + \mathcal{L}u_3 + b\mathcal{L}\frac{\partial u_2}{\partial t} + 2Q_1 u_1 u_2 + Q_3\left(u_1 \frac{\partial^2 u_2}{\partial x^2} + u_2 \frac{\partial^2 u_1}{\partial x^2}\right) + C_1 u_1^3. \tag{4.10}$$

u_3 is unknown in (4.10). Thus, we assume u_3 as follows:

$$\begin{aligned} u_3(x,t) = {} & H_3(t)e^{3ix} + H_2(t)e^{2ix} + H_1(t)e^{ix} + H_0(t) + \bar{H_1}(t)e^{-ix} + \bar{H_2}(t)e^{-2ix} \\ & + \bar{H_3}(t)e^{-3ix}, \end{aligned} \tag{4.11}$$

where H_0, H_1, H_2, H_3, and the complex conjugates $\bar{H}_1, \bar{H}_2, \bar{H}_3$ are time-dependent amplitudes. This equation has a solvability condition coming from the e^{ix} terms. Substituting (4.6), (4.9) and (4.11) into (4.10) and collecting the coefficient of e^{ix}, we get

$$\frac{\partial^2 F_1}{\partial t^2} = \mu_2 F_1 + A|F_1|^2 F_1, \tag{4.12}$$

where

$$A = (Q_1 - Q_3)\left(\frac{38}{9}Q_1 - \frac{23}{9}Q_3\right) + 3C_1. \tag{4.13}$$

Collecting the coefficients of e^{3ix} components, we get

$$H_3 = \frac{1}{64}\left(\frac{2}{9}Q_1\left(Q_1 - Q_3\right) - \frac{5}{9}Q_3\left(Q_1 - Q_3\right) + C_1\right)F_1^3. \tag{4.14}$$

Collecting the coefficients of e^{2ix} components, we get

$$H_2 = \frac{2\left(Q_1 - Q_3\right)}{9}\left(F_1 G_1 - bF_1\frac{\partial F_1}{\partial t}\right), \tag{4.15}$$

and from the constant coefficient, we get

$$H_0 = 2\left(Q_1 - Q_3\right)\left(F_1\bar{G}_1 + \bar{F}_1 G_1 - b\left(\frac{\partial F_1}{\partial t}\bar{F}_1 + F_1\frac{\partial \bar{F}_1}{\partial t}\right)\right). \tag{4.16}$$

At $O(\epsilon^4)$, we have

$$\begin{aligned}\frac{\partial^2 u_2}{\partial t^2} &= \mu_2 u_2 + \mathcal{L}u_4 + \nu_2\frac{\partial u_1}{\partial t} + b\mathcal{L}\frac{\partial u_3}{\partial t} + Q_1\left(u_2^2 + 2u_1u_3\right) + Q_2\left(\frac{\partial u_1}{\partial t}\right)^2 \\ &+ Q_3\left(u_1\frac{\partial^2 u_3}{\partial x^2} + u_2\frac{\partial^2 u_2}{\partial x^2} + u_3\frac{\partial^2 u_1}{\partial x^2}\right) + 3C_1u_1^2u_2 + C_2u_1^2\frac{\partial u_1}{\partial t}.\end{aligned} \tag{4.17}$$

The solvability condition is the e^{ix} component of (4.17), which gives

$$\begin{aligned}\frac{\partial^2 G_1}{\partial t^2} &= \mu_2 G_1 + \nu_2 \frac{\partial F_1}{\partial t} + N F_1^2 \bar{G}_1 + P|F_1|^2 G_1 + C\left(\frac{\partial F_1}{\partial t}\bar{F}_1 + F_1 \frac{\partial \bar{F}_1}{\partial t}\right) F_1 \\ &\quad + D|F_1|^2 \frac{\partial F_1}{\partial t},\end{aligned} \tag{4.18}$$

where

$$N = (Q_1 - Q_3)\left(\frac{38}{9}Q_1 - \frac{23}{9}Q_3\right) + 3C_1, \tag{4.19}$$

$$P = (Q_1 - Q_3)\left(\frac{76}{9}Q_1 - \frac{62}{9}Q_3\right) + 6C_1, \tag{4.20}$$

$$C = 2b\,(Q_1 - Q_3)\,(-2Q_1 + Q_3) + C_2, \tag{4.21}$$

$$D = b\,(Q_1 - Q_3)\left(\frac{-4}{9}Q_1 + \frac{10}{9}Q_3\right) + C_2. \tag{4.22}$$

Note that, the term u_t^2 with the coefficient Q_2 does not contribute to (4.18) since there is no e^{ix} component in $\left(\frac{\partial u_1}{\partial t}\right)^2$. We use a reconstitution procedure to combine equations (4.12) and (4.18) into a single PDE and write

$$z = \epsilon F_1 + \epsilon^2 G_1. \tag{4.23}$$

By unscaling time and the parameters according to

$$\frac{\partial}{\partial t} \to \frac{1}{\epsilon}\frac{\partial}{\partial t} \qquad \mu_2 \to \frac{1}{\epsilon^2}\mu \qquad \text{and } \nu_2 \to \frac{1}{\epsilon^2}\nu. \tag{4.24}$$

We get

$$\begin{aligned}\frac{\partial^2 z}{\partial t^2} &= \mu z + \epsilon\nu \frac{\partial F_1}{\partial t} + \epsilon^3 A|F_1|^2 F_1 + \epsilon^4 N F_1^2 \bar{G}_1 + \epsilon^4 P|F_1|^2 G_1 \\ &\quad + \epsilon^3 C\left(\frac{\partial F_1}{\partial t}\bar{F}_1 + F_1\frac{\partial \bar{F}_1}{\partial t}\right) F_1 + \epsilon^3 D|F_1|^2 \frac{\partial F_1}{\partial t}.\end{aligned} \tag{4.25}$$

Substituting $F_1 = \frac{z}{\epsilon} - \epsilon G_1$ in (4.25) and neglecting all the terms proportional to

ϵ, we get the TB normal form

$$\frac{\partial^2 z}{\partial t^2} = \mu z + \nu \frac{\partial z}{\partial t} + A|z|^2 z + C(\frac{\partial z}{\partial t}\bar{z} + z\frac{\partial \bar{z}}{\partial t})z + D|z|^2\frac{\partial z}{\partial t}, \tag{4.26}$$

where A, C and D are given by (4.13), (4.21) and (4.22), respectively. Since the coefficient Q_2 for the term u_t^2 does not appear in the coefficients A, C and D, we will drop this term from the PDE (4.1) and we will accept the contribution from the term uu_{xx}. Then the PDE takes the following form

$$\begin{aligned}\frac{\partial^2 u}{\partial t^2} = &\left(\mu - \left(1 + \frac{\partial^2}{\partial x^2}\right)^2\right) u + \left(\nu - b\left(1 + \frac{\partial^2}{\partial x^2}\right)^2\right) u_t + Q_1 u^2 \\ &+ Q_3 u u_{xx} + C_1 u^3 + C_2 u^2 u_t + C_4 u_t^3. \end{aligned}\tag{4.27}$$

As we discussed in Chapter 3, for stability we require $C_2 < 0$ and $C_4 < 0$ and to make the Lyapunov function bounded below we require $C_1 < 0$. In next section we will discuss the fraction $\frac{D}{M}$ in more detail.

4.3 Relating the model to the cases in DK

The authors in [34] show that the normal form exhibits a wide range of behaviour depending on the sign of the coefficients A, D and M and the value of the fraction $\frac{D}{M}$ where $M = 2C + D$. The bifurcation diagram changes at special values of $\frac{D}{M} = c$ where $c = \frac{1}{5}, \frac{1}{2}, 0.7, 0.74, \frac{3}{4}, \frac{4}{5}, 1$. The regions between the lines $\frac{D}{M} = c$ in the (D, M)-plane are enumerated with roman numeral I$\pm$, XII$\pm, \cdots$ in [34] (see Figure 2.2).

In this section, we compute the fraction $\frac{D}{M}$ in order to relate the model (4.27) to the normal form cases. From (4.21) and (4.22), the fraction $\frac{D}{M}$ is

$$\frac{D}{M} = \frac{\frac{-4}{9}bQ_1^2 + \frac{14}{9}bQ_1Q_3 - \frac{10}{9}bQ_3^2 + C_2}{\frac{-76}{9}bQ_1^2 + \frac{122}{9}bQ_1Q_3 - \frac{46}{9}bQ_3^2 + 3C_2}, \tag{4.28}$$

where $M = 2C + D$. Lyapunov stability requires C_1, C_2 and C_4 to be negative. Take for example $C_1 = C_2 = C_4 = -1$ and $b = 2$. By plotting contours of A and $\frac{D}{M} = c$, where $c = \frac{1}{5}, \frac{1}{2}, 0.7, 0.74, \frac{3}{4}, \frac{4}{5}, 1$, we can obtain the normal form cases. Figure 4.1 shows that, with the new nonlinear term uu_{xx}, the fraction $\frac{D}{M}$ can access all values of the non-degeneracy condition c with $A < 0$, and cases II$-$ and III$-$ with $A > 0$. In Table 4.1 we show values of Q_1 and Q_3 obtained from Figure 4.1 that correspond to the different cases in [34], along with the coefficients A, D and M from (4.13), (4.21) and (4.22) where $M = 2C + D$. Note that without the term uu_{xx} the only case we obtain is II$-$ with $A < 0$ as we have mentioned in Chapter 3.

We can conclude that the nonlinearities $u^2, uu_{xx}, u^3, u^2u_t$ and u_t^3 allow a wide range of weakly nonlinear behaviour. Then the current model with these nonlinearities is

$$\begin{aligned}\frac{\partial^2 u}{\partial t^2} = \left(\mu - \left(1 + \frac{\partial^2}{\partial x^2}\right)^2\right) u + \left(\nu - b\left(1 + \frac{\partial^2}{\partial x^2}\right)^2\right) u_t + Q_1 u^2 \\ + Q_3 uu_{xx} + C_1 u^3 + C_2 u^2 u_t + C_4 u_t^3,\end{aligned} \tag{4.29}$$

where μ and ν are the control parameters, Q_1, Q_3, C_1, C_2 and C_4 are constants, $b > 1$, and the term $Q_2 u_t^2$ has been dropped.

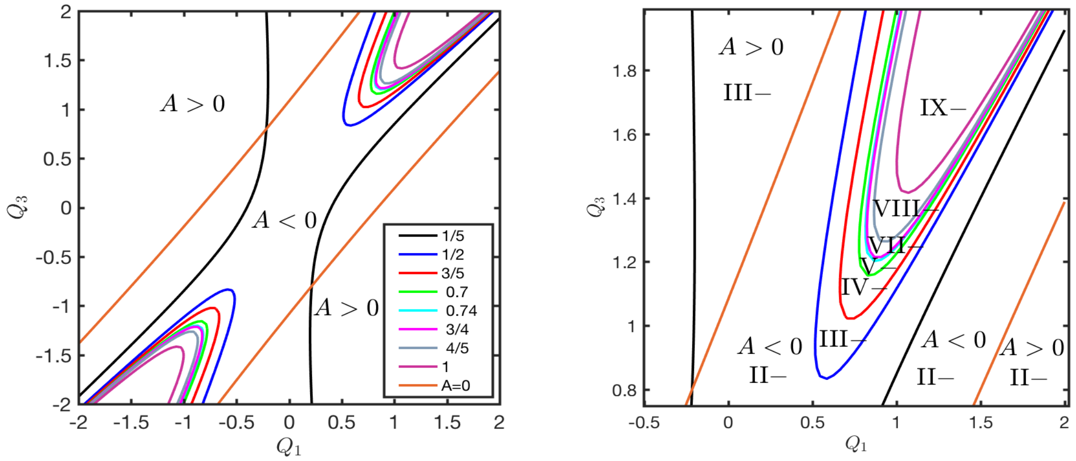

Figure 4.1: Plot of contours of A in orange from (4.13) and the different values of $\frac{D}{M} = c$ where $c = \frac{1}{5}, \frac{1}{2}, \frac{3}{5}, 0.7, 0.74, \frac{3}{4}, \frac{4}{5}$ from (4.28) where $C_1 = C_2 = C_4 = -1$ and $b = 2$. The regions between each curve correspond to the enumerated II−,...IX− in [34]. The right panel shows a zoom of the top right corner of the left panel.

	Q_1	Q_3	A	M	D	$\frac{D}{M}$	Case in DK
$A > 0$	1.5	0.5	2.056	-23.22	-1.22	0.05	II−
	0.1	1.5	1.78	-22.1	-5.54	0.25	III−
$A < 0$	0.5	0	-1.94	-7.22	-1.22	0.17	II−
	0.6	0.9	-3.07	-2.72	-1.44	0.53	III−
	0.8	1.1	-3.17	-2.32	-1.52	0.66	IV−
	0.85	1.2	-3.18	-2.27	-1.67	0.736	V−
	0.9	1.21	-3.27	-2.12	-1.58	0.74	VI−
	0.9	1.25	-3.21	-2.15	-1.69	0.78	VII−
	1	1.4	-3.26	-1.97	-1.89	0.96	VIII−
	1.1	1.5	-3.32	-1.702	-1.942	1.14	IX−

Table 4.1: In this table we show example of different values of Q_1 and Q_3. The values taken from Figure 4.1. We compute the coefficients A, D, M from (4.13), (4.21), (4.22) and the fraction $\frac{D}{M}$ from (4.28). In the last column we show the corresponding case in [34].

4.4 Numerical results

In this section, we present numerical solutions of the model (4.29). To treat the model numerically, we discretize the PDE both in time and space. In space, we discretize the model using spectral methods [24, 30, 46, 50] and fast Fourier transform (FFT). In time, we discretize the model (4.29) using the exponential time differencing method (ETD) [24, 30, 46, 50]. The ETD method solves the linear parts of the PDEs exactly followed by a second order approximation of the nonlinear parts. Further explanation can be seen in Appendix A.

To obtain the solutions behaviour close to the TB point, we solve the PDE with 32 grid points with one-wavelength in one dimensional domain using random initial conditions. In this section, we will show the result in two cases. First, when $Q_1 \neq 0$ and $Q_3 = 0$, the PDE then reverts to (3.40) where the normal form shows only stable SS and TW (case labelled II− with $A < 0$ in [34]). Secondly, when $Q_1 \neq 0$ and $Q_3 \neq 0$, which the normal form gives a wider range of solutions behaviour: we focus on case III− with $A < 0$, in which the normal form exhibits stable SW and MW as well as SS and TW.

During this dissertation, we compare the stability region from solving the model with the stability region obtained from the normal form [34]. To do this we solve the PDE and plot the type of solutions in (ν, μ)-plane, using polar coordinates defined by

$$\nu = d\cos(\theta), \qquad \mu = d\sin(\theta), \tag{4.30}$$

where d is the radius that controls how far ν and μ are from the TB point, and θ is the angle that controls the position of ν and μ in the (ν, μ)-plane. Moreover, we show the bifurcation diagram from numerical simulations, plotting the amplitude as a function of the control parameter θ with fixed d. Note that the Hopf bifurcation occurs at $\nu = 0$ and $\mu < 0$ which correspond to $\theta = 270°$. The pitchfork bifurcation occurs at $\mu = 0$ which correspond to $\theta = 0°$ and $\theta = 180°$.

4.4.1 Example solutions

Close to the TB point, four types of solutions can be shown including SS, TW, SW and MW as well as the trivial state, as mentioned in Section 2.2. In this section, we will show examples of these solutions in time evaluation and in space for small domain with one wavelength.

- **Trivial solution (T)**: In a time-dependent model the trivial solution being stable means all small trajectories in $\hat{u}$ and $\hat{u}_t$ go toward zero.
- **Steady state solution (SS)**: The SS solutions are the state that describes the behaviour of the system when the solution remains unchanged in time with $\hat{u}_t = 0$ (see Figure 4.2 a).
- **Travelling waves (TW)**: In time-dependent systems the TW solutions have a constant amplitude and a constant frequency ω in the asymptotic limit (see Figure 4.2 b).
- **Standing waves (SW)**: The SW solutions mean there are oscillations in the amplitude for both $\hat{u}$ and $\hat{u}_t$ as a function of time. When the solutions reach the asymptotic state the oscillations occur where the maximum amplitude does not vary further as time increases (see Figure 4.2 c).
- **Modulated waves (MW)**: The MW solutions have also an oscillation in amplitude for both $\hat{u}$ and $\hat{u}_t$. The asymptotic amplitude of the wave is modulated means that there is a long wavelength modulation of the amplitude as time varies (see Figure 4.2 d).

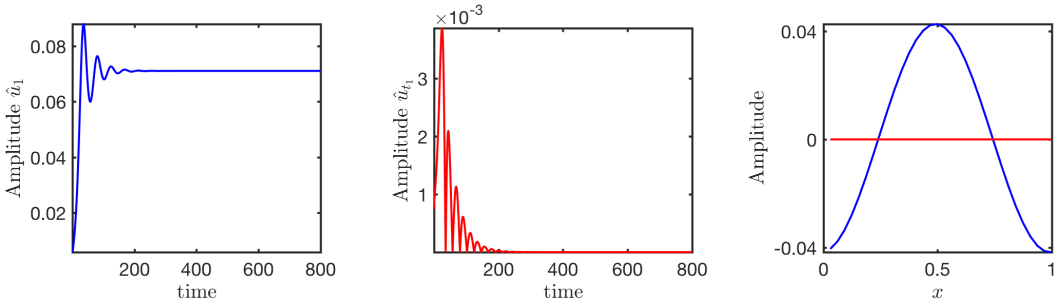

(a) Steady state

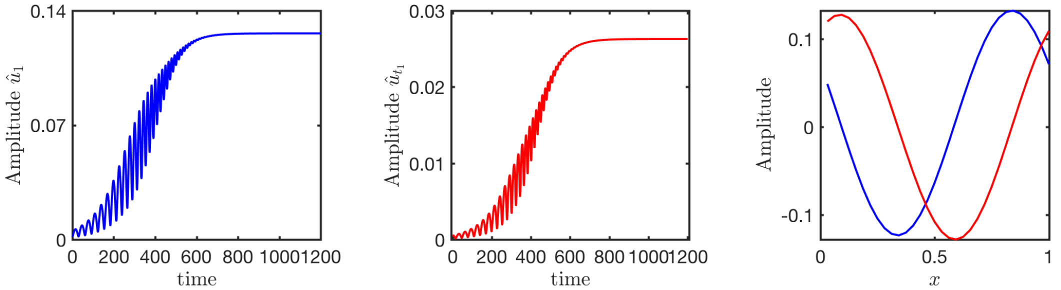

(b) Travelling wave

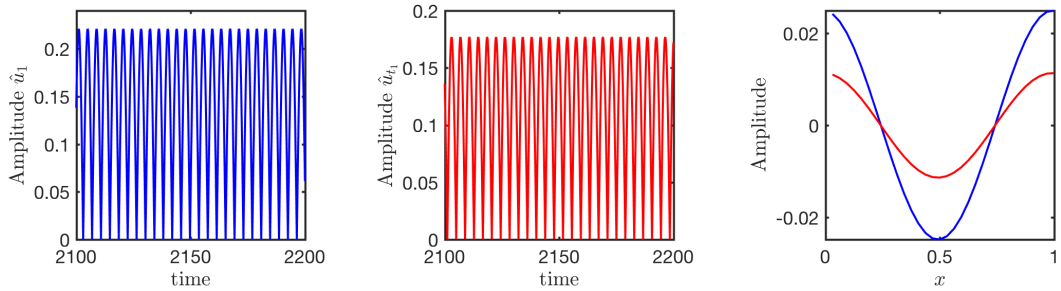

(c) Standing wave in the asymptotic state

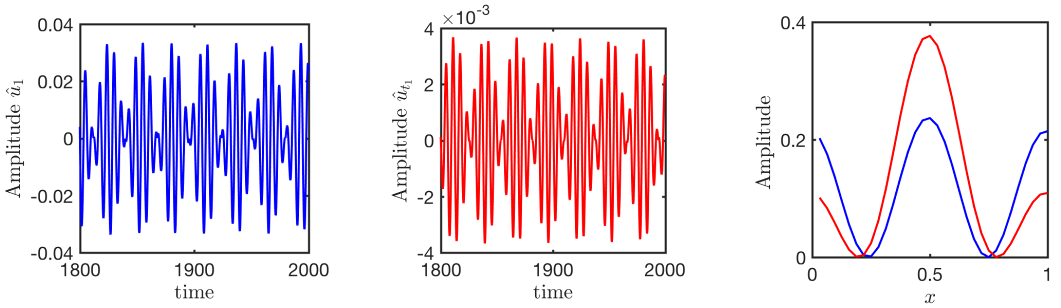

(d) Sketch of modulated wave in the asymptotic state

Figure 4.2: Example of solutions in time-dependent system. The solutions (a,b,c) obtained from solving the PDE (4.29) using time-stepping method where $Q_1 = 0.6, Q_3 = 0.9$, $C_1, C_2, C_4 = -1$, and $b = 2$ allowing one wavelength with 32 grid points. The MW solution (d) is not a real solution but it is sketch since there is no MW obtained from solving the PDE (4.29). The left-hand and middle panels show the amplitude of $\hat{u}_1$ and $\hat{u}_{t_1}$ of the first Fourier mode ($k = 1$). The right-hand panels show the amplitude of u (in blue) and u_t (in red) in physical space with all mode of k.

4.4.2 Stopping criterion and classification criteria

When we start our time-stepping from random initial conditions using rand function in Matlab which generates arrays of random numbers whose elements are uniformly distributed in the interval $(0, 1)$, we need a stopping criterion to identify when we have reached an asymptotic state. However, the normal form shows five types of solutions: T, SS, TW, SW and MW (see Chapter 2 and Section 4.4.1). We also expect such states to exist in the PDE model. Therefore, once an asymptotic state has been reached, we need to apply a classification criterion to determine the type of solution. During time-stepping, starting at $t = 0$ with a time step of 0.01, we advance the evolution by 200 time units. When $t = 200$, we calculate the value of $z_{pre} = |\max(\hat{u}_1) - \min(\hat{u}_1)|$. We again advance the evolution from $t = 200$ to $t = 400$ when we again compute $z_{cur} = |\max(\hat{u}_1) - \min(\hat{u}_1)|$. Here $\hat{u}_1$ is the amplitude of the first Fourier mode ($k = 1$).

We check to see if the difference between z_{pre} and z_{cur} is more than the tolerance of $\tau = 10^{-8}$. If the difference is more than the tolerance, then we determine that the evolution has not yet reached an asymptotic state. Then we update the value of z_{pre} with z_{cur} and again time step for another 200 time units. At the end of the time-stepping, we again recompute z_{cur} and repeat the above check to see if the value of $|z_{pre} - z_{cur}| < \tau$. If this condition is not satisfied, we update the value of z_{pre} and repeat time-stepping. On the other hand, if this condition is satisfied, we determine that we have reached an asymptotic state and move on to try and classify the obtained solution using conditions from Table 4.2.

We set the condition of the solutions in Table 4.2 based on the behaviour of each solution from Figure 4.2. We implement the conditions in code to check first the condition of the trivial state then the SS, TW, SW and if none of the above conditions are satisfied we check if the solution is MW. However, this classification criteria works well in obtaining the type of solution for our model (4.29) but it

Class of Solution	Condition of Solution at asymptotic state	Numerical Implementation of Condition
T	$\hat{u}_1 = 0, \hat{u}_{t_1} = 0$	$\lvert\hat{u}_1\rvert_{t=200n} < \tau$ & $\lvert\hat{u}_{t_1}\rvert_{t=200n} < \tau$
SS	$\hat{u}_1 = c, \hat{u}_{t_1} = 0$	$\lvert\hat{u}_1\rvert_{t=200n} > \tau$ & $\lvert\hat{u}_{t_1}\rvert_{t=200n} < \tau$
TW	$\hat{u}_1 = c, \hat{u}_{t_1} = c$	$[\max(f) - \min(f)] < \tau$ & $[\max(f_t) - \min(f_t)] < \tau$
SW	$\hat{u}_1 \neq c, \hat{u}_{t_1} \neq c$, $\lvert z_{pre} - z_{cur}\rvert = c$	$[\max(f) - \min(f)] > \tau$ & $[\max(f_t) - \min(f_t)] > \tau$
MW	$\hat{u}_1 \neq c, \hat{u}_{t_1} \neq c$, $\lvert z_{pre} - z_{cur}\rvert \neq c$	- if none of the above are satisfied -

Table 4.2: Conditions for a variety of classes of solutions for the model (4.29) where $\hat{u}_1$ and $\hat{u}_{t_1}$ are the amplitude at asymptotic state of the first Fourier mode ($k = 1$). The c here indicates a constant. Here $f = (\hat{u}_{1_{t=200(n-1)}} \text{ to } \hat{u}_{1_{t=200n}})$ and $f_t = (\hat{u}_{t_{1_{t=200(n-1)}}} \text{ to } \hat{u}_{t_{1_{t=200n}}})$, where n is a constant.

might be not a good criterion for other problems. Therefore, once the time-stepping reaches the asymptotic state we also check that the solution we get satisfies the condition we implemented by eye to make sure that we get the correct type of solution.

4.4.3 Numerical results: case II$-$ with $A < 0$

This case can obtained by setting $Q_1 = 0.5, Q_3 = 0$, $C_1 = C_2 = C_4 = -1$, and $b = 2$, in the PDE (4.29) (see Table 4.1). In this case, the normal form shows stable SS in the region between the pitchfork bifurcation line $L_0 : \mu = 0, \nu < 0$ to the half line L_m where the bifurcation changes to TW solutions at

$$L_m : \frac{\mu}{\nu} = \frac{A}{D} = \frac{-1.94}{-1.22} = 1.59, \qquad \mu > 0, \nu > 0. \tag{4.31}$$

The TW are stable in the region between the half line L_m to the half line H_0 : $\nu = 0$ where $\mu < 0$ (see Figure 3.6).

From solving the PDE (4.29) using the time-stepping method, we show the type of solution in (ν, μ)-plane (see Figure 4.3 a) in order to compare with the stability diagram for the normal form [34] (see Figure 3.6 a). Also, we plot the amplitude against θ, where θ controls the position of μ and ν in the (ν, μ)-plane (see Figure 4.3 b) in order to compare with the bifurcation diagram with the normal form (see Figure 3.6 b). In Figure 4.3 (b) we also compute the amplitude for the SS and TW solutions from weakly nonlinear theory as solid and dashed red and blue lines where

$$\begin{aligned} |u| &= \sqrt{\frac{-\mu}{A}}, && \text{amplitude of SS,} \\ |u| &= \sqrt{\frac{-\nu}{D}}, && \text{amplitude of TW,} \end{aligned} \tag{4.32}$$

(see Section 2.2), in order to compare the amplitude from numerical estimation with the amplitude from weakly nonlinear theory for the SS and TW solutions. The comparison will be discussed further in Section 4.4.5.

Starting from random initial conditions close to the pitchfork bifurcation at $\theta = 180^\circ$ with fixed radius 0.01, we find that the SS solutions exist in the region between the pitchfork bifurcation line $L_0 : \mu = 0, \nu < 0$ to the half line L_m. The solutions then change to TW after passing the half line L_m and terminate at the Hopf bifurcation $\theta = 270^\circ$ $(\nu = 0, \mu < 0)$. The trivial solutions are stable in the region where $\mu < 0$ and $\nu < 0$. Figure 4.3 (a) shows that the stability region for SS (x red) and TW (+ blue) agree exactly with the stability region given by the normal form (see Figure 3.6 a). Also, Figure 4.3 (b) shows that the amplitude for SS and TW solutions from weakly nonlinear theory agree with the numerical estimation for the PDE (4.29); further discussion is in Section 4.4.5.

4.4.4 Numerical results: case III$-$ with $A < 0$

In this case the normal form shows stable SS, TW, SW, MW as well as the trivial state (see Figure 4.4). The SS solutions are stable in the region between the half

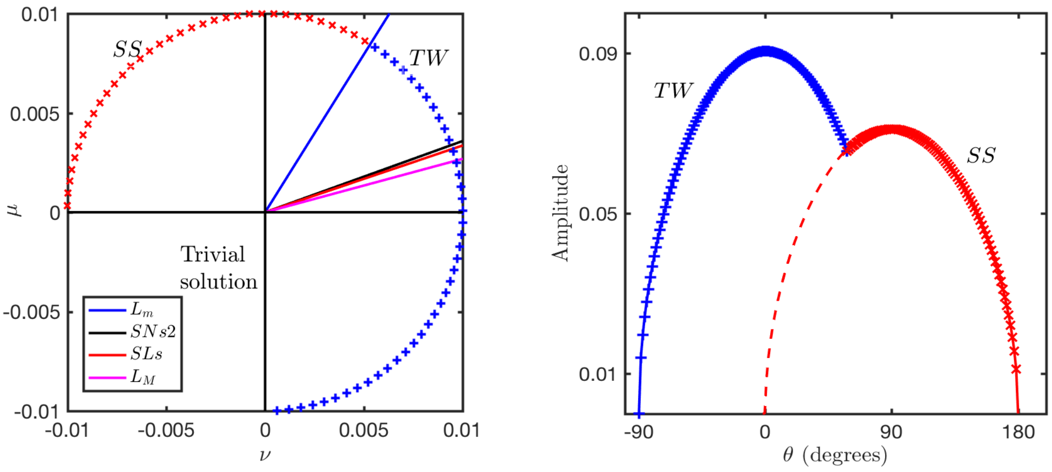

(a) **(b)**

Figure 4.3: The solutions obtained from solving the PDE (4.29) using time-stepping with $Q_1 = 0.5, Q_3 = 0, C_1, C_2, C_4 = -1$, and $b = 2$. (a) Plotting the solution type in (ν, μ)-plane where the x red and + blue indicate SS and TW solutions, respectively. The bifurcation lines L_m, SN_s, SL_s and L_M set in the same order as in the stability diagram for the normal form (see Figure 3.6 a). The notation is explained in Chapter 2. (b) Plotting the amplitude of SS and TW for the PDE (4.29) vs θ. The x red and + blue points represent the estimated amplitude for SS and TW, respectively. The solid red and blue curves represent the amplitude computed from weakly nonlinear theory for SS and TW solutions, respectively. The dashed red curve represents the unstable SS solutions compute from the weakly nonlinear theory (which is $\sqrt{\frac{-\mu}{A}}$ where $A = -1.94$).

line $L_0 : \mu = 0$ and $\nu < 0$ to the half line L_m where

$$L_m : \frac{\mu}{\nu} = \frac{A}{D} \qquad \mu > 0, \nu > 0. \tag{4.33}$$

The TW solutions are stable in the region between the half line L_m to the half line L_H where

$$L_H : \frac{\mu}{\nu} = \frac{3M - 5D}{2M - 4D}\frac{A}{D}, \qquad \nu > 0, \mu < 0. \tag{4.34}$$

The MW solutions are stable between the half line L_H and L_{S2} where

$$L_{S2} : \frac{\mu}{\nu} \approx \frac{A}{0.74D}, \qquad \nu > 0, \mu < 0. \tag{4.35}$$

The stable SW solutions are stable in the region between the half line L_{S2} to the half line $H_0 : \nu = 0, \mu < 0$ at the Hopf bifurcation.

Setting $Q_1 = 0.6, Q_2 = 0.9$, $C_1 = C_2 = C_4 = -1$, and $b = 2$ in the PDE (4.29) (see Table 4.1) the model then represent case III$-$ with $A < 0$ in [34]. With this choice the coefficients of the normal form are $A = -3.07, D = -2.72$ and $M = -1.44$ (see Table 4.1). In Table 4.3, we compute the stability region depending on the coefficients of the nonlinearities in the model

Class of solution	Stability region from the normal form	Stability region from the model
SS	$\frac{\mu}{\nu} > L_m$ to L_0	$\frac{\mu}{\nu} > 2.13$ to $\mu = 0, \nu < 0$
TW	$L_H < \frac{\mu}{\nu} < L_m$	$-6.395 < \frac{\mu}{\nu} < 2.13$
MW	$L_{s2} < \frac{\mu}{\nu} < L_H$	$-6.529 < \frac{\mu}{\nu} < -6.395$
SW	$\frac{\mu}{\nu} < L_{s2}$ to H_0	$\frac{\mu}{\nu} < -6.529$ to $\nu = 0, \mu < 0$

Table 4.3: The stability region for different class of solutions from the normal form for case III$-$ with $A < 0$ in [34]. The table shows the stability region for the model with the choice of nonlinearities $Q_1 = 0.6, Q_2 = 0.9, C_1 = C_2 = C_4 = -1$, and $b = 2$ where the normal form coefficients are $A = -3.07, D = -2.72$ and $M = -1.44$.

Similarly, starting from random initial conditions close to the pitchfork bifurcation at $\theta = 180°$ with fixed radius 0.01, we plot the numerical solutions in the (ν, μ)-plane. Figure 4.5 shows that the stability regions for SS, TW and SW solutions agree exactly with the stability regions from the normal form (see Figure 4.4). The region where the MW are stable is narrow in the normal form and we have been unable to find any MW solutions in the PDE.

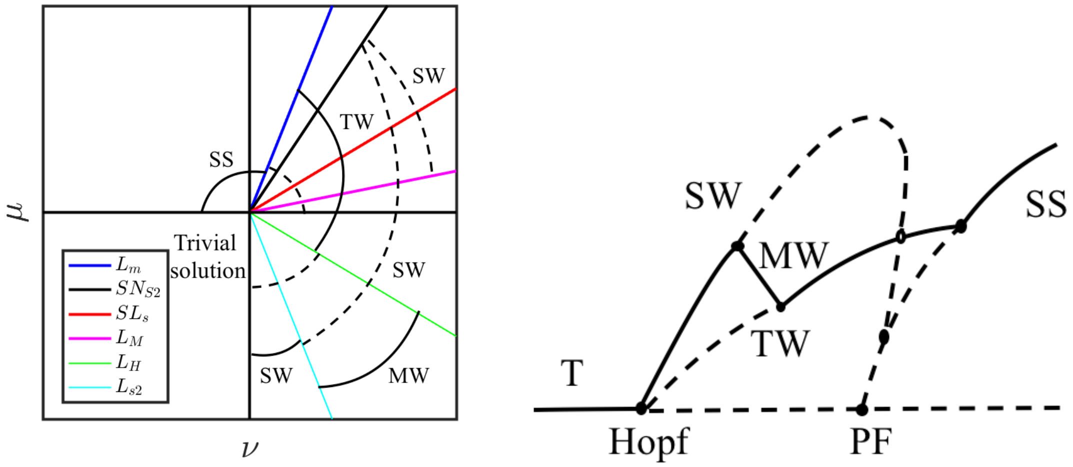

(a) **(b)**

Figure 4.4: (a) Sketch of the stability diagram for case labelled III− with $A < 0$ in [34] and (b) the corresponding bifurcation diagram. The notation is explained in Chapter 2.

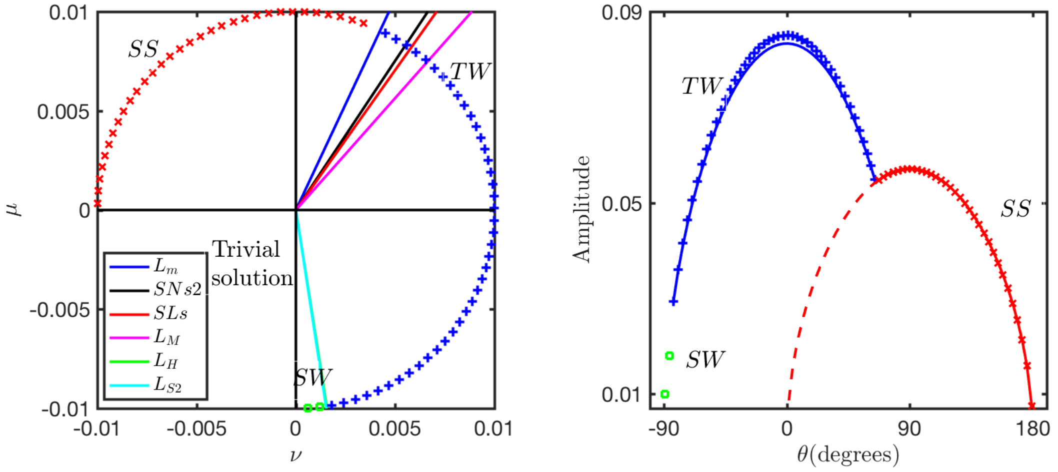

Figure 4.5: The solutions obtained from solving the PDE (4.29) using time-stepping method where $Q_1 = 0.6, Q_3 = 0.9$, $C_1, C_2, C_4 = -1$, and $b = 2$. (a) Plotting the solution type in (ν, μ)-plane where the x red, + blue and square green indicate to SS, TW and SW solutions, respectively. The bifurcation lines $L_m, SN_s, SL_s, L_M, L_H$ and L_{s2} set in the same order as in the stability diagram for the normal form (see Figure 4.4 a). The notation is explained in Chapter 2. (b) Plotting the amplitude of SS, TW and SW for the PDE (4.29) vs θ. The x red, + blue and square green points represent the estimated amplitude for SS, TW and SW, respectively. The solid red and blue curves represent the amplitude computed from weakly nonlinear theory for SS and TW solutions (4.32), respectively. The dashed red curve represents the unstable SS solutions computed from the weakly nonlinear theory (which is $\sqrt{\frac{-\mu}{A}}$ where $A = -3.07$).

4.4.5 Comparing the weakly nonlinear amplitude with numerical amplitude

In this section, we compare the amplitude from numerical estimation with the amplitude from weakly nonlinear theory. From weakly nonlinear theory (see Section 4.2), we scaled μ and ν according to

$$\mu \to \epsilon^2 \mu_2 \qquad \nu \to \epsilon^2 \nu_2 \tag{4.36}$$

and expand u in terms of small ϵ as

$$u_{wnl} = \epsilon u_1 + O(\epsilon^2), \tag{4.37}$$

where

$$u_1 = F_1(t) e^{ix} + c.c, \tag{4.38}$$

and F_1 is time-dependent amplitude as follows

$$|F_1| = \begin{cases} \sqrt{\frac{-\mu_2}{A}} & \text{for} \quad \text{SS}, \\ \\ \sqrt{\frac{-\nu_2}{D}} & \text{for} \quad \text{TW}, \end{cases} \tag{4.39}$$

Substituting (4.38) into (4.37), we obtain the weakly nonlinear amplitude for SS and TW solutions with mode $k = 1$ as follows:

$$u_{wnl} = \begin{cases} \sqrt{\frac{-\mu}{A}}\,(e^{ix} + c.c) + O(\mu) & \text{for SS}, \\ \\ \sqrt{\frac{-\nu}{D}}\,(e^{ix} + c.c) + O(\nu) & \text{for TW}, \end{cases} \tag{4.40}$$

where μ and ν are unscaled parameters. Therefore, we expect the difference between the numerical amplitude u_{num} with mode $k = 1$, (which includes terms

ν	μ	$\epsilon = \sqrt{\mu}$	u_{num}	u_{wnl}	The difference $\lvert u_{num} - u_{wnl}\rvert$	ratio	log(ϵ)	log(ratio-1)
-0.000872	0.009962	0.099810	0.070910	0.071577	0.000667	1.0094	-2.304491	-4.666250
-0.005250	0.008511	0.092256	0.065629	0.066160	0.000531	1.0081	-2.383188	-4.8158741
-0.008511	0.005250	0.072455	0.051697	0.051960	0.000263	1.0051	-2.624786	-5.281236
-0.009962	0.000872	0.029522	0.021153	0.021171	0.000018	1.00085	-3.522614	-7.052100

(a) Comparison for SS solutions.

ν	μ	$\epsilon = \sqrt{\nu}$	u_{num}	u_{wnl}	The difference $\lvert u_{num} - u_{wnl}\rvert$	ratio	log(ϵ)	log(ratio-1)
0.00866	-0.005	0.09306	0.08411	0.08417	0.00006	1.00071	-2.37451	-7.13412
0.00574	-0.00819	0.07573	0.06845	0.06850	0.00005	1.00073	-2.58052	-7.16572
0.00174	-0.00985	0.04167	0.03768	0.03769	0.00001	1.00026	-3.17795	-8.39277

(b) Comparison for TW solutions.

Table 4.4: Comparison of amplitudes computed from PDE simulations and amplitudes from weakly nonlinear theory, with $Q_1 = 0.5, Q_3 = 0, C_1 = C_2 = C_4 = -1$, and $b = 2$ (case II$-$, $A < 0$). See also Figure 4.3.

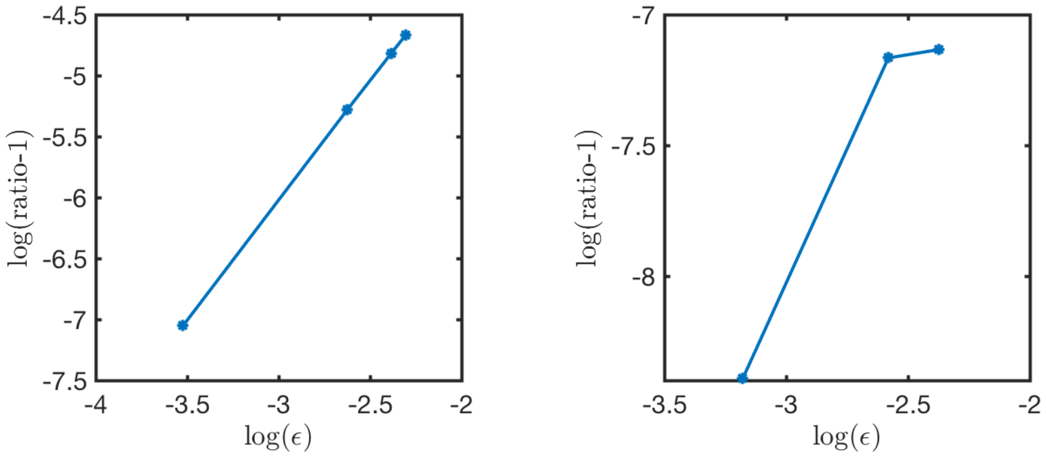

(a) **(b)**

Figure 4.6: Plotting the log of ϵ vs log of (ratio-1) (a) for the SS solutions and (b) for the TW solutions from Table 4.4.

of all orders) and the weakly nonlinear amplitude u_{wnl} (which includes only terms of order ϵ) is $O(\mu)$ in SS solutions and $O(\nu)$ in TW solutions. Consequently, we expect the ratio of the two amplitudes is $1 + O(\epsilon) = 1 + O(\sqrt{\mu})$ for SS solutions and $1 + O(\epsilon) = 1 + O(\sqrt{\nu})$ for TW solutions.

In Table 4.4, we show the amplitude from weakly nonlinear theory and the estimated amplitude at mode $k = 1$ (a) for SS solutions and (b) for TW solutions from solving the PDE using time-stepping method and with parameter values result in case II$-$ with $A < 0$ (see Section 4.4.3). The ratio between the numerical amplitude with mode $k = 1$ and the weakly nonlinear amplitude is better than we expect: it is $1 + O(\mu)$ rather than $1 + O(\sqrt{\mu})$ for SS solutions. The reason is that the $O(\sqrt{\mu})$ correction to this difference is proportional to G_1 (in Eq. (4.8)) which for SS and TW is zero. The TW results are even so better than expected; this may be because ϵ is not small enough for the asymptotic result to hold. We represent the results in Figure 4.6. The figure shows the plotting of $\log(\epsilon)$ against log(ratio-1) for (a) the SS and (b) the TW solutions from Table 4.4. From the figure, we find that the slope of the SS solutions is around 1.95 where it should be around 1 this because the ratio between the numerical amplitude with mode $k = 1$ and the weakly nonlinear amplitude is $1 + O(\mu)$ rather than $1 + O(\epsilon)$.

4.5 Conclusion

In this Chapter, we extended the model by adding more nonlinearities in order to explore a wider range of solutions found in the normal form. The model (4.29) with the nonlinearities u^2, uu_{xx}, u^3, u^2u_t and u_t^3 and the coefficients Q_1, Q_3, C_1, C_2 and C_4 can access cases II$-$ and III$-$ with $A > 0$ and $M < 0$ and cases II$-$ to IX$-$ with $A < 0$ and $M < 0$. Because of the Lyapunov stability requirement we are not able to access the cases with $M > 0$. Also, we are not able to access to case I$-$ with $A > 0$ and $A < 0$ (which require $\frac{D}{M} < 0$, with $D > 0$ and $M < 0$) and case IV$-$ with $A > 0$ (which requires $\frac{D}{M} > \frac{1}{2}$, with $D < 0$ and $M < 0$) because the nonlinearities $u^2, uu_{xx}, u^3, u^2u_t$ and u_t^3 allow A to be positive (with a limited range $0 < \frac{D}{M} < \frac{1}{2}$, where $D < 0$ and $M < 0$) and negative (with a limited range $\frac{D}{M} > 0$, where $D < 0$ and $M < 0$).

We solved the PDE numerically using spectral method and the ETD method.

We obtained three type of solutions: SS, TW and SW. We found a good agreement between the numerical simulations and the estimated amplitudes obtained from weakly nonlinear analysis, for both the SS and the TW solutions. In order to make the comparison easy we plotted the stability diagram as in [34] for our PDE. The comparison shows that our results are consistent with the results shown in [34] including the types of solutions and the stability region at small values of (ν, μ)-plane. The only difference was the MW; these occur in the normal form in a narrow region between the half line L_H and L_{S2}, but we did not find stable MW in the PDE.

Chapter 5

Localized states in the model

5.1 Introduction

In Chapter 4, we solved the model numerically in a small domain. At suitable parameters values, the model shows extended stable states for travelling wave (TW), standing wave (SW) and steady state (SS). The extended solutions refer to solutions that fill the domain. The normal form has subcritical bifurcations to TW, SW and SS, which suggests that stable large-amplitude patterns might exist at the same parameter values as the stable zero solution, and so in a large domain, it might be possible to find localized states. Localized states refer to the state where the pattern is localized in one part of the domain in a background of some other pattern or the zero solution. In an infinite domain, the branch of spatially localized states appears via a bifurcation from trivial state at the same point as the subcritical periodic state, often leading to homoclinic snaking [15, 18, 20, 23]. Steady spatially localized states have been observed widely in many investigations of the Swift–Hohenberg equation [15, 18, 20, 23, 69, 93]. In double-diffusive convection, steady spatially localized states have been observed numerically in binary [11, 74] and thermosolutal convection [12].

In convection with two different gradients, a subcritical Hopf bifurcation can occur at the onset of flow leading to states of large-amplitude TW or SW. With bistability between the trivial state and periodic TW or SW, localized travelling wave (LTW) or localized standing wave (LSW) can be found. Unlike the steady localized patterns in the Swift–Hohenberg equation where the time derivative vanishes, the LTW and LSW require the time dependency leading to spatially localized cells whose shapes change with time. LTW observed in investigations of binary convection [6, 8, 48, 83, 101, 120], where they are also called travelling pulses in some other investigations [57–59, 112].

Our interest in this chapter is to find localized states in the model. The analysis of the normal form obtained by [34] shows that there is a subcritical pitchfork bifurcation for all positive and negative cases with $A > 0$. For $A < 0$, the normal form has a subcritical Hopf bifurcation to SW for cases I+, III+, IV+, V+,VI+,VII+, and VIII+, and a subcritical Hopf bifurcation to TW for casesII+, IX+ and I− (see Figure 2.2 and [34]).

In this chapter, we will focus on obtaining two bifurcation scenarios in the normal form equation, in order to obtain spatially localized steady state (LSS) and LTW for the model. These cases are labelled IV− with $A > 0$ and I− with $A < 0$ in [34]. Figure 5.1 shows the stability in (ν, μ)-plane (right panel) and the corresponding bifurcation diagrams (middle and left panel), where the middle panel shows the bifurcation above the diagonal in (ν, μ)-plane and the left panel shows the bifurcation below the diagonal in (ν, μ)-plane (a) for case IV− with $A > 0$ and (b) for case I− with $A < 0$ from [34]. In the next, we will discuss the bifurcation diagrams for these two cases as follows:

- **Case IV− with** $A > 0$: This case lies in the region where the coefficients

D and M are both negative and the fraction $\frac{D}{M} > \frac{1}{2}$. The bifurcation below the diagonal in (ν, μ)-plane (see Figure 5.1 a, right panel) has a subcritical SS branch from a pitchfork bifurcation at $\mu = 0$. Stable SW and unstable TW bifurcate from the trivial state at a Hopf bifurcation where $\nu = 0, \mu < 0$. The stable SW branch terminates on the subcritical SS branch with the formation of a heteroclinic orbit at a global bifurcation SL_s connecting two saddles. The unstable TW branch terminates at the subcritical SS at L_m. The bifurcation above the diagonal in (ν, μ)-plane (see Figure 5.1 a, middle panel) has only a subcritical SS branch from a pitchfork bifurcation at $\mu = 0$. The trivial state is stable in the region where $\mu < 0$ and $\nu < 0$. This case has been investigated analytically and numerically in thermosolutal convection [33, 45, 55, 56] and is important because it was an early example of the discovery and analysis of how a Shil'nikov heteroclinic orbit [55, 89] can lead to chaotic dynamics, though this is in a different parameter regime from that which we will investigate.

- **Case I− with** $A < 0$: This case lies in the region where $D > 0$ and $M < 0$. The bifurcation below the diagonal in (ν, μ)-plane (see Figure 5.1 b, right panel) has an unstable SS branch bifurcating from a pitchfork bifurcation at $\mu = 0$ with $\nu > 0$. It also has a subcritical TW branch and unstable SW branch bifurcating from the trivial state at a Hopf bifurcation where $\nu = 0, \mu < 0$. The SW branch undergoes saddle-node (SN) bifurcation at SN_{s2} and terminates at the SS branch at L_M. The bifurcation above the diagonal in (ν, μ)-plane (see Figure 5.1 b, middle panel) has stable SS branch bifurcating from a pitchfork bifurcation at $\mu = 0$ with $\nu > 0$ which becomes unstable after passing the half lines L_m. The subcritical TW branch bifurcates from the SS branch at L_m. The trivial state is stable in the region where $\mu < 0$ and $\nu < 0$.

We have selected these two cases since we expect that there is subsequent saddle-

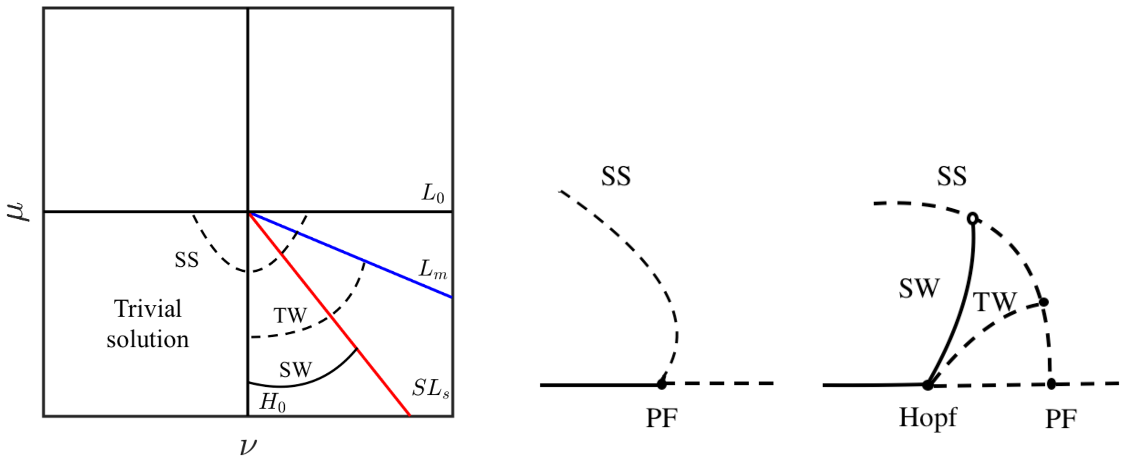

(a) Case IV$-$, $A > 0$

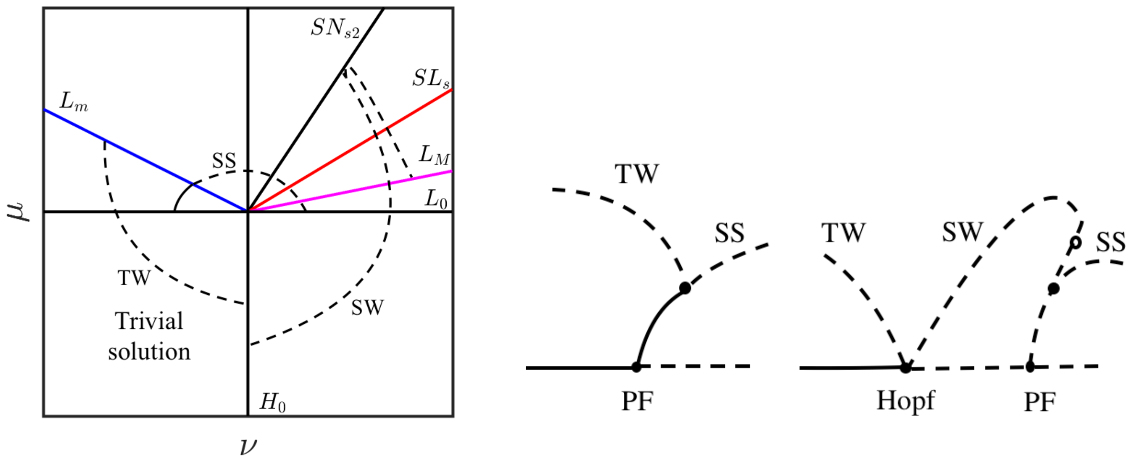

(b) Case I$-$, $A < 0$

Figure 5.1: Sketch of the stability diagram in (ν, μ)-plane in left and the corresponding bifurcation diagram in right from [34], where the middle panel represents the bifurcation above the diagonal in (ν, μ)-plane and the right panel represents the bifurcation below the diagonal in (ν, μ)-plane, (a) for case IV$-$ with $A > 0$ and (b) for case I$-$ with $A < 0$. The notation is explained in Chapter 2.

node bifurcations at the subcritical branch of SS (case IV$-$ with $A > 0$) and TW (case I$-$, $A < 0$) would lead to stable large-amplitude solutions coexisting with the stable trivial solutions, and possibly then to LSS and LTW.

In Chapter 4, we showed that the model (4.29) with the nonlinearities u^2, uu_{xx},

u^3, u^2u_t and u_t^3 with the coefficients Q_1, Q_3, C_1, C_2 and C_4 is Lyapunov stable when C_2 and C_4 are negative. With this choice of nonlinearities, the normal form is restricted to cases II$-$ to IX$-$ with $A < 0$ and case II$-$ and III$-$ with $A > 0$, as described in Chapter 4. The two cases IV$-$ with $A > 0$ and I$-$ with $A < 0$ cannot be obtained with this choice of nonlinearity. This requires us to modify the model again by adding further nonlinearities.

In section 5.2, we show the weakly nonlinear analysis for the new nonlinearities and the coefficients A, M and C for the normal form. We also show examples of the parameters values that result in the two cases of interest. In section 5.3 and 5.4 we find the subcritical bifurcation of pitchfork and Hopf bifurcation, respectively, at suitable parameters values. In each case we investigate the subcritical branch in small domains using the time-stepping method we described in Chapter 4. Moreover, we compare the stability with [34]. In order to obtain localized states we increase the domain size to fit many wavelengths, taking sech envelopes with different widths as initial conditions in the time-stepping. In addition we follow the spatially localized steady state branch using numerical continuation with Newton iteration in order to investigate its homoclinic snaking behaviour.

5.2 New nonlinearities and the weakly nonlinear analysis

In this section we will focus on finding nonlinearities that result in case IV$-$ with $A > 0$ where $D, M < 0$ and the fraction $\frac{D}{M} > \frac{1}{2}$, and case I$-$ with $A < 0$ where $D > 0, M < 0$ and $\frac{D}{M} < 0$. The previous nonlinearities $u^2, uu_{xx}, u^3, u^2u_t$ and u_t^3 with the coefficients Q_1, Q_3, C_1, C_2 and C_4 allow A to be positive (with a limited range $0 < \frac{D}{M} < \frac{1}{2}$) and negative (with a limited range $\frac{D}{M} > 0$), where D and M are always negative. In order to obtain case IV$-$ we want $\frac{D}{M} > \frac{1}{2}$ (with $D < 0$ and

$M < 0$) and in order to obtain case I$-$ we want $\frac{D}{M} < 0$ (with $D > 0$ and $M < 0$). This can achieved be adding cubic terms to the PDE since the coefficients D and M are determined at fourth order in ϵ (see Section 4.2).

In Section 3.3, we mentioned to some cubic terms that we want to consider in this thesis: $(uu_{xx})u_t, (u_x)^2u_t, u^2u_{txx}, uu_tu_{xx}$ and uu_xu_{tx}. Following the weakly nonlinear method mentioned in Section 3.4, we expand u in terms of small ϵ as $u = \epsilon u_1 + \epsilon^2 u_2 + \epsilon^3 u_3 + \epsilon^4 u_4 + \cdots$, and scaling the time $\frac{\partial}{\partial t} \to \epsilon \frac{\partial}{\partial t}$, then the above cubic nonlinearities with $O(\epsilon^4)$ are $(u_1 u_{1xx})u_{1_t}$, $(u_{1_x})^2 u_{1_t}$, $u_1^2 u_{1_{txx}}$, $u_1 u_{1_t} u_{1_{xx}}$ and $u_1 u_{1_x} u_{1_{tx}}$ where u_1 is

$$u_1(x,t) = F_1(t)e^{ix} + \bar{F}_1(t)e^{-ix}. \tag{5.1}$$

Note that, the weakly nonlinear analysis is the same as in Chapter 4 up to third power of ϵ. Since $u_{1_{xx}} = -u_1$, the e^{ix} components of the terms $(u_1 u_{1xx})u_{1_t}$, $u_1^2 u_{1_{txx}}$, $u_1 u_{1_t} u_{1_{xx}}$ are the same as that from the term $-u_1^2 u_{1_t}$ in the model (4.29). Therefore, these terms play the same role in the fraction $\frac{D}{M}$ as $-u_1^2 u_{1_t}$, and do not enlarge the range of values of $\frac{D}{M}$. The e^{ix} component of the terms $(u_{1_x})^2 u_{1_t}$ and $u_1 u_{1_x} u_{1_{tx}}$ are $\left(2F_1\bar{F}_1\frac{\partial F_1}{\partial t} - F_1^2\frac{\partial \bar{F}_1}{\partial t}\right)$ and $\left(F_1^2\frac{\partial \bar{F}_1}{\partial t}\right)$, respectively. By applying the weakly nonlinear as before we get the normal form

$$\frac{\partial^2 z}{\partial t^2} = \mu z + \nu\frac{\partial z}{\partial t} + A|z|^2 z + C(\frac{\partial z}{\partial t}\bar{z} + z\frac{\partial \bar{z}}{\partial t})z + D|z|^2\frac{\partial z}{\partial t}, \tag{5.2}$$

where C, D and $M = 2C + D$ are

$$\begin{aligned} C &= -4bQ_1^2 + 6bQ_1Q_3 - 2bQ_3^2 + C_2 - C_5 + C_6, \\ D &= \frac{-4}{9}bQ_1^2 + \frac{14}{9}bQ_1Q_3 - \frac{10}{9}bQ_3^2 + C_2 + 3C_5 - C_6, \\ M &= \frac{-76}{9}bQ_1^2 + \frac{122}{9}bQ_1Q_3 - \frac{46}{9}bQ_3^2 + 3C_2 + C_5 + C_6, \end{aligned} \tag{5.3}$$

and the coefficients A set at the third power of ϵ and given by

$$A = (Q_1 - Q_3)\left(\frac{38}{9}Q_1 - \frac{23}{9}Q_3\right) + 3C_1, \tag{5.4}$$

(see Section 4.2), and $Q_1, Q_3, C_1, C_2, C_4, C_5$ and C_6 are the coefficients of the nonlinearities u^2, uu_{xx}, u^3, u^2u_t, u_t^3, $(u_x)^2u_t$ and uu_xu_{tx}, respectively.

Therefore, the model we consider in this chapter is

$$\begin{aligned}\frac{\partial^2 u}{\partial t^2} = \left(\mu - \left(1 + \frac{\partial^2}{\partial x^2}\right)^2\right)u + \left(\nu - b\left(1 + \frac{\partial^2}{\partial x^2}\right)^2\right)u_t + Q_1u^2 \\ + Q_3uu_{xx} + C_1u^3 + C_2u^2u_t + C_4u_t^3 + C_5(u_x)^2u_t + C_6uu_xu_{tx},\end{aligned} \tag{5.5}$$

where μ and ν are the control parameters, $Q_1, Q_3, C_1, C_2, C_4, C_5$ and C_6 are constants, and $b > 1$.

Without the new cubic terms the model is Lyapunov stable with $C_2 < 0$ and $C_4 < 0$. The Lyapunov function is bounded below for $C_1 < 0$ as we have mentioned in Chapter 3. With the new terms $(u_x)^2u_t$ and uu_xu_{tx}, the Lyapunov function (if it exists) becomes more complicated. We do not calculate this Lyapunov function, but rather we choose the coefficients C_5 and C_6 that give the wanted case (case IV−, $A > 0$ and case I−, $A < 0$), and rely on C_1, C_2 and C_4 to provide global stability. This is confirmed by numerical integration. In Table 5.1, we show values of the PDE parameters that represent case IV− with $A > 0$ and I− with $A < 0$. Note that, the coefficients mentioned in table are not unique as long as they result in a suitable case. In next section, we solve the PDE numerically and obtain localized states.

Case	Q_1	Q_3	C_1	C_2	C_4	C_5	C_6	A	M	D	$\frac{D}{M}$
IV-	0.9	-0.2	-0.2	-1	-1	-0.5	6	4.14	-16.47	-9.87	0.6
I-	0.8	0.5	-1	-0.1	-1	-0.1	-5	-2.37	-7.92	4.72	-0.6

Table 5.1: Table shows an example of parameters value for the model (5.5) that represent case IV$-$ with $A > 0$ and I$-$ with $A < 0$ in the normal form [34].

5.3 Case IV$-$ with $A > 0$: localized steady states

5.3.1 Checking the stability of steady states

In this section, we obtain the solution behaviour and stability in the case IV$-$ (with $A > 0$) by solving the model (5.5) numerically. In the numerical treatment, we use the same method described in Section 4.4. We show the result in (ν, μ)-plane to compare the stability region with [34] and we plot the amplitude against θ, where θ is the angle in degrees that control the position of ν and μ in the (ν, μ)-plane:

$$\nu = d\cos(\theta) \qquad \mu = d\sin(\theta). \tag{5.6}$$

The normal form shows stable SW occur in the region between the half line $\nu = 0,\ \mu < 0$, (the Hopf bifurcation) and the half line SL_s where

$$SL_s : 5A\nu \approx M\mu,\ \mu < 0.$$

The subcritical SS branch bifurcates from a pitchfork bifurcation at $\mu = 0$ (see Figure 5.1). Note that the Hopf bifurcation occurs at $\nu = 0$ and $\mu < 0$ which correspond to $\theta = 270°$ and the pitchfork bifurcation occurs at $\mu = 0$ which correspond to $\theta = 0°$ and $\theta = 180°$.

We solve the PDE (5.5) using the parameters value in Table 5.1 with 32 gird

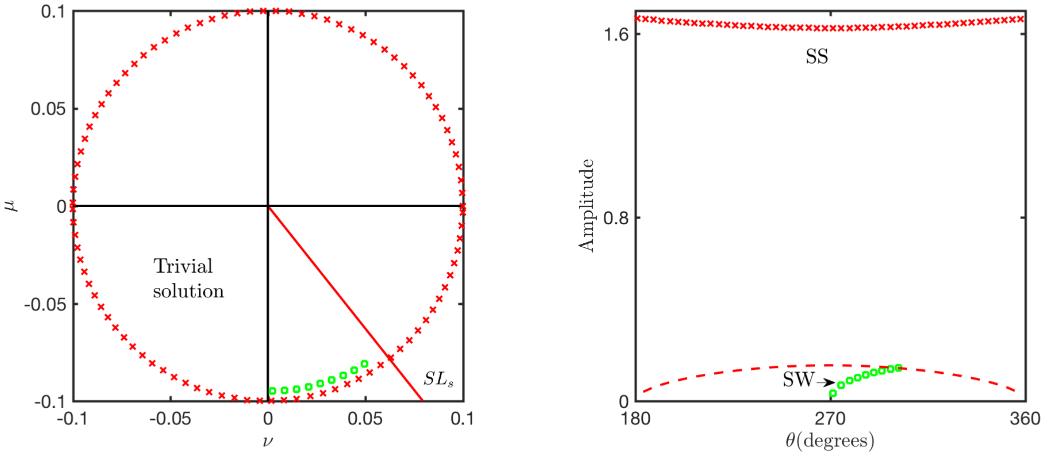

(a) (b)

Figure 5.2: Plot the solution from solving the model (5.5) by time-stepping with parameters values $Q_1 = 0.9, Q_3 = -0.2, C_1 = -0.2, C_2 = C_4 = -1, C_5 = -0.5, C_6 = 6$ and $b = 2$ for radius 0.1 and allowing one wavelength with 32 gird points. (a) Shows the solution in (ν, μ)-plane and (b) shows the amplitude of the mode $k = 1$ as θ is the control parameter where a Hopf bifurcation occurs at $\theta = 270°$ and a pitchfork bifurcation occurs at $\theta = 180°$ and $\theta = 0°$. The red x and green square refer to extended SS and SW solutions, respectively. The red dashed line refers to the small-amplitude unstable SS computed from the weakly nonlinear theory (which is $\sqrt{\frac{-\mu}{A}}$ where $A = 4.14$). The half line SL_s is the line of Hopf bifurcations where SW joins the small-amplitude unstable SS (the red dash line).

points with one wavelength in a one-dimensional domain for three different radii $d = 0.1, 0.7$ and 0.9. To obtain the small and large-amplitude we do time-stepping twice, one with small initial conditions and one with large initial conditions. From time-stepping we plot the results in Figure 5.2 for radius 0.1 and Figure 5.3 for radius 0.7 and 0.9 where (a) shows the solutions in (ν, μ)-plane and (b) shows the amplitude of modes with $k = 1$, this represents F_1 in weakly nonlinear analysis.

Starting from small initial conditions close to a pitchfork bifurcation $\theta = 180°$ where $\nu < 0, \mu = 0$, the trivial state stable when $\mu < 0$ and $\nu < 0$ until reaches to a Hopf bifurcation. The SW branch bifurcates from the trivial state with small-amplitude at a Hopf bifurcation $\theta = 270°$ where $\nu = 0, \mu < 0$ and increases as ν increase until reaches near the line SL_s which has slope $\frac{\mu}{\nu} = -1.26$. The amplitude then increases to large-amplitude SS after passing SL_s. The large-amplitude

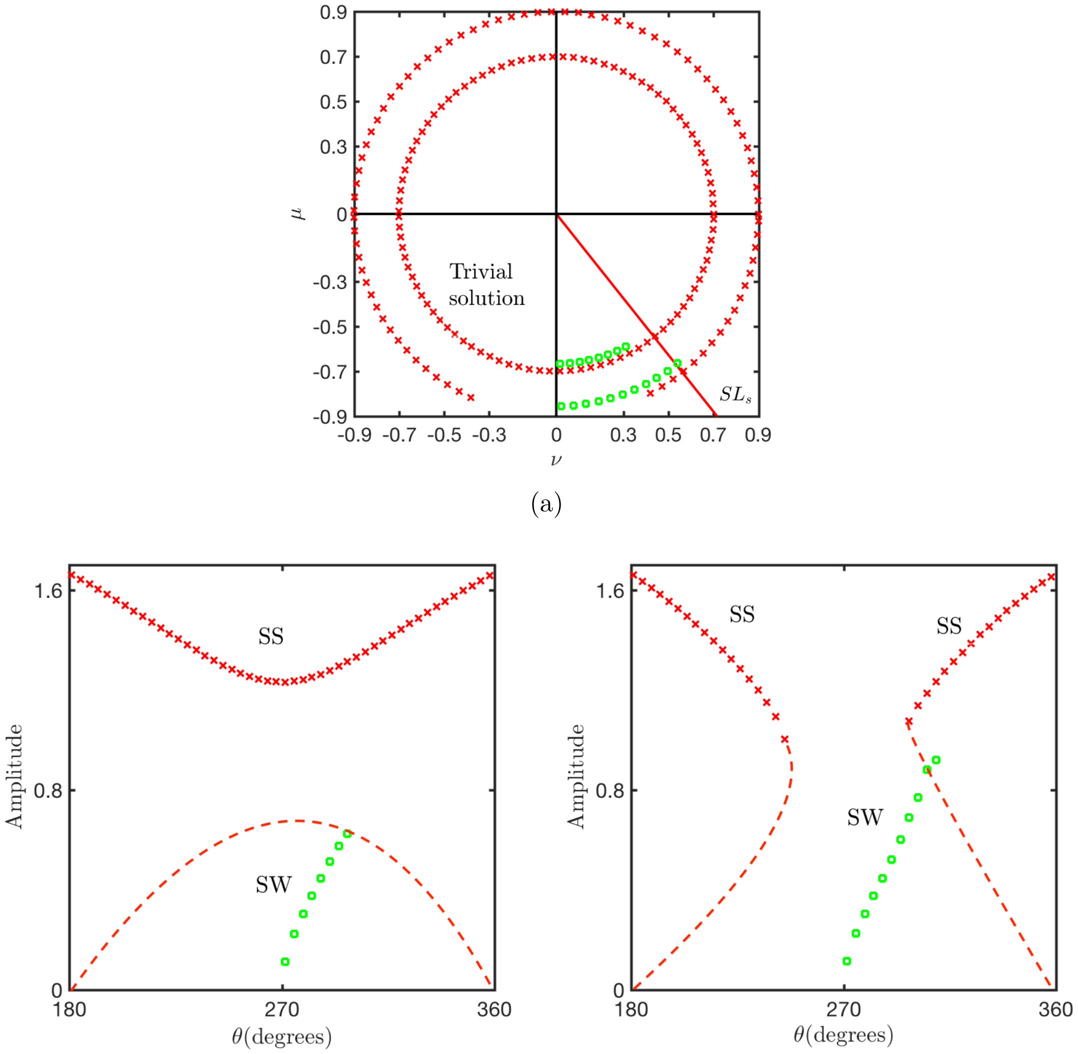

(a)

(b)

(c)

Figure 5.3: Plot the solution from solving the model (5.5) by time-stepping with parameters values $Q_1 = 0.9, Q_3 = -0.2, C_1 = -0.2, C_2 = C_4 = -1, C_5 = -0.5, C_6 = 6$ and $b = 2$ for radii $0.7, 0.9$ and allowing one wavelength with 32 gird points. (a) Shows the solution in (ν, μ)-plane and (b,c) shows the amplitude of the mode $k = 1$ as θ is the control parameter (b) for radius 0.7 and (c) for radius 0.9. A Hopf bifurcation occurs at $\theta = 270°$ and a pitchfork bifurcation occurs at $\theta = 180°$ and $\theta = 0°$. The red x and green square refer to extended SS and SW solutions, respectively. The red dash line refers to (b) the small-amplitude unstable SS computed from the weakly nonlinear theory (which is $\sqrt{\frac{-\mu}{A}}$ where $A = 4.14$) and (c) an illustration of unstable SS, drawn by hand. The half line SL_s is the line of Hopf bifurcations where SW joins the small-amplitude unstable SS (the red dash line).

SS branch bifurcates from a pitchfork bifurcation $\theta = 180°$ and disconnects to the small-amplitude SS in the absence of the saddle-node bifurcation for radius 0.1 and 0.7 (see Figures 5.2 a,b and 5.3 a,b). For radius 0.9, the branch of SS close to $\theta = 180°$ has large-amplitude and connects to the small-amplitude SS branch in a saddle-node bifurcation, apparent in Figure 5.3 (c).

This case shows a bistability between two different pairs of states. Bistability between the trivial state and large-amplitude SS occurs in the region where $\mu < 0$ and $\nu < 0$. Bistability between small-amplitude SW and large-amplitude SS is in the region from $\nu = 0$ to the half line SL_s. This indicate that a LSS can obtained with two different backgrounds: trivial states and SW, as we see in the next section.

5.3.2 Localized states

In the last section, we have seen that the PDE has large-amplitude SS solutions. There is bistability between the trivial state and large-amplitude SS when $\mu < 0$, $\nu < 0$ and bistability between small-amplitude SW and large-amplitude SS in the region between $\nu = 0$, $\mu < 0$ and the half line SL_s. In this section, we get localized states in these regions. To do this we follow the following process. First, we increase the domain size to allow 64 wavelengths with 16 grid points per wavelength ($L_x = 64\lambda_c$, $\lambda_c = 2\pi$) and do time-stepping to find an extended SS (such as in Figure 5.4 a). Then, we use a sech envelope with different widths to make several initial conditions and do time-stepping again to obtain localized states (such as in Figure 5.4 b). Using this method we are able to get localized steady states with two different backgrounds.

First, we find LSS with the trivial state as a background in the region where the trivial state and large-amplitude SS are both stable ($\mu < 0$ and $\nu < 0$).

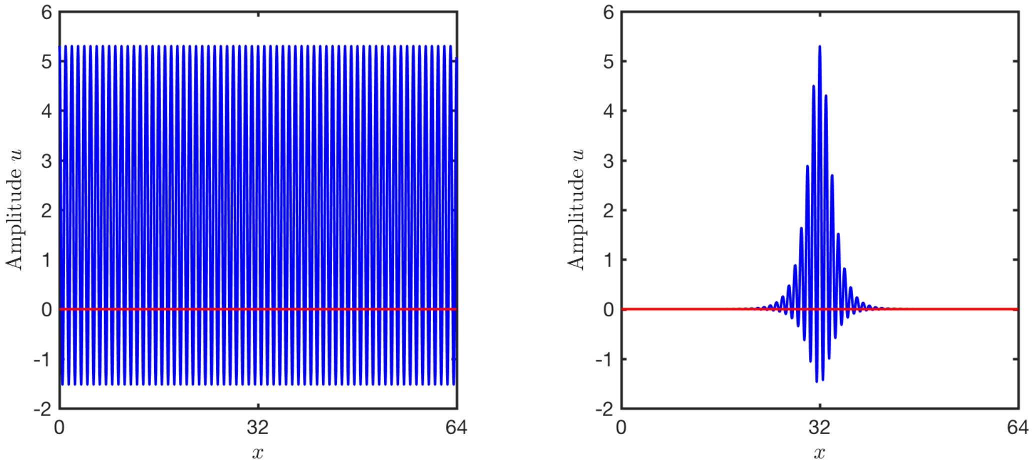

(a) **(b)**

Figure 5.4: (a) Example of extended SS solutions from time-stepping for radius 0.7 and $\theta = 185°$ with parameters values $Q_1 = 0.9, Q_3 = -0.2, C_1 = -0.2, C_2 = C_4 = -1, C_5 = -0.5, C_6 = 6$ and $b = 2$ (where domain size $L_x = 64\lambda_c$, $\lambda_c = 2\pi$). (b) Example of initial condition to obtain localized states using sech envelope for (a). The blue and red curve refer to u and u_t, respectively.

Figure 5.5 (a) shows one example of LSS with trivial state background for radius 0.7 and $\theta = 200°$ ($\nu = -0.54$, $\mu = -0.45$). There are other LSS with different widths, depending on the initial conditions, and to investigate these in detail we do numerical continuation in the next section.

Second, we find LSS with an MW background in the region where the large-amplitude SS and the small-amplitude SW are both stable. The bistability occurs in the region between the Hopf bifurcation at $\theta = 270°$ ($\nu = 0, \mu < 0$) to the half line SL_s at $\theta \approx 308.4$, as mentioned in Section 5.3.1. The small-amplitude MW background solutions move as a function of time. Initially, the small-amplitude solutions are SW with large-amplitude SS in the middle of the domain. As time increases the SW turn in to MW. This change occurs because the left-right symmetry of the SW solutions is broken by the SS solutions in the middle [51]. Figure 5.5 (b) shows one example of LSS with MW background for radius 0.7 and $\theta = 280°$ ($\nu = 0.12, \mu = -0.69$). Many widths of this class of solutions can be obtained by changing the initial sech envelope width.

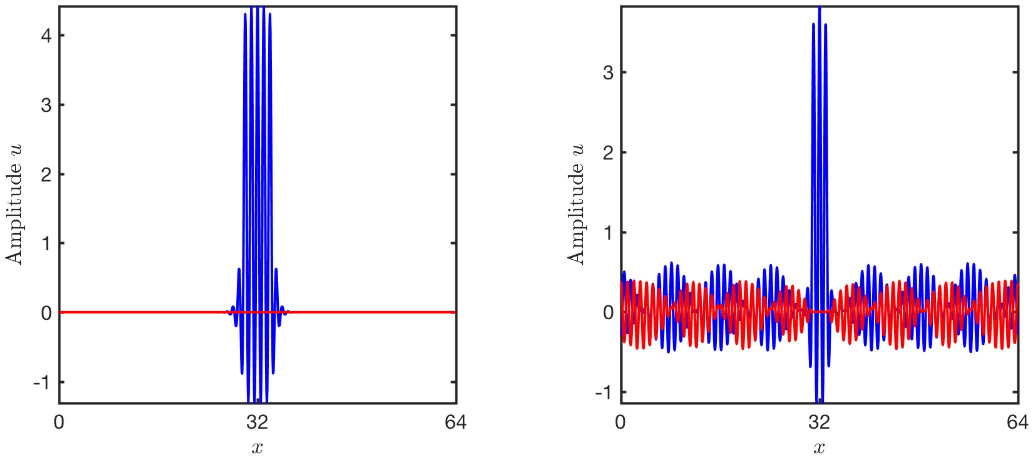

(a) **(b)**

Figure 5.5: (a) Localized steady state with trivial solutions in the background from time-stepping at radius 0.7 and $\theta = 220°$ where $\nu = -0.54, \mu = -0.45$ with parameters values $Q_1 = 0.9, Q_3 = -0.2, C_1 = -0.2, C_2 = C_4 = -1, C_5 = -0.5, C_6 = 6$ and $b = 2$. (b) Localized steady state with MW solutions in the background from time-stepping at radius 0.7 and $\theta = 280°$ where $\nu = 0.12, \mu = -0.69$. The domain size ($L_x = 64\lambda_c$, $\lambda_c = 2\pi$). The blue and red curve refer to u and u_t, respectively for all mode of k.

Unlike the LSS with the trivial state background, in this case two patterns (large-amplitude SS and small-amplitude MW) coexist, which suggests the presence of a spatial heteroclinic orbit between the SS and MW states. We discuss this further in Chapter 6.

5.3.3 Numerical continuation

In the following we use numerical continuation to compute the numerical solutions of the model for both the extended SS and the LSS. The method we use based on Newton iteration and pseudo arclength continuation (see Appendix B). Using continuation, we are finding only steady solutions. Setting the time-derivative term to zero, the model (5.5) is the steady Swift–Hohenberg equation:

$$0 = \left(\mu - \left(1 + \frac{\partial^2}{\partial x^2}\right)^2\right) u + Q_1 u^2 + Q_3 u u_{xx} + C_1 u^3. \tag{5.7}$$

The solutions then depend on μ only but stability depends on both μ and ν. The initial guesses for the branches of extended SS and LSS are obtained from time-stepping. Since θ controls the values of μ and ν in the (ν, μ)-plane, we will use θ as the bifurcation parameter with fixed radius. We show the bifurcation diagram of all solutions as functions of θ and μ, where $\mu = d\sin(\theta)$, against the norm as a measure of the solutions, where

$$||u||_2 = \left(\int_0^{L_x} (u(x))^2 dx \right)^{\frac{1}{2}}. \tag{5.8}$$

We will do continuation in two different radii 0.7 and 0.9 in one-dimensional domain allowing 16 wavelengths with 16 grid points per wavelength ($L_x = 16\lambda_c$, $\lambda_c = 2\pi$).

5.3.3.1 Continuation for radius 0.9

Starting from initial guesses obtained from time-stepping in numerical continuation with radius $d = 0.9$, we do continuation to obtain the extended SS and the LSS solutions. Figure 5.6 (a) shows the solutions from numerical continuation with θ as the control parameter, and (b) for μ where $\mu = d\sin(\theta)$. In Figure 5.6, we represent the full branch of extended SS in black, the LSS branch with even numbers of peaks L_e in orange and the LSS branch with odd numbers of peaks L_o in green. Along the odd branch L_o the midpoint $\left(\frac{L_x}{2}\right)$ of the localized state is always a global maximum (with an odd number of maxima), while along the even branch L_e the midpoint $\left(\frac{L_x}{2}\right)$ is a global minimum (with an even number of maxima). Figure 5.7 shows Figure 5.6 (b) in more detail with examples of LSS with different widths.

The extended SS branch emerges subcritically from the trivial state at $\theta = 180°$ (the pitchfork bifurcation $\mu = 0$) and undergoes a saddle-node bifurcation at

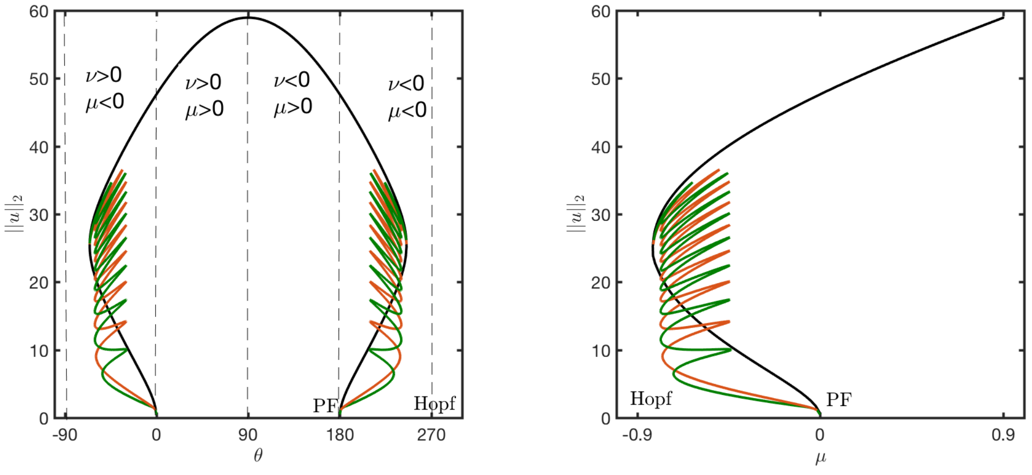

(a) **(b)**

Figure 5.6: (a) The full branch for extended SS in black and the odd and even branch in green and brown where θ is the control parameter and radius 0.9 with parameters values $Q_1 = 0.9, Q_3 = -0.2, C_1 = -0.2, C_2 = C_4 = -1, C_5 = -0.5, C_6 = 6$ and $b = 2$. (b) Plot the bifurcation with μ is the control parameter from (a) where $\mu = d\sin(\theta)$. The two snaking regions in (a) overlap in (b) but in (a), the background trivial solution is stable for $180° \le \theta \le 270°$ ($\nu < 0$) while it is unstable for $-90° \le \theta \le 0°$ ($\nu > 0$).

$\theta = 245.6°$ ($\mu = -0.81$). The branch changes at the saddle-node to a large-amplitude stable state. It reaches the maximum amplitude when $\theta = 90°$ ($\mu = 0.9$) and decreases until reaches to the second saddle-node at $\theta = -65.6°$ ($\mu = -0.81$). The branch then decrease further until terminates back to a pitchfork bifurcation $\theta = 0°$ ($\mu = 0$). Because the solutions depend on μ only there is a symmetry $\theta \to 180° - \theta$. Similarly, we use time-stepping to obtain the initial guess for the even L_e and odd L_o branches for localized state and then do the continuation. Both branches emerge subcritically close to the pitchfork bifurcation with small-amplitude and undergo a series of saddle-node bifurcations producing the homoclinic snaking. Each branch adds an oscillation on each side as it snakes back and forth, until they reach the width of the domain where they terminate on the SS branch, close to the saddle-node point. The snaking region occurs between $\theta = 209.5°$ ($\mu = -0.44$) and $\theta = 240.5°$ ($\mu = -0.78$). The Hopf bifurcation occurs when $\theta = 270°$ (where $\nu = 0$ and $\mu = -0.9$). Note that, for this choice of radius the homoclinic region occurs away from the Hopf bifurcation. The trivial solutions are stable in the region where $\mu < 0$ and $\nu < 0$ and unstable anywhere else.

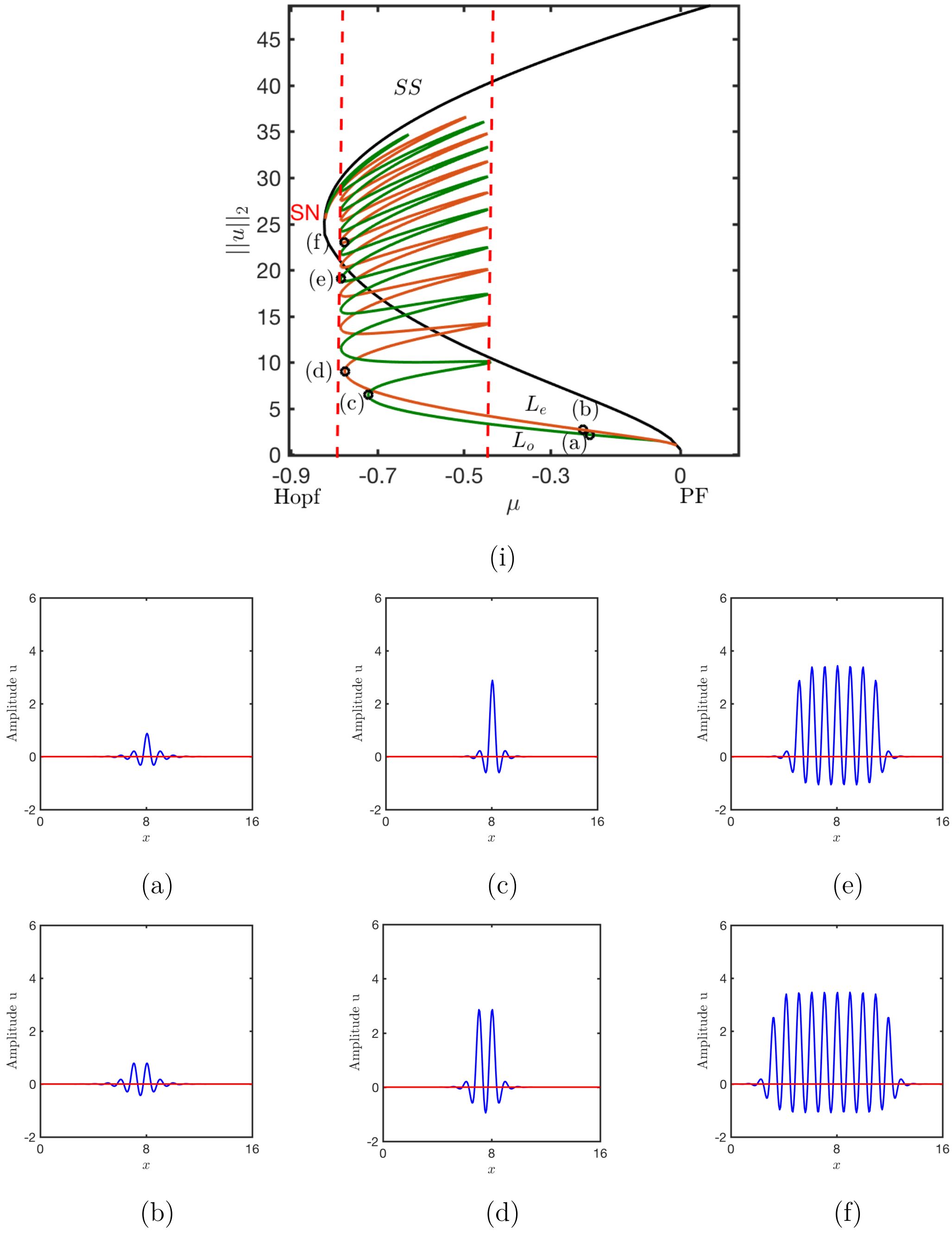

(i)

(a) (c) (e)

(b) (d) (f)

Figure 5.7: (i) The full branch for extended SS in black and the odd L_o and even L_e branches in green and brown where μ is the control parameter and radius 0.9 with parameters values $Q_1 = 0.9, Q_3 = -0.2, C_1 = -0.2, C_2 = C_4 = -1, C_5 = -0.5, C_6 = 6$ and $b = 2$. The SS branch bifurcate from trivial state at a pitchfork bifurcation $\mu = 0$. The saddle-node point (SN) is $\mu = -0.81$. The Hopf bifurcation occurs at $\mu = -0.9$ where $\nu = 0$. (a, c, e) Show the solutions obtained from the odd branch L_o with different widths and (b, d, f) show the solutions obtained from the even branch L_e where the domain size ($L_x = 16\lambda_c,\ \lambda_c = 2\pi$). The snaking region is the region between the red dashed lines.

5.3.3.2 Continuation for radius 0.7

In this section, we examine the numerical continuation for a smaller radius 0.7. The difference is that $-0.7 \leq \mu$, so the saddle-node bifurcation of the SS branch at $\mu = -0.81$ and the left side of the snaking branch cannot be reached.

To obtain the numerical branch for LSS as well as the extended SS branch we use the same process as for radius 0.9. We show the results in Figure 5.8, (a) for θ against the norm and (b) for μ, where $\mu = d \sin(\theta)$.

Starting from large extended SS as initial guesses in continuation, we find that the branch of extended SS has large-amplitude with maximum at $\theta = 90°$ ($\mu = 0.7$) and minimum amplitude at $\theta = 270°$ ($\mu = -0.7$). This branch continues around the circle from $\theta = 0°$ to $\theta = 360°$ and does not connect to the pitchfork bifurcation, which indicates that there is no saddle-node bifurcation.

To find the localized branch we start continuation from initial guesses with various numbers of peaks obtained from time-stepping. The continuation shows that the odd and even branches with at least 15 peaks are isola. They start from the region where the trivial state stable ($\mu < 0$ and $\nu < 0$) and continue to the region where the trivial state not stable after passing the Hopf bifurcation ($\nu = 0$ and $\mu < 0$). Each isolated branch reach the minimum amplitude at $\theta = 270°$ ($\mu = -0.7$). The snaking region of isolated branch occurs between $\theta = 219.5°$ ($\mu = -0.44$) and $\theta = 320.5°$ ($\mu = -0.44$). The two lower branches with one and two peaks bifurcate close the pitchfork bifurcation $\theta = 180°$ ($\mu = 0$) with small-amplitude, reach maximum at $\theta = 270°$ ($\mu = -0.7$), and then terminate with small-amplitude close to the pitchfork bifurcation $\theta = 360°$ ($\mu = 0$).

From time-stepping, the LSS with the trivial state background are stable in the region where $\mu < 0$ and $\nu < 0$ and become unstable after passing the Hopf bifurcation in the region where $\mu < 0$ and $\nu > 0$. After the Hopf bifurcation, the only stable solutions are the LSS with an MW background where there is bistability between SS and SW as we discussed in 5.3.1.

Figure 5.9 summarize the results obtained from numerical continuation for radius 0.7 and 0.9 in (ν, μ)-plane. The black curve refers to the extended SS and the blue curve refers to the region where LSS with the trivial state background exist for both radii. The region between the red dashed lines indicates to the snaking region for radius 0.9 and the isolas for radius 0.7. As we take smaller radius the snaking region becomes narrower. This also indicates that for any radius smaller than -0.44 there is no LSS occur since the bistability between two stable states occurs out of the snaking region. In Figure 5.9 we also show points where the LSS with an MW background (see Figure 5.5 b) occur as green stars, obtained from time-stepping. The SL_s half line is the line where the branch ends on a heteroclinic bifurcation (see Figure 5.1). Beyond this line, there are no SW, and time-stepping leads to large-amplitude SS.

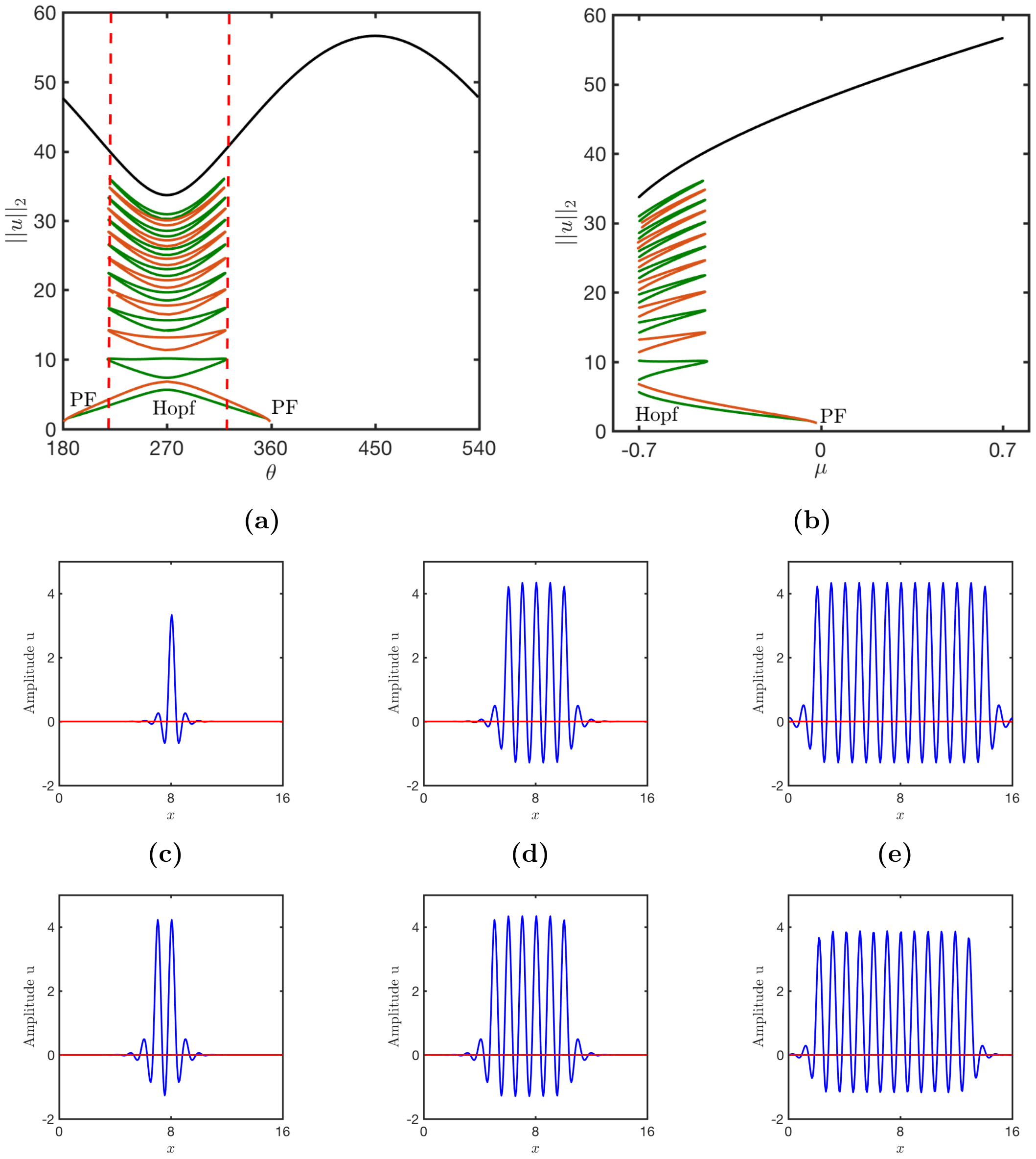

(a) (b)

(c) (d) (e)

(f) (g) (h)

Figure 5.8: The full branch for extended SS in black and the odd and even branches in green and brown for radius 0.7 with parameters values $Q_1 = 0.9, Q_3 = -0.2, C_1 = -0.2, C_2 = C_4 = -1, C_5 = -0.5, C_6 = 6$ and $b = 2$. (a) Shows the solutions where θ is a control parameter and (b) show the solutions in μ where $\mu = d\sin(\theta)$. The pitchfork bifurcation occurs at $\theta = 180°$ and $360°$ where $\mu = 0$. The Hopf bifurcation occurs at $\theta = 270°$ where $\nu = 0, \mu = -0.7$. (a, d, e) Shows the solutions profile for odd solutions with 1,5 and 13 peaks. (f, g, h) Shows the solutions profile for even solutions with 2,6 and 12 peaks. The domain size ($L_x = 16\lambda_c,\ \lambda_c = 2\pi$). The isola region is the region between the red dashed lines.

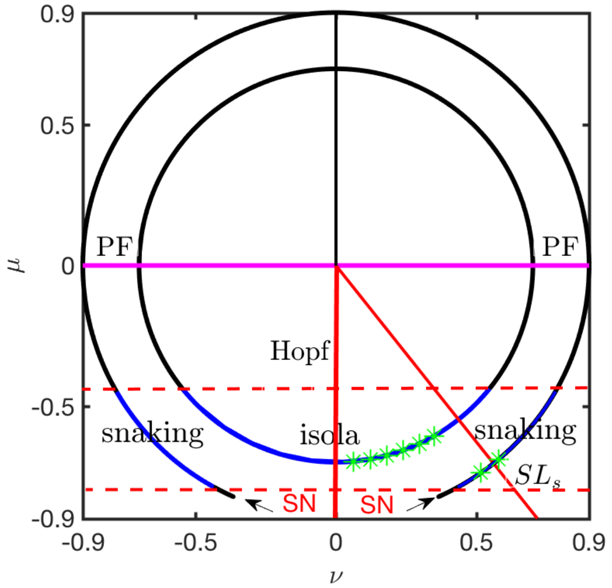

Figure 5.9: (ν, μ)-plane from solving the PDE using numerical continuation for radii 0.9 and 0.7 with parameters values $Q_1 = 0.9, Q_3 = -0.2, C_1 = -0.2, C_2 = C_4 = -1, C_5 = -0.5, C_6 = 6$ and $b = 2$. The pink and red cures refer to the pitchfork bifurcation and Hopf bifurcation, respectively. The black curve refers to the extended SS solutions and the blue curve refers to the snaking region for radius 0.9 (see Figure 5.7) and the isola region for radius 0.7 (see Figure 5.8). The snaking region for radius 0.9 occurs between $\mu = -0.44, \nu = -0.78$ and $\mu = -0.78, \nu = -0.44$. The isolated region occurs between $\mu = -0.44, \nu = -0.54$ to $\mu = -0.44, \nu = 0.54$. The SN point occurs at $\mu = -0.81$ for radius 0.9. The localized solutions stable in the region where the trivial states stable ($\mu < 0$, and $\nu < 0$) and unstable in the region where the trivial states become unstable ($\mu < 0$, and $\nu > 0$). The green star markets refer to the LSS with an MW background from time-stepping (see Figure 5.5 b). The LS_s half line is the line where the bifurcation changes from SW to SS in the normal form (see Figure 5.1).

5.4 Case I$-$ with $A < 0$: localized travelling waves

5.4.1 Checking the stability of travelling waves

In case I$-$ with $A < 0$, the normal form shows a stable SS occurring in the region between the pitchfork bifurcation at $\mu = 0$ where $\nu < 0$ to the half line L_m, where

$$L_m : \mu D = \nu A \qquad A\mu < 0. \tag{5.9}$$

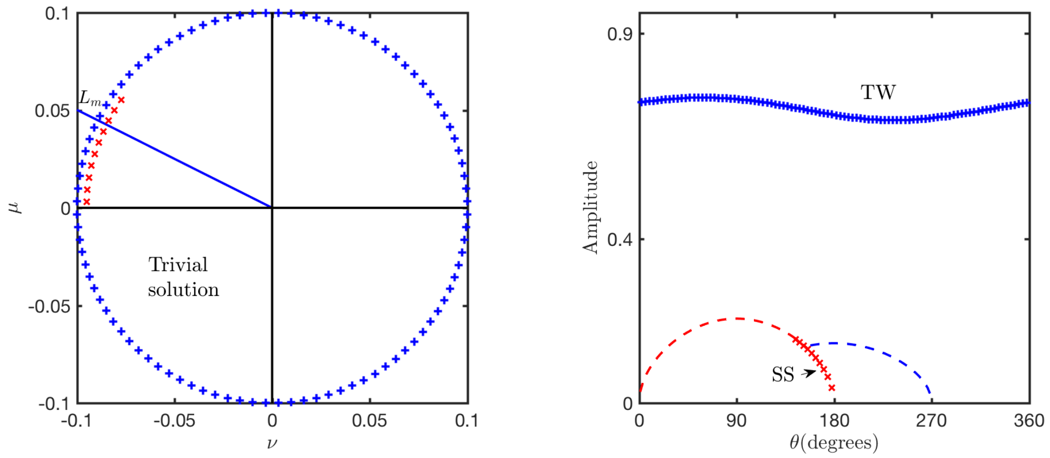

(a) (b)

Figure 5.10: Plot the solution from solving the model (5.5) by time-stepping with parameters values $Q_1 = 0.8, Q_3 = 0.5, C_1 = -1, C_2 = -0.1, C_4 = -1, C_5 = -0.1, C_6 = -5$ and $b = 2$ for radius 0.1 and allowing one wavelength with 32 gird points. (a) Shows the solution in (ν, μ)-plane and (b) shows the amplitude of the mode $k = 1$, θ the control parameter. A Hopf bifurcation occurs at $\theta = 270°$ and a pitchfork bifurcation occurs at $\theta = 180°$ and $\theta = 0°$. The blue + and red x refer to extended TW and SS solutions, respectively. The red and blue dashed lines refer to the small-amplitude unstable SS and TW, respectively, computed from the weakly nonlinear theory (which is $\sqrt{\frac{-\mu}{A}}$ where $A = -2.37$ for SS and $\sqrt{\frac{-\nu}{D}}$ where $D = 4.72$ for TW). The half line L_m is the line from the normal form at which the bifurcation from TW to SS occurs, with slope -0.502 at $\theta = 153.34$.

The TW branch bifurcates subcritically from trivial solution at Hopf bifurcation $\nu = 0$ where $\mu < 0$ (see Figure 5.1 b). Using the parameter values in Table 5.1, we solve the model in small domain (one wavelength with 32 grid points) to obtain the solutions using small and large-amplitude initial conditions, with parameter radii 0.1, 0.7 and 0.9. From time-stepping we plot the results in Figure 5.10 for radius 0.1 and Figure 5.11 for radius 0.7 and 0.9, where (a) shows the solutions in (ν, μ)-plane and (b) shows the bifurcation of the amplitude of mode with $k = 1$.

The trivial state is stable for the region $\nu < 0$ and $\mu < 0$ for all radii 0.1, 0.7 and 0.9. The small-amplitude SS bifurcates at a pitchfork bifurcation $\theta = 180°$ where $\mu = 0, \nu < 0$ and loses stability at L_m, which has the slope $\frac{\mu}{\nu} \approx -0.502$. There is a large-amplitude TW solution around the whole circle in the (ν, μ)-

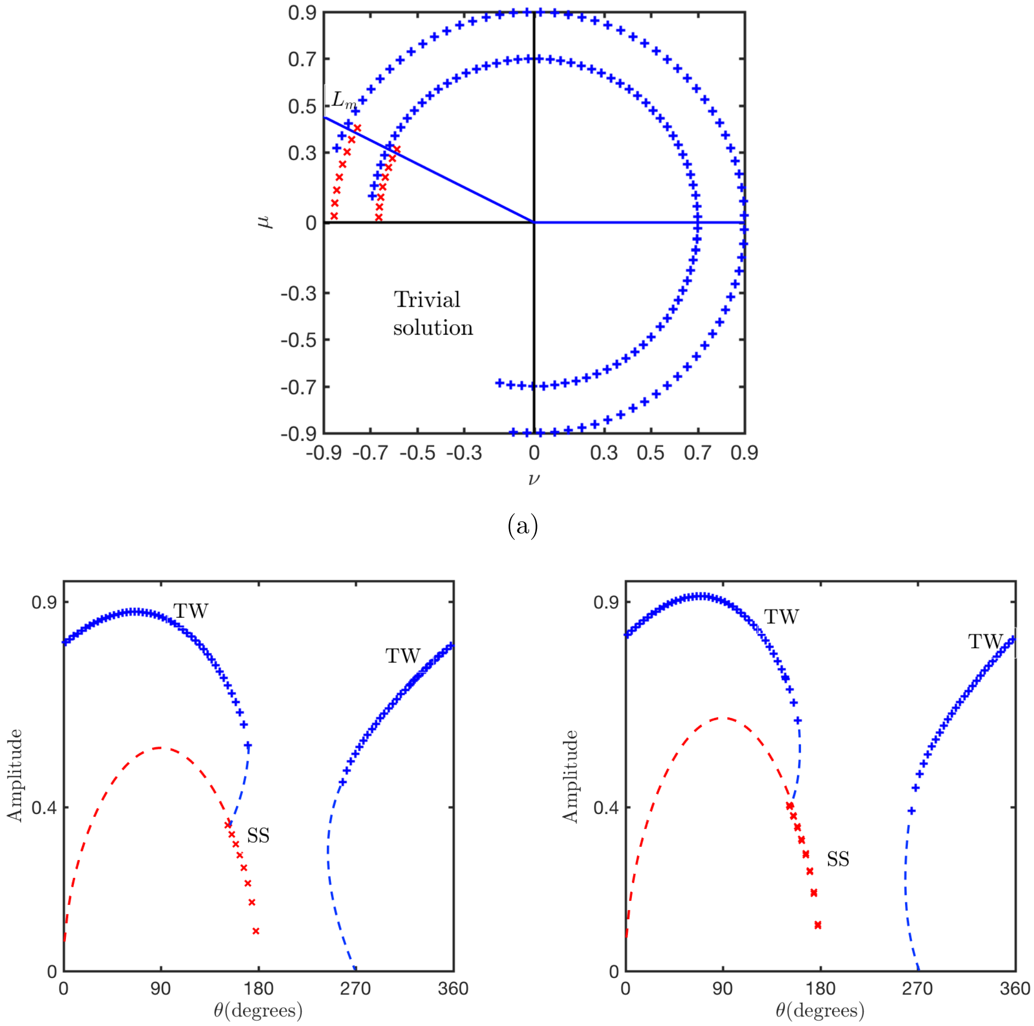

(a)

(b)

(c)

Figure 5.11: Plot the solution from solving the model (5.5) by time-stepping with parameters values $Q_1 = 0.8, Q_3 = 0.5, C_1 = -1, C_2 = -0.1, C_4 = -1, C_5 = -0.1, C_6 = -1$ and $b = 2$ for radii $0.7, 0.9$ and allowing one wavelength with 32 gird points. (a) Shows the solution in (ν, μ)-plane and (b,c) shows the amplitude of the mode $k = 1$, θ the control parameter. A Hopf bifurcation occurs at $\theta = 270°$ and a pitchfork bifurcation occurs at $\theta = 180°$ and $\theta = 0°$. The blue + and red x refer to extended TW and SS solutions, respectively. The red dashed lines refers to the small-amplitude unstable SS. The unstable SS are computed from the weakly nonlinear theory (which is $\sqrt{\frac{-\mu}{A}}$ where $A = -2.37$). The blue dashed line is an illustration of unstable TW, drawn by hand. The half line L_m is the line from the normal form at which the bifurcation from TW to SS occurs, with slope -0.502 at $\theta = 153.34$.

plane at radius 0.1 (see Figure 5.10). For radius 0.7 and 0.9 (see Figure 5.11), the amplitude of the TW decreases in the region where the trivial state or the small-amplitude SS are stable. This indicates that in this case there is bistability between two different states: a large-amplitude TW with trivial states in the region where $\mu < 0, \nu < 0$ and a large-amplitude TW with small-amplitude SS in the region between the pitchfork bifurcation $\mu = 0, \nu < 0$ to the half line L_m. Therefore, the LTW with the trivial state and LTW with SS background can be sought and obtained, as we see in the next section.

5.4.2 Localized states

The bifurcation diagram in the last section shows that there is a bistability between two pairs of stable states: the trivial state and large-amplitude TW in the region where $\mu < 0$ and $\nu < 0$, and the small-amplitude SS and large-amplitude TW in the region between the pitchfork bifurcation at $\mu = 0$ where $\nu < 0$ to the half line L_m. To obtain the localized state we increase the domain size to allow 64 wavelengths in the domain ($L_x = 64\lambda_c, \lambda_c = 2\pi$) and do time-stepping to find an extended TW as an initial condition in obtaining the localized state. Then, we use sech envelop with different widths on the initial conditions and do time-stepping again to obtain the localised state. Using this method we are able to get LTW with two different backgrounds.

First, we find LTW with the trivial state background in the region where $\mu < 0$ and $\nu < 0$. Figure 5.12, shows two examples of LTW with the trivial state backgrounds for two different parameters values (a) for radius 0.1 and $\theta = 200$ where $\mu = -0.034, \nu = -0.094$ and (b) for radius 0.1 and $\theta = 250$ where $\mu = -0.094, \nu = -0.034$. In this examples, the amplitude of u and u_t move from left to right with a group velocity smaller than the phase velocity. At given parameter values, the LTW we find all have the same width, regardless of initial conditions (unlike LSS).

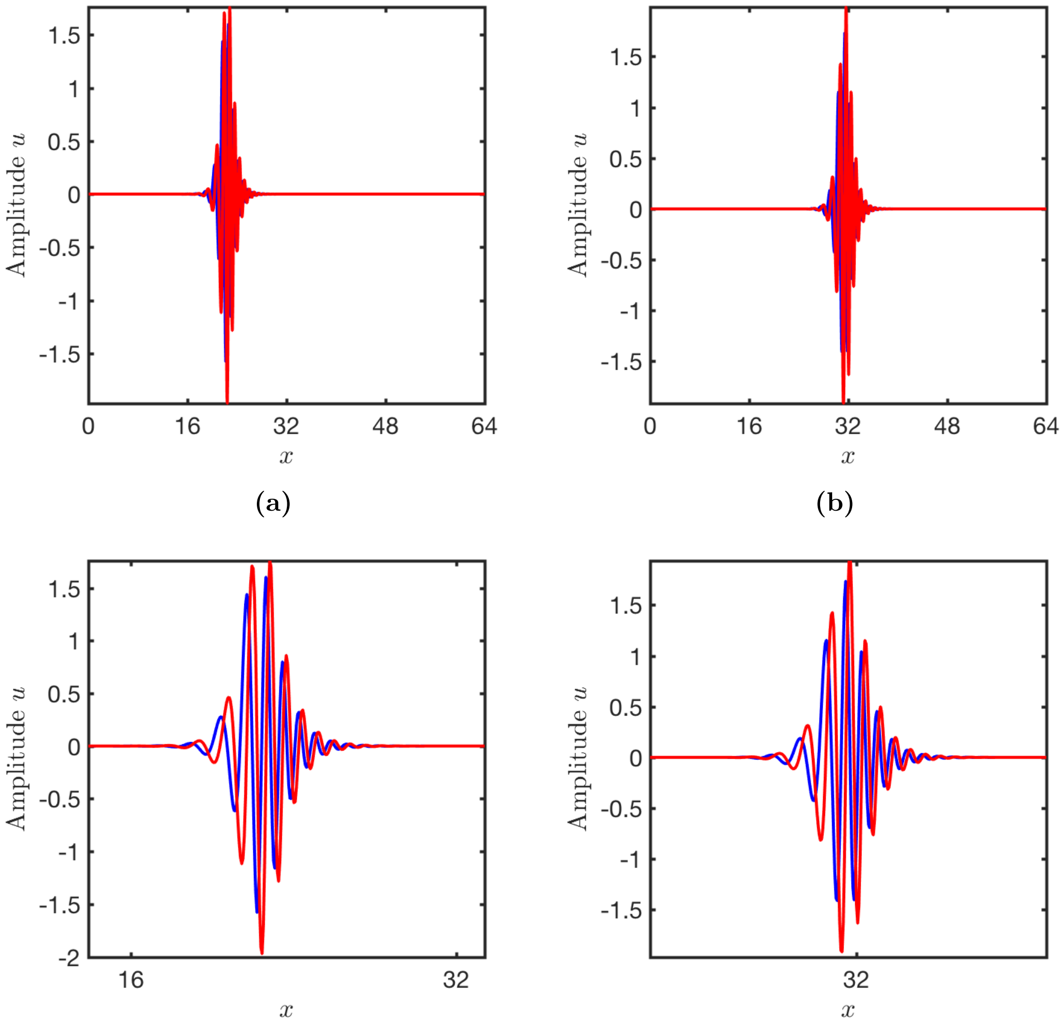

(a)

(b)

(c)

(d)

Figure 5.12: Two examples of LTW with trivial state background for parameters values $Q_1 = 0.8, Q_3 = 0.5, C_1 = -1, C_2 = -0.1, C_4 = -1, C_5 = -0.1, C_6 = -5$ and $b = 2$. (a) For radius 0.1 and $\theta = 200°$ and (b) radius 0.1 and $\theta = 250°$. (c,d) Show zooms of (a,b). The blue and red curves refer to u and u_t. The domain size is $L_x = 64\lambda_c, \lambda_c = 2\pi$.

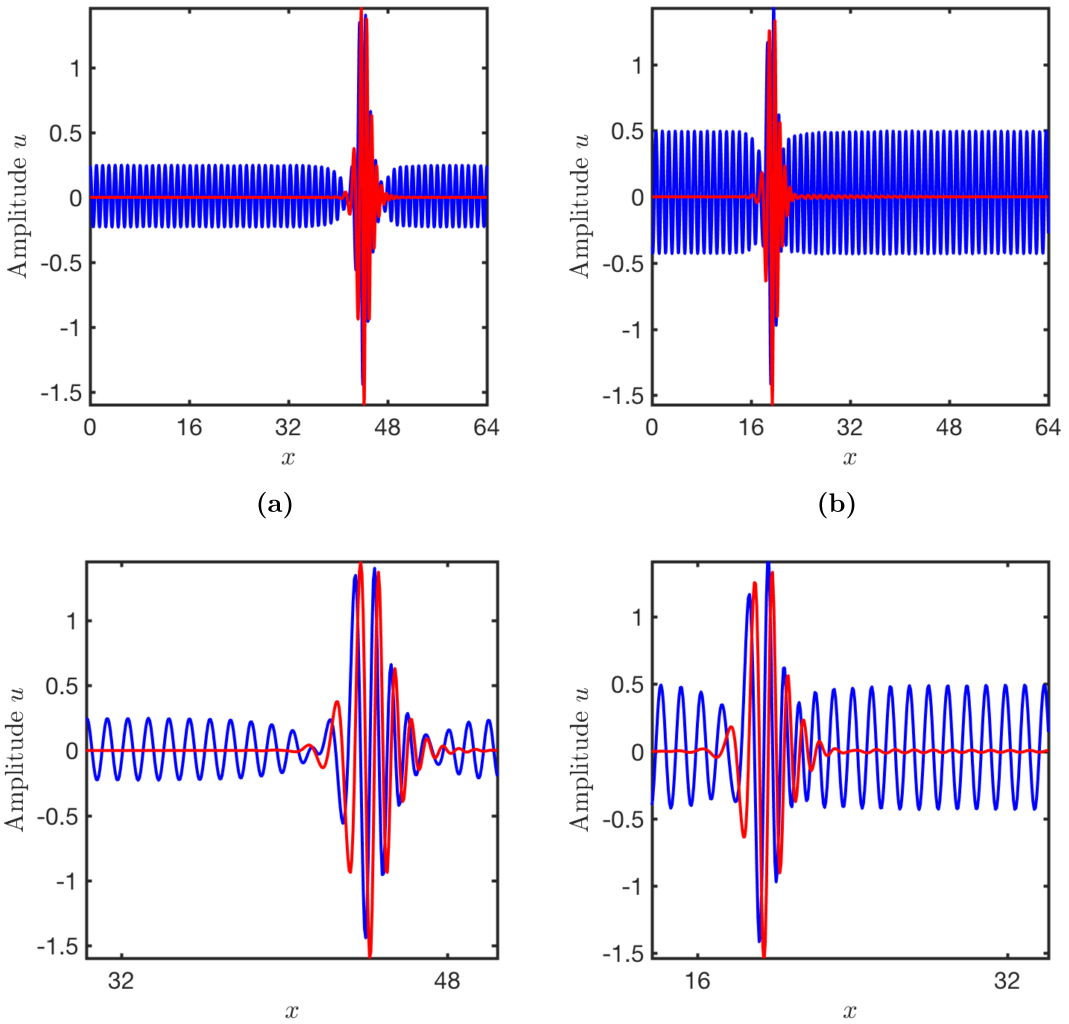

(a) **(b)**

(c) **(d)**

Figure 5.13: Example of LTW with SS background for parameters values $Q_1 = 0.8, Q_3 = 0.5, C_1 = -1, C_2 = -0.1, C_4 = -1, C_5 = -0.1, C_6 = -5$ and $b = 2$ (a) for radius 0.1 and $\theta = 170°$ (b) for radius 0.4 and $\theta = 160°$ where (c,d) are zooms of (a,b). The blue and red curves refer to u and u_t. The domain size is $L_x = 64\lambda_c, \lambda_c = 2\pi$.

Second, we find LTW with an SS background in the region between the pitchfork bifurcation at $\mu = 0$ where $\nu < 0$ to the half line L_m. Figure 5.13, shows two examples of LTW with an SS background for (a) radius 0.1 and $\theta = 170°$ where $\mu = 0.017, \nu = -0.098$ (b) for radius 0.4 and $\theta = 160°$ where $\mu = 0.14, \nu = -0.038$. The LTW move from left to right.

5.5 Conclusion and Discussion

In this chapter, we obtained spatially localized structures in the model PDE (5.5). The localized solutions require coexistence between two stable states. Our expectation that we will able to find the localized states is based on the TB normal form [34]. The normal form shows different bifurcation scenarios based on its coefficients. In this chapter, we focused in two bifurcations scenarios labelled IV$-$ with $A > 0$ and I$-$ with $A < 0$ in [34]. We solved the model with suitable parameter values numerically and obtained the solution behaviour for each case separately.

In the case IV$-$ with $A > 0$, the normal form shows a SS branch that bifurcates subcritically from a pitchfork bifurcation and a branch of SW bifurcates from a Hopf bifurcation and terminates on the subcritical SS branch. Therefore, the bistability in this case occurs with two different pairs of states: a trivial state with large-amplitude SS and a small-amplitude SW with large-amplitude SS. By solving the model using the time-stepping (ETD) method, we found the small-amplitude trivial state in the region where $\nu < 0, \mu < 0$ and small-amplitude SW in the region where $\nu = 0, \mu < 0$ to SL_s. The large-amplitude SS coexist with trivial state and SW. The stability region from solving the model agrees with the stability region obtained in [34] (see Figures 5.2 and 5.3). Using a sech envelope to create initial conditions with different widths, we are able to find localized states with various widths in two different backgrounds: LSS with the trivial state background and LSS with an MW background in the region where the SW exist.

In order to obtain the LSS branch with the trivial solution background we used numerical continuation for the model (5.5) for different parameter radii 0.7 and 0.9. For radius 0.9, we found that there are two branches of localized states with even and odd peaks bifurcating close to the primary pitchfork bifurcation and producing a homoclinic snaking in the region where the trivial state is stable. Each branch adds a pair of oscillations on both sides at saddle-node bifurcations until the solutions reaches the width of the extended state, where they terminate at a saddle-node point. For radius 0.7, we found that the large-amplitude SS solutions does not connect to the pitchfork bifurcation, and the left side of the snaking branch cannot be reached, which leads to isolated branches of localized state with odd and even peaks. The branches start in the region where the trivial state is stable to the region where the trivial state become unstable. For radius 0.9 the LSS also coexist with the stable trivial state and large-amplitude SS producing a homoclinic snaking.

In the case I$-$ with $A < 0$, the normal form shows a TW branch bifurcates subcritically at the primary Hopf bifurcation, and stable SS bifurcate in the primary pitchfork and lose stability to the branch of TW at L_m. This indicates that there is a bistability between two different pairs of states: large-amplitude TW with trivial and SS background. To obtain these states we solved the model using the time-stepping. The trivial state is stable in the region where $\nu < 0, \mu < 0$ and small-amplitude SS is stable in the region between $\mu = 0, \nu < 0$ to L_m. In this case, the stability region from solving the model also agrees with the stability region obtained from the normal form (see Figures 5.10 and 5.11). To obtain the localized state we used a sech envelope to generate initial conditions with different widths and then did the time-stepping. We found localized TW with two different backgrounds: the trivial state background and the SS background. All LTW we found have the same width even for different initial condition width. Doing continuation to obtain the localized TW branch is complicated since the wave depends on space and time. This needs more effort and we aim to make this as future work.

Overall, the model (5.5) shows different interesting types of localized states. Some of these have already been found in other investigations: LSS [11, 12, 74] and

LTW [6, 8, 48, 57–59, 83, 101, 112, 120] with the trivial state in the background in the PDEs for binary and thermosolutal convection. The model shows localized states with background that is different than trivial state: LSS with MW as a background and LTW with SS as a background. These states have been predicted (in a generalized way) from the normal form and to our knowledge no previous investigation has found these states before.

Chapter 6

Conclusion: summary and discussion

In this dissertation, we have developed a simple nonlinear PDE model that replicates the linear behaviour of two-dimensional double-diffusive convection. The model is based on the Swift–Hohenberg equation, which was originally derived to describe the effects of thermal fluctuations and the evolution of roll patterns close to the onset of Rayleigh–Bénard convection and later used as a model of pattern formation in many physical problems. The new model can be reduced further using weakly nonlinear theory to the Takens–Bogdanov normal form where the pitchfork and Hopf bifurcations coincide at the Taken–Bogdanov point. The advantage of the model lies in the relative ease of investigating the nonlinear behaviour numerically and analytically, as compared to the full PDEs of double-diffusive convection. To our knowledge, the model we developed in this dissertation is the first Swift–Hohenberg-type model PDE that has a Takens–Bogdanov primary bifurcation, appropriate for double-diffusive convection. Alongside the numerical results, the model is important for helping to understand the bifurcation structure and the solution behaviour close the Takens–Bogdanov point in an extended system and in particular for investigating localized solutions.

In Chapter 3, we derived the linear and the minimal nonlinear part of the model. The derivation of the linear part comes from understanding the linear part of double-diffusive convection. The linear part of the model has two control parameters μ and ν, where μ controls the pitchfork bifurcation and ν controls the Hopf bifurcation, and takes the form:

$$\frac{\partial^2 u}{\partial t^2} = \left(\mu - \left(k_{\mathrm{cPF}}^2 + \frac{\partial^2}{\partial x^2}\right)^2\right) u + \left(\nu - b\left(k_{\mathrm{cHopf}}^2 + \frac{\partial^2}{\partial x^2}\right)^2\right)\frac{\partial u}{\partial t}, \tag{6.1}$$

where the parameters k_{cPF} and k_{cHopf} are the wavenumbers for the pitchfork and Hopf bifurcations. In this dissertation, we are interested in modelling systems such as thermosolutal [33, 45, 79, 82] and binary convection [10, 52, 54, 112], where the pitchfork and Hopf bifurcations have the same critical wavenumbers (see Figures 1.9 and 1.10), therefore, we assumed $k_{\mathrm{cPF}} = k_{\mathrm{cHopf}} = 1$. For future investigations, if $k_{\mathrm{cPF}} \neq k_{\mathrm{cHopf}}$ then this model could be relevant to other problems where the pitchfork and Hopf bifurcation have different critical wavenumbers, for example magnetoconvection [4, 26, 86, 92, 115] and rotating convection [28, 109, 110, 121].

For the nonlinearities, we considered the global stability based on a Lyapunov function. Many nonlinearities can be added to the model since the model is a second-order partial differential equation in u and u_t and fourth-order in space; some of these nonlinearities, quadratic and cubic in u and u_t and up to two spatial derivatives, are shown in Chapter 3, Section 3.3. In Chapter 3, we aimed to make the model as simple as possible as a starting point for later work. Together with considering the Lyapunov stability, we chose the first nonlinearities $N_1(u, u_t) = Q_1 u^2 + C_1 u^3 + C_2 u^2 u_t + C_4 u_t^3$. Then, we employed weakly nonlinear analysis to reduce the model to the Takens–Bogdanov normal form:

$$\frac{\partial^2 z}{\partial t^2} = \mu z + \nu \frac{\partial z}{\partial t} + A|z|^2 z + C(\frac{\partial z}{\partial t}\bar{z} + z\frac{\partial \bar{z}}{\partial t})z + D|z|^2 \frac{\partial z}{\partial t}, \tag{6.2}$$

where the coefficients A, C and D depend on the parameters Q_1, C_1, C_2, and C_4 (see Section 3.4). The normal form itself was discussed by [34]. Their analysis shows that the normal form has five principle types of solutions including T, SS, TW, SW, and MW. The bifurcation diagrams (the (M, D)-plane) are divided into 8 different regions for $A > 0$ and 18 different regions for $A < 0$ depending on sign M and the value of the ratio $\frac{D}{M}$ (where $M = 2C + D$). The bifurcation structure and stabilities of the solutions are different in each region. We have summarized some of the relevant results obtained by [34] in Chapter 2. Regardless of the fact that the coefficient D in the normal form for thermosolutal and binary convection vanishes (see Section 2.4), we want to make the model as generic as possible to allow a wide range of weakly nonlinear behaviour, including all behaviour exhibited by thermosolutal and binary convection.

Lyapunov stability requires $C_1 < 0, C_2 < 0$ and $C_4 < 0$. With this restriction, we computed A and the fraction $\frac{D}{M}$, and compared with the analysis of the normal form. We found that the initial choice of the nonlinearities N_1 allowed only the case labelled II$-$ with $A < 0$ and $0 < \frac{D}{M} < \frac{1}{2}$ in [34], where steady state (SS) and travelling wave (TW) patterns are the only stable solutions (see Figures 3.6 and 4.3).

To allow the standing wave (SW) and modulated wave (MW) solutions which have been observed in thermosolutal [37, 98] and binary convection [49, 72], we extended the nonlinearities with more terms in Chapter 4. The second set of nonlinearities where $N_2(u, u_t) = Q_1 u^2 + Q_3 u u_{xx} + C_1 u^3 + C_2 u^2 u_t + C_4 u_t^3$. Similarly, we applied weakly nonlinear analysis and computed A and the fraction $\frac{D}{M}$, and compared with the analysis of the normal form. We found that the second set of nonlinearities N_2 allowed the model to match all negative cases with $A < 0$ and cases II$-$ and III$-$ with $A > 0$. In Chapter 4, we focused on case III$-$ with $A < 0$. In this case, the normal form shows stable SW and MW as well as SS and TW (see Figure 4.4). Numerically, we obtained the SS, TW and SW solutions but not the MW solutions, since these are stable only in a very narrow band between the half lines L_H (Hopf bifurcation of MW from TW) and L_{s2} (Hopf bifurcation of MW from SW) (see Figure 4.5).

Our aim in Chapter 5 was to find localized states. In particular, we aimed to identify two types of localized state: localized steady state (LSS) with the trivial state as a background, which was observed numerically in binary convection [11, 74] and in thermosolutal convection [12], and localized travelling wave (LTW) with the trivial state as a background which was observed in binary convection [6, 8, 48, 57–59, 83, 101, 112, 120]. To find localized states, we looked for subcritical pitchfork and Hopf bifurcations, since we expected that subsequent saddle-node bifurcations would lead to stable large-amplitude solutions coexisting with the stable trivial solutions, and possibly then to localized solutions. However, the weakly nonlinear theory with the N_1 and N_2 nonlinearities did not allow subcritical branches at the pitchfork and Hopf bifurcations. Therefore, we extended the model further by adding more nonlinearities. The extended nonlinearities then become $N_3(u, u_t) = Q_1u^2+Q_3uu_{xx}+C_1u^3+C_2u^2u_t+C_4u_t^3+C_5(u_x)^2u_t+C_6uu_xu_{tx}$. This choice allows a subcritical pitchfork (case IV$-$ with $A > 0$, see Figure 5.1 a) and a subcritical Hopf bifurcation (case I$-$ with $A < 0$, see Figure 5.1 b). Therefore, the model we considered in this dissertation with all nonlinearities is

$$\begin{aligned}\frac{\partial^2 u}{\partial t^2} &= \left(\mu - \left(1+\frac{\partial^2}{\partial x^2}\right)^2\right)u + \left(\nu - b\left(1+\frac{\partial^2}{\partial x^2}\right)^2\right)\frac{\partial u}{\partial t}\\ &\quad + Q_1u^2 + Q_3uu_{xx} + C_1u^3 + C_2u^2u_t + C_4u_t^3 + C_5(u_x)^2u_t + C_6uu_xu_{tx}.\end{aligned} \tag{6.3}$$

where μ and ν are the control parameters and the coefficients $Q_1, Q_3, C_1, C_2, C_4, C_5$

and C_6 are constants, constrained only by Lyapunov stability.

From solving the model numerically, we obtained different types of localized states. In case IV$-$ with $A > 0$ (which is the case most relevant to thermosolutal convection, see Section 2.4) and from time stepping, we obtained LSS in the region where there is bistability between the trivial state and a branch of periodic steady states, with $\mu < 0$ and $\nu < 0$ (see Figures 5.2, 5.3 and 5.5 a). We used numerical continuation of the PDE model (6.3) to compute the branches of localized states. The continuation method we used can only find steady solutions, so the model is effectively the steady Swift–Hohenberg equation with solutions depending only on μ – though the stabilities depend on both μ and ν. The solutions are associated with homoclinic connections to the trivial state, in the same manner as the localized solutions in the Swift–Hohenberg equation [18, 20, 23]. The two localized branches with odd and even numbers of peaks add an oscillations on each side as they snake back and forth until they reach the width of the domain, where they terminate on the steady state branch, at the saddle-node bifurcation (see Figures 5.6 and 5.7). In the absence of the saddle-node bifurcation in the periodic state where the left side of the snaking branch cannot be reached, we found isolated branches of LSS (see Figure 5.8). The localized solutions we obtained still exist but are unstable in the region where the trivial state becomes unstable, where $\mu < 0$ and $\nu > 0$.

From time-stepping, we found LSS with an MW background in the region where the large-amplitude SS branch and the small-amplitude SW branch are both stable (see Figures 5.2, 5.3 and 5.5 b). Compared with LSS in the Swift–Hohenberg equation (1.22), where the localized solutions does not depend on time, the fourth-order dynamical system in space of the standard quadratic-cubic

Swift–Hohenberg equation can be written in matrix form as:

$$\frac{d}{dx}\begin{pmatrix} u \\ u_x \\ u_{xx} \\ u_{xxx} \end{pmatrix} = \begin{pmatrix} u_x \\ u_{xx} \\ u_{xxx} \\ (r - q_c^4)u - 2q_c^2 u_{xx} + bu^2 - u^3 \end{pmatrix}. \tag{6.4}$$

When $r < 0$, the linear stability of the fixed point in space has four zero eigenvalues two with positive and two with negative real part, which suggests the existence of homoclinic orbits to the trivial states as $x \to \pm\infty$ (see Section 1.2). The existence of homoclinic orbits is confirmed by the spatial analysis of such type of systems [22, 25, 116]. In LSS with an MW background, two patterns with large-amplitude SS coexist with small-amplitude Hopf bifurcation, which suggests that the localized solutions are heteroclinic orbits between the SS and MW states. Unlike the LSS with the trivial state background, the small-amplitude MW is a time-dependent solutions, which complicates the spatial analysis of the model (6.3). The model (6.3) is a second-order time-dependent and fourth-order in space. Consequently, to prove the existence of heteroclinic orbits between the SS and MW states using spatial dynamics, we need to consider the eight-dimensional problem:

$$\frac{d}{dx}\begin{pmatrix} u \\ u_x \\ u_{xx} \\ u_{xxx} \\ u_t \\ u_{tx} \\ u_{txx} \\ u_{txxx} \end{pmatrix} = \begin{pmatrix} u_x \\ u_{xx} \\ u_{xxx} \\ ? \\ u_{tx} \\ u_{txx} \\ u_{txxx} \\ ? \end{pmatrix}, \tag{6.5}$$

where the question marks indicate u_{xxxx} and u_{txxxx}, which cannot be evaluated easily from the model (6.3). In this case generalized spatial dynamic needs to be considered, this is still an open problem for the future.

In case I− with $A < 0$ and from time stepping, we found LTW with the trivial state background in the region where the trivial state and a large-amplitude branch of TW are stable, with $\mu < 0$ and $\nu < 0$ (see Figures 5.10, 5.11 and 5.12). We also found LTW with SS background in the region where the small-amplitude SS and large-amplitude TW are stable (see Figures 5.10, 5.11 and 5.13). For the given parameter values, the LTW we found all have the same width, regardless of initial conditions. In contrast, LSS exist with a wide range of widths, with different numbers of peaks. We are not able to answer, why we get uniquely selected widths of LTW. One way that may help to answer this question comes from the analysis of Ginzburg–Landau equation [43]. In case of the Swift–Hohenberg equation (1.22), the real Ginzburg–Landau approximation to the Swift–Hohenberg equation for large spatial scale $X = \epsilon x$ and $T = \epsilon^2 t$, close to $r = 0$ is

$$Z_T = rZ - A|Z|^2 Z + 4Z_{XX}, \tag{6.6}$$

where r is the controls parameter and $A = 3 - \frac{38}{9}b^2$ for N_{23}, [20, 69] and $A = -3b$ for N_{35} [23]. This equation is used to approximate several branches of solutions that emerge subcritically close to $r = 0$, including spatially periodic and localized states. The localized solutions for the Swift–Hohenberg equation (1.22), take the form

$$u(x) = \frac{1}{q_c}\left(\frac{2r}{q_c}\right)^{1/2} \operatorname{sech}\left(\frac{x\sqrt{-r}}{2q_c}\right)\cos\left(q_c x + \phi\right) + O(r), \tag{6.7}$$

where q_c is the wavenumber and ϕ is the phase of the pattern within the sech envelope. Therefore, any localized solution close to $r = 0$ has a small-amplitude and takes the width of the sech envelope to contain many wavelengths of the underlying pattern [20, 21]. In the new model (6.3), deriving the Ginzburg–Landau equation for the Takens–Bogdanov normal form may help to convince that the localized travelling wave solutions have the sech envelope similar to the steady state solutions. In Appendix C, we show the derivation of the Ginzburg–Landau equation from the model (6.3) which takes the form

$$\begin{aligned} Z_{TT} =&\mu Z + \nu Z_T + A|Z|^2 Z + C(Z_T\bar{Z} + Z\bar{Z}_T)Z + D|Z|^2 Z_T + 4Z_{XX} + 4bZ_{XXT} \\ &- 4iZ_{XXX} + iKZ^2\bar{Z}_X + iR|Z|^2 Z_X, \end{aligned} \tag{6.8}$$

where μ and ν are the control parameters, the coefficient A is given by (5.4), the coefficients C and D are given by (5.3) and K and R are given by

$$\begin{aligned} K =&\frac{20}{9}Q_3^2 - \frac{38}{9}Q_1Q_3, \\ R =&\frac{32}{27}Q_1^2 + \frac{140}{27}Q_1Q_3 - \frac{136}{27}Q_1Q_3. \end{aligned} \tag{6.9}$$

The analysis of this equation has not been computed, and we aim to address this in future work.

LTW with trivial state background and with uniquely selected widths have also observed in experimental [57, 59, 60, 83] and numerical [6, 8, 103] studies of binary convection. These studies were not carried out close to the Takens–Bogdanov point, so our model does not directly apply here. Nonetheless, we used time stepping in this work to find LTW solutions. Using continuation to compute the LTW solutions would need more effort due to the time and space dependence. The numerical continuation would then require additional unknown variables: the group velocity and the temporal period. An approach to solving this problem is suggested by [112, 114]. We plan to do this as future work.

Lyapunov stability allow us to access all cases within the normal form with $M < 0$, but half the cases of the normal form with $M > 0$ are not accessible. In Table 6.1, we give example choices of parameters $Q_1, Q_3, C_1, C_2, C_4, C_5$, and C_6 for the model (6.3) and the corresponding case in the normal form [34]. The cases shown in blue are the cases we considered in this thesis with the main result found from solving the model numerically. In the last column, we give references to the relevant convection literature.

The model we addressed in this dissertation is one-dimensional $u = u(x, t)$, but it can be easily extended into two dimensions $u = u(x, y, t)$ as long as it satisfies the Lyapunov stability mentioned in Section 3.3. In two dimensions, there are steady hexagons as well as stripes, and many different two-dimensional generalisations of TW and SW [88, 96]. The Takens–Bogdanov normal form in two dimensions has not been fully analysed [90]. This is work for the future.

Case in [34]	Coefficients of the nonlinearities Q_1	Q_3	C_1	C_2	C_4	C_5	C_6	Equation	Main results	Convection references
$A > 0$										
I−	0.8	-0.5	-1	-0.1	-1	-0.1	-5	(4.27)		
II−	1.5	0.5	-1	-1	-1	0	0	(4.27)		
III−	0.1	1.5	-1	-1	-1	0	0	(4.27)		
IV−	0.9	-0.2	-0.2	-1	-1	-0.5	6	(5.5)	SS & SW (Figure 5.2, 5.3)	thermosolutal: [37, 98] binary: [49, 72]
									LSS with T (Figure 5.5 a, 5.7, 5.8)	thermosolutal: [12] binary: [11, 74]
									LSS with MW (Figure 5.5 b)	
$A < 0$										
I−	0.8	0.5	-1	-0.1	-1	-0.1	-5	(5.5)	SS & TW (Figure 5.10,5.11)	thermosolutal: [37, 98, 105] binary: [7, 120]
									LTW with T (Figure 5.12)	binary: [6, 8, 48, 57–59, 83, 101, 112, 120]
									LTW with SS (Figure 5.13)	
II−	0.5	0	-1	-1	-1	0	0	(3.40)	SS & TW (Figure 4.3)	thermosolutal: [37, 98, 105] binary: [7, 120]
III−	0.6	0.9	-1	-1	-1	0	0	(4.27)	SS &TW & SW (Figure 4.4)	thermosolutal: [37, 98, 105] binary: [7, 49, 72, 120]
IV−	0.8	1.1	-1	-1	-1	0	0	(4.27)		
V−	0.85	1.2	-1	-1	-1	0	0	(4.27)		
VI−	0.9	1.21	-1	-1	-1	0	0	(4.27)		
VII−	0.9	1.25	-1	-1	-1	0	0	(4.27)		
VIII−	1	1.4	-1	-1	-1	0	0	(4.27)		
IX−	1.1	1.5	-1	-1	-1	0	0	(4.27)		

Table 6.1: Examples of parameter values for the model (6.3) and the corresponding case in the normal form [34]. The instances in blue indicate the cases we considered in this thesis with the main result. In last column, we give references to the relevant convection literature.

Appendices

A Numerical method

The model (4.29) and later (5.5) is a second order time-dependent PDE that varies both in time and space. A well-known numerical treatment for such types of problems has two essential aspects. Firstly, the spatial part of the PDE is discretized to get a system of ODEs with time as the only independent variable. The approximation for such problems can be made to high accuracy when using spectral methods [24, 30, 46, 50]. For periodic problems with $x \in [0, L]$, the basis functions for spectral methods are Fourier functions, using the Fourier transform to transform from the physical variable x to the Fourier variable k. With N grid points $x_j = j\frac{L}{N}, j = 0, \cdots, N-1$, the discrete Fourier transform is

$$\hat{u}(k) = \frac{1}{N} \sum_{j=0}^{N-1} e^{-kx_j} u(x_j), \qquad k = -\frac{N}{2} + 1, \cdots, \frac{N}{2}, \tag{A.10}$$

and the inverse discrete Fourier transform

$$u(x_j) = \sum_{k=-\frac{N}{2}+1}^{\frac{N}{2}} e^{ikx_j} \hat{u}(k), \qquad j = 0, \cdots N-1. \tag{A.11}$$

We must be aware of the aliasing error which occurs when periodic functions are represented on a finite grid, causing modes with different wavenumbers to become indistinguishable. When computing Fourier transforms of quadratic nonlinear products then the interaction between two Fourier modes could generate higher modes that are the same as the small modes. To deal with this it suffices to measure wavenumbers for the grid in an interval of length 2π. Our basic periodic grid will be a subset of the interval $[0, 2\pi]$. Therefore, in our numerics, we do not do de-aliasing because the numerics well resolved by appling enough grid points.

In problems involving high-order spatial derivatives, the ODEs are usually stiff, so the second step is to solve the ODEs (and hence the PDE) using a time-stepping method appropriate for stiff problems. In stiff systems, the stability of the numerical method can be sensitive to the choice of time step size. One time stepping method that achieves good accuracy and excellent stability in solving stiff systems is the exponential time differencing (ETD) method. The derivation of the ETD schemes is based on integrating the linear (stiffest) part of the differential equation exactly followed by approximating the nonlinear terms [24, 30, 46, 50]. The first-order ETD1 scheme is

$$u_{n+1} = e^{\mathcal{L}h} u_n + \mathcal{L}^{-1} \left(e^{\mathcal{L}h} - 1 \right) N(u_n), \tag{A.12}$$

where $\mathcal{L}$ represents the (matrix) linear part, $N(u_n)$ is the nonlinear term, and h denotes the time step size. ETD1 is used for the first time step, but for subsequent time steps, the second-order ETD2 scheme is

$$u_{n+1} = e^{\mathcal{L}h} u_n + \frac{\left((1 + \mathcal{L}h)\, e^{\mathcal{L}h} - 1 - 2\mathcal{L}h \right)}{h} \mathcal{L}^{-2} N(u_n) + \frac{\left(-e^{\mathcal{L}h} + 1 + \mathcal{L}h \right)}{h} \mathcal{L}^{-2} N(u_{n-1}), \tag{A.13}$$

where $N(u_{n-1})$ is the nonlinear term obtained from the previous step.

The ETD method is particularly convenient if the linear part of the problem is diagonal. In our problem, the linear part is blocked diagonal in Fourier space, with 2 × 2 blocks of the form

$$\mathcal{L} = \begin{bmatrix} 0 & 1 \\ \mu - (1-k^2) & \nu - b\,(1-k^2) \end{bmatrix}. \tag{A.14}$$

From testing the eigenvalues in our problem, we found that we have some eigenvalues close to zero while the others are big or far from zero. When some of the eigenvalues $\mathcal{L}$ are equal or close to zero, the explicit formulas for the ETD coefficients in (A.12) and (A.13) cannot be used directly, since this leads to rounding errors occurring due to the cancellation in the coefficients of $N(u_n)$ and $N(u_{n-1})$ above. This problem has been discussed by [50]. The solution is to approximate the coefficients using contour integrals in the complex plane.

Contour integration is a method of evaluating the coefficients accurately by replacing them by contour integrals using the Cauchy integral formula:

$$F(\mathcal{L}) = \frac{1}{2\pi i}\int_{\Gamma} (TI - \mathcal{L})^{-1}\, F(T) dT, \tag{A.15}$$

where I is the identity matrix. The contour Γ is defined as

$$T(\theta) = z_0 + re^{i\theta} \qquad 0 \le \theta \le 2\pi, \tag{A.16}$$

where r is the radius and z_0 is the centre. Substituting in (A.15), we get

$$F(\mathcal{L}) = \frac{1}{2\pi}\int_0^{2\pi} \left(\left(z_0 + re^{i\theta}\right) I - \mathcal{L}\right)^{-1} F\left(z_0 + re^{i\theta}\right)\left(re^{i\theta}\right) d\theta, \tag{A.17}$$

where $\left(\left(z_0 + re^{i\theta}\right) I - \mathcal{L}\right)^{-1}$ is the resolvent matrix. From the trapezoidal rule, we have

$$\int_0^{2\pi} F(\theta) \approx \frac{2\pi}{M}\sum_{i=1}^{M} F(\theta_i), \qquad \theta_i = \frac{2\pi i}{M}, i = 1, 2, ..., M. \tag{A.18}$$

Applying the trapezoidal rule in (A.17), we have

$$F(\mathcal{L}) = \frac{1}{M}\sum_{i=1}^{M} F\left(z_0 + re^{i\theta}\right)\left(\left(z_0 + re^{i\theta}\right)I - \mathcal{L}\right)^{-1}\left(re^{i\theta}\right)d\theta, \tag{A.19}$$

we use $M = 16$. This approximation depends on choosing the centre z_0 and the radius of the circular contour to enclose all eigenvalues of the matrix $\mathcal{L}$. For eigenvalues far from zero; the explicit formulas for ETD in (A.12) and (A.13) give better approximations than the contour integral. Therefore, in our calculation and for each value of k in spectral space, we check the magnitude of the eigenvalues of $\mathcal{L}$ in (A.14). If both eigenvalues smaller than 0.5 in magnitude, we apply the contour integral with radius 2 and centre zero. If this not the case we use the direct formulas for the ETD coefficients in (A.12) and (A.13) even if one eigenvalue is smaller than 0.5. We tried other approaches (using large circles, using multiple circles, and using Taylor expansions) but the method described above proved to be the most satisfactory.

B Numerical continuation

Numerical continuation is a tool that is used to trace out a curve of solutions to the nonlinear system (5.5) using a pseudo-arclength continuation method [40] together with Newton's method [1, 40], which we will mention separately in the next sections.

The problem takes the form

$$F(\mathbf{u}, \mu) = 0, \tag{B.20}$$

where $\mathbf{u}(\mu)$ is a branch of solutions we want to calculate depending on the parameter μ as the only parameter that is varied. With N grid points, the solution $\mathbf{u}$ is a vector containing a series of values $\mathbf{u}_i$ on each grid point x_i where $(i = 1, \cdots, N)$.

B.1 Pseudo-arclength continuation

We apply the pseudo-arclength continuation to solve the system (B.20) since we expect the solutions to move along the curve as the parameter μ varies (such as in Figure 5.7). Therefore, the ideal parameterization of a curve is the arclength s; the solutions $\mathbf{u}$ and the parameter μ can be treated in terms of s as follows:

$$F(\mathbf{u}(s), \mu(s)) = 0. \tag{B.21}$$

With the pseudo-arclength constraint s the equation (B.21) has N equations with $N+1$ unknown parameters. Therefore, we require an additional equations that we should add to the system. This equation comes from the orthogonality condition, to obtain the subsequent solutions around the curve. Suppose we have two points on the branch s_0 and s_1 then the next point on the branch should be in a plane that is orthogonal to a straight line connecting the two previous points. From the last two solutions $(\mathbf{u}(s_0), \mu(s_0))$ and $(\mathbf{u}(s_1), \mu(s_1))$, which obtain using Newton solver (see below), we measure the arclength distance as follows:

$$\frac{d\mathbf{u}}{ds} = \frac{\mathbf{u}(s_1) - \mathbf{u}(s_0)}{s_1 - s_0}, \qquad \frac{d\mu}{ds} = \frac{\mu(s_1) - \mu(s_0)}{s_1 - s_0}. \tag{B.22}$$

Then we predict the next step $(\mathbf{u}(s_p), \mu(s_p))$, which lies in a straight line from the last two solutions as follows:

$$\mathbf{u}_p = \mathbf{u}(s_1) + \Delta s\frac{d\mathbf{u}}{ds}, \qquad \mu_p = \mu(s_1) + \Delta s\frac{d\mu}{ds}, \tag{B.23}$$

where Δs refers to the stepsize. The predicted step $(\mathbf{u}(s_p), \mu(s_p))$ then is used as initial iterate for a Newton method to solve (B.21) and find the next solution $(\mathbf{u}, \mu)$ which should satisfy the orthogonality condition:

$$(\mathbf{u} - \mathbf{u}_p) \cdot \frac{d\mathbf{u}}{ds} + (\mu - \mu_p)\frac{d\mu}{ds} = 0. \tag{B.24}$$

With this condition, we can solve $N + 1$ equations with $N + 1$ parameters and the system we want to solve becomes

$$G(\mathbf{u}, \mu) = \begin{pmatrix} F(\mathbf{u}, \mu) \\ \text{orthogonality condition (B.24)} \end{pmatrix}. \tag{B.25}$$

Then we solve $G(\mathbf{u}, \mu) = 0$ using the Newton method to obtain the next solution on the branch $(\mathbf{u}(s_2), \mu(s_2))$ where s_2 is

$$s_2 = s_1 + \frac{1}{N}(\mathbf{u}(s_2) - \mathbf{u}(s_1)) \cdot \frac{d\mathbf{u}}{ds} + (\mu(s_2) - \mu(s_1))\frac{d\mu}{ds}. \tag{B.26}$$

Once we obtain the next solution, the method takes the last two solutions $(\mathbf{u}(s_1), \mu(s_1))$ and $(\mathbf{u}(s_2), \mu(s_2))$ to predict the next solution using (B.22) and

(B.23) with replacing s_1 by s_2 and s_0 by s_1, and so on. Following this process, we are able to obtain all the solutions around the branch.

B.2 Newton's method

We use Newton's method [16] to solve the system $G(X) = 0$, where $X = (\mathbf{u}, \mu)$ starting from sufficiently accurate initial guess X_0, for example obtained from time stepping in our problem or from a prediction from previous points on the branch. From this method, there is a set of solutions X_n given by

$$X_{n+1} = X_n - \left(\frac{\partial G}{\partial X_n}\right)^{-1} G(X_n), \qquad n > 0, \tag{B.27}$$

that converges to the solutions of $G(X_n) = 0$ as $n \to \infty$, for a close enough initial guess X_0, where $\left(\frac{\partial G}{\partial X_n}\right)^{-1}$ is the inverse of the Jacobian. Finding the inverse of a large matrix in (B.27) is too expensive. Therefore, instead of finding the inverse we assume a small perturbation δX_n and solve the equation

$$P \cdot \frac{\partial G}{\partial X_n} \cdot \delta X_n = P \cdot G(X_n), \tag{B.28}$$

where P is a linear preconditioner (see below). This equation is solved using the biconjugate gradient stabilized method [106] (bicgstab in MATLAB) to find δX_n. The biconjugate gradient stabilized method is an iterative method used to solve the linear equation (B.28) for δX_n by allowing to specify the tolerance B_{tol} and the maximum number of iterations. The bicgstab method is iterative until satisfies the tolerance, which we chose to be

$$B_{tol} = 10^{-15} \frac{||X_n||}{||G(X_n)||}. \tag{B.29}$$

When bicgstab does converge to the requested tolerance within the requested iterations (which we chose to be 200), we have δX_n. Then we update the state from (B.27) as follows:

$$X_{n+1} = X_n - \delta X_n, \qquad n > 0, \tag{B.30}$$

This Newton method iterates until convergence when

$$||G(X_n)||< 10^{-13}||X_n||. \tag{B.31}$$

In our calculation, we need to implement a preconditioner that helps the biconjugate gradient stabilized method to converge more quickly. Therefore, we find the preconditioner, which is the inverse of the linear part $P = \mathcal{L}^{-1}$.

C Derivation of the Ginzburg–Landau approximation to the model (6.3)

We introduce a small parameter $\epsilon \ll 1$, define a large spatial scale $X = \epsilon x$ and scale the parameters μ, ν and the time similar to the scaling we used in the weakly nonlinear method as follows

$$\frac{\partial}{\partial t} \to \epsilon \frac{\partial}{\partial T}, \ \mu \to \epsilon^2 \mu_2, \ \nu \to \epsilon^2 \nu_2, \tag{C.32}$$

and look for solutions of the form

$$u(x) = \epsilon u_1(x, X) + \epsilon^2 u_2(x, X) + \epsilon^3 u_3(x, X) + \epsilon^4 u_4(x, X) + \cdots. \tag{C.33}$$

With this scaling $\left(1 + \frac{\partial^2}{\partial x^2}\right)^2 u$ and $\left(1 + \frac{\partial^2}{\partial x^2}\right)^2 u_t$ in the model (6.3) become

$$\begin{aligned} \left(1 + \frac{\partial^2}{\partial x^2}\right)^2 u =& \left(u + 2u_{xx} + u_{xxxx}\right) + 4\epsilon \left(u_{Xx} + u_{xxxX}\right) \\ & + \epsilon^2 \left(2u_{XX} + 6u_{xxXX}\right) + 4\epsilon^3 u_{xXXX} + \epsilon^4 u_{XXXX}, \\ \left(1 + \frac{\partial^2}{\partial x^2}\right)^2 u_t =& \epsilon \left(u_T + 2u_{xxT} + u_{xxxxT}\right) + 4\epsilon^2 \left(u_{xXT} + u_{xxxXT}\right) \\ & + \epsilon^3 \left(2u_{XXT} + 6u_{xxXXT}\right) + 4\epsilon^4 u_{xXXXT} + O(\epsilon^5), \end{aligned} \tag{C.34}$$

Substituting the expansion and scaling in the PDE (6.3) and matching terms order by order in ϵ, we get

$$O(\epsilon): \quad \mathcal{L}u_1 = 0,$$

$$O(\epsilon^2): \quad -\mathcal{L}u_2 - 4\left(\partial_{xX} + \partial_{xxxX}\right) u_1 - b\mathcal{L}\frac{\partial u_1}{\partial T} + Q_1 u_1^2 + Q_3 u_1 \partial_{xx} u_1 = 0,$$

$$
\begin{aligned}
O(\epsilon^3): \quad \frac{\partial^2 u_1}{\partial T^2} &= \mu u_1 - \mathcal{L} u_3 - 4\left(\partial_{xX} + \partial_{xxxX}\right) u_2 - \left(2\partial_{XX} + 6\partial_{xxXX}\right) u_1 \\
&- b\mathcal{L}\frac{\partial u_2}{\partial T} + 2Q_1 u_1 u_2 - 4b\left(\partial_{xX} + \partial_{xxxX}\right)\frac{\partial u_1}{\partial T} \\
&+ Q_3\left(2u_1\partial_{xX}u_1 + u_1\partial_{xx}u_2 + u_2\partial_{xx}u_1\right) + C_1 u_1^3,
\end{aligned}
$$

$$
\begin{aligned}
O(\epsilon^4): \quad \frac{\partial^2 u_2}{\partial T^2} &= \mu u_2 - \mathcal{L} u_4 - 4\left(\partial_{xX} + \partial_{xxxX}\right) u_3 - \left(2\partial_{XX} + 6\partial_{xxXX}\right) u_2 \\
&- 4\partial_{xXXX}u_1 + \nu\frac{\partial u_1}{\partial T} - b\mathcal{L}\frac{\partial u_3}{\partial T} - b\left(2\partial_{XX} + 6\partial_{xxXX}\right)\frac{\partial u_1}{\partial T} \\
&- 4\partial_{xXXX}\frac{\partial u_1}{\partial T} + Q_1\left(u_2^2 + 2u_1u_3\right) \\
&+ Q_3\left(u_1\partial_{XX}u_1 + 2u_1\partial_{xX}u_2 + 2u_2\partial_{xX}u_1 + u_1\partial_{xx}u_3 + u_2\partial_{xx}u_2 + u_3\partial_{xx}u_1\right) \\
&+ 3C_1u_1^2\frac{\partial u_1}{\partial T} + C_2u_1^2\frac{\partial u_1}{\partial T} + C_3\left(\frac{\partial u_1}{\partial T}\right)^3 + C_4\left(\partial_x u_1\right)^2\frac{\partial u_1}{\partial T} + C_5u_1\partial_x u_1\partial_x\frac{\partial u_1}{\partial T},
\end{aligned}
\tag{C.35}
$$

where

$$
\mathcal{L} = -\left(1 + 2\partial_{xx} + \partial_{xxxx}\right). \tag{C.36}
$$

The equations are solved by

$$
\begin{aligned}
u_1(x,t) =& F_1(X,T)e^{ix} + \bar{F}_1(X,T)e^{-ix}, \\
u_2(x,t) =& G_2(X,T)e^{2ix} + G_1(X,T)e^{ix} + G_0(X,T) + \bar{G}_1(X,T)e^{-ix} + \bar{G}_2(X,T)e^{-2ix}, \\
u_3(x,t) =& H_3(X,T)e^{3ix} + H_2(X,T)e^{2ix} + H_1(X,T)e^{ix} + H_0(X,T) + \bar{H}_1(X,T)e^{-ix} \\
&+ \bar{H}_2(X,T)e^{-2ix} + \bar{H}_3(X,T)e^{-3ix}.
\end{aligned}
\tag{C.37}
$$

and use the same process in derivation the Takens–Bogdanov normal form (see Section 3.4), we obtain the Ginzburg–Landau equation (6.8).

Bibliography

[1] Allgower, E. L. and Georg, K. [2003], *Introduction to numerical continuation methods*, Vol. 45, SIAM.

[2] Alnahdi, A., Niesen, J. and Rucklidge, A. M. [2014], 'Localized patterns in periodically forced systems', *SIAM Journal on Applied Dynamical Systems* **13**(3), 1311–1327.

[3] Alnahdi, A., Niesen, J. and Rucklidge, A. M. [2018], 'Localized patterns in periodically forced systems: II. patterns with nonzero wavenumber', *SIAM Journal on Applied Dynamical Systems* **17**(2), 1478–1502.

[4] Arter, W. [1983], 'Nonlinear convection in an imposed horizontal magnetic field', *Geophysical & Astrophysical Fluid Dynamics* **25**(4), 259–292.

[5] Baines, P. and Gill, A. [1969], 'On thermohaline convection with linear gradients', *Journal of Fluid Mechanics* **37**(2), 289–306.

[6] Barten, W., Lücke, M. and Kamps, M. [1991], 'Localized traveling-wave convection in binary-fluid mixtures', *Physical Review letters* **66**(20), 2621.

[7] Barten, W., Lücke, M., Kamps, M. and Schmitz, R. [1995*a*], 'Convection in binary fluid mixtures. I. extended traveling-wave and stationary states', *Physical Review E* **51**(6), 5636.

[8] Barten, W., Lücke, M., Kamps, M. and Schmitz, R. [1995*b*], 'Convection

in binary fluid mixtures. II. localized traveling waves', *Physical Review E* **51**(6), 5662.

[9] Batchelor, C. K. and Batchelor, G. [2000], *An introduction to fluid dynamics*, Cambridge University Press.

[10] Batiste, O. and Knobloch, E. [2005], 'Simulations of localized states of stationary convection in He3-He4 mixtures', *Physical Review letters* **95**(24), 244501.

[11] Batiste, O., Knobloch, E., Alonso, A. and Mercader, I. [2006], 'Spatially localized binary-fluid convection', *Journal of fluid mechanics* **560**, 149–158.

[12] Beaume, C., Bergeon, A. and Knobloch, E. [2011], 'Homoclinic snaking of localized states in doubly diffusive convection', *Physics of Fluids* **23**(9), 094102.

[13] Beaume, C., Bergeon, A. and Knobloch, E. [2013], 'Convectons and secondary snaking in three-dimensional natural doubly diffusive convection', *Physics of fluids* **25**(2), 024105.

[14] Beaume, C., Bergeon, A. and Knobloch, E. [2018], 'Three-dimensional doubly diffusive convectons: instability and transition to complex dynamics', *Journal of Fluid Mechanics* **840**, 74–105.

[15] Beck, M., Knobloch, J., Lloyd, D. J., Sandstede, B. and Wagenknecht, T. [2009], 'Snakes, ladders, and isolas of localized patterns', *SIAM Journal on Mathematical Analysis* **41**(3), 936–972.

[16] Bender, C. M. and Orszag, S. A. [2013], *Advanced mathematical methods for scientists and engineers I: Asymptotic methods and perturbation theory*, Springer Science & Business Media.

[17] Bodenschatz, E., Pesch, W. and Ahlers, G. [2000], 'Recent developments in Rayleigh–Bénard convection', *Annual review of fluid mechanics* **32**(1), 709–778.

[18] Burke, J. and Dawes, J. H. [2012], 'Localized states in an extended Swift–Hohenberg equation', *SIAM Journal on Applied Dynamical Systems* **11**(1), 261–284.

[19] Burke, J., Houghton, S. and Knobloch, E. [2009], 'Swift–Hohenberg equation with broken reflection symmetry', *Physical Review E* **80**(3), 036202.

[20] Burke, J. and Knobloch, E. [2006], 'Localized states in the generalized Swift–Hohenberg equation', *Physical Review E* **73**(5), 056211.

[21] Burke, J. and Knobloch, E. [2007*a*], 'Homoclinic snaking: structure and stability', *Chaos: An Interdisciplinary Journal of Nonlinear Science* **17**(3), 037102.

[22] Burke, J. and Knobloch, E. [2007*b*], 'Normal form for spatial dynamics in the Swift–Hohenberg equation', *Dynamical Systems* **2007**, 1–10.

[23] Burke, J. and Knobloch, E. [2007*c*], 'Snakes and ladders: localized states in the Swift–Hohenberg equation', *Physics Letters A* **360**(6), 681–688.

[24] Canuto, C., Hussaini, M. Y., Quarteroni, A., Thomas Jr, A. et al. [2012], *Spectral methods in fluid dynamics*, Springer Science & Business Media.

[25] Champneys, A. R. [1998], 'Homoclinic orbits in reversible systems and their applications in mechanics, fluids and optics', *Physica D: Nonlinear Phenomena* **112**(1-2), 158–186.

[26] Chandrasekhar, S. [2013], *Hydrodynamic and hydromagnetic stability*, Courier Corporation.

[27] Chapman, S. J. and Kozyreff, G. [2009], ‘Exponential asymptotics of localised patterns and snaking bifurcation diagrams’, *Physica D: Nonlinear Phenomena* **238**(3), 319–354.

[28] Clune, T. and Knobloch, E. [1993], ‘Pattern selection in rotating convection with experimental boundary conditions’, *Physical Review E* **47**(4), 2536.

[29] Coullet, P., Riera, C. and Tresser, C. [2000], ‘Stable static localized structures in one dimension’, *Physical Review letters* **84**(14), 3069.

[30] Cox, S. M. and Matthews, P. C. [2002], ‘Exponential time differencing for stiff systems’, *Journal of Computational Physics* **176**(2), 430–455.

[31] Crawford, C. and Riecke, H. [1999], ‘Oscillon-type structures and their interaction in a Swift–Hohenberg model’, *Physica D: Nonlinear Phenomena* **129**(1-2), 83–92.

[32] Cross, M. C. and Hohenberg, P. C. [1993], ‘Pattern formation outside of equilibrium’, *Rev. Mod. Phys.* **65**, 851–1112.
URL: *https://0-link-aps-org.wam.leeds.ac.uk/doi/10.1103/RevModPhys.65.851*

[33] Da Costa, L., Knobloch, E. and Weiss, N. [1981], ‘Oscillations in double-diffusive convection’, *Journal of Fluid Mechanics* **109**, 25–43.

[34] Dangelmayr, G. and Knobloch, E. [1987], ‘The Takens–Bogdanov bifurcation with O(2)-symmetry’, *Phil. Trans. R. Soc. Lond. A* **322**(1565), 243–279.

[35] Dawes, J. [2010], ‘The emergence of a coherent structure for coherent structures: localized states in nonlinear systems’, *Philosophical Transactions of the Royal Society A: Mathematical, Physical and Engineering Sciences* **368**(1924), 3519–3534.

[36] Deane, A., Knobloch, E. and Toomre, J. [1987], ‘Traveling waves and chaos in thermosolutal convection’, *Physical Review A* **36**(6), 2862.

[37] Deane, A., Knobloch, E. and Toomre, J. [1988], 'Traveling waves in large-aspect-ratio thermosolutal convection', *Physical Review A* **37**(5), 1817.

[38] Decker, W. and Pesch, W. [1994], 'Order parameter and amplitude equations for the Rayleigh–Bénard convection', *Journal de Physique II* **4**(3), 419–438.

[39] Drazin, P. G. [2002], *Introduction to hydrodynamic stability*, Vol. 32, Cambridge University Press.

[40] Govaerts, W. J. [2000], *Numerical methods for bifurcations of dynamical equilibria*, Vol. 66, SIAM.

[41] Greenside, H., Coughran Jr, W. and Schryer, N. [1982], 'Nonlinear pattern formation near the onset of Rayleigh–Bénard convection', *Physical Review Letters* **49**(10), 726.

[42] Houghton, S. and Knobloch, E. [2009], 'Homoclinic snaking in bounded domains', *Physical Review E* **80**(2), 026210.

[43] Hoyle, R. [2006], *Pattern formation: an introduction to methods*, Cambridge University Press.

[44] Hunt, G. W., Peletier, M. A., Champneys, A. R., Woods, P. D., Wadee, M. A., Budd, C. J. and Lord, G. J. [2000], 'Cellular buckling in long structures', *Nonlinear Dynamics* **21**(1), 3–29.

[45] Huppert, H. E. and Moore, D. R. [1976], 'Nonlinear double-diffusive convection', *Journal of Fluid Mechanics* **78**(4), 821–854.

[46] Hussaini, M. Y. and Zang, T. A. [1987], 'Spectral methods in fluid dynamics', *Annual review of fluid mechanics* **19**(1), 339–367.

[47] Iooss, G. and Pérouème, M.-C. [1993], 'Perturbed homoclinic solutions in reversible 1: 1 resonance vector fields', *J. Diff. Eqns* **102**(1), 62–88.

[48] Jung, D. and Lücke, M. [2005], 'Traveling wave fronts and localized traveling wave convection in binary fluid mixtures', *Physical Review E* **72**(2), 026307.

[49] Jung, D., Matura, P. and Lücke, M. [2004], 'Oscillatory convection in binary mixtures: Thermodiffusion, solutal buoyancy, and advection', *The European Physical Journal E* **15**(3), 293–304.

[50] Kassam, A.-K. and Trefethen, L. N. [2005], 'Fourth-order time-stepping for stiff PDEs', *SIAM Journal on Scientific Computing* **26**(4), 1214–1233.

[51] Kirk, V. and Rucklidge, A. M. [2008], 'The effect of symmetry breaking on the dynamics near a structurally stable heteroclinic cycle between equilibria and a periodic orbit', *Dynamical Systems* **23**(1), 43–74.

[52] Knobloch, E. [1986], 'Oscillatory convection in binary mixtures', *Physical Review A* **34**(2), 1538.

[53] Knobloch, E. [2015], 'Spatial localization in dissipative systems', *Ann. Rev. Condens. Matter Phys.* **6**(1), 325–359.

[54] Knobloch, E. and Moore, D. R. [1990], 'Minimal model of binary fluid convection', *Physical Review A* **42**(8), 4693.

[55] Knobloch, E., Moore, D. R., Toomre, J. and Weiss, N. O. [1986], 'Transitions to chaos in two-dimensional double-diffusive convection', *Journal of Fluid Mechanics* **166**, 409–448.

[56] Knobloch, E. and Proctor, M. [1981], 'Nonlinear periodic convection in double-diffusive systems', *Journal of Fluid Mechanics* **108**, 291–316.

[57] Kolodner, P. [1991*a*], 'Collisions between pulses of traveling-wave convection', *Physical Review A* **44**(10), 6466.

[58] Kolodner, P. [1991*b*], 'Drift, shape, and intrinsic destabilization of pulses of traveling-wave convection', *Physical Review A* **44**(10), 6448.

[59] Kolodner, P. [1991*c*], 'Stable and unstable pulses of traveling-wave convection', *Physical Review A* **43**(6), 2827.

[60] Kolodner, P. [1994], 'Stable, unstable, and defected confined states of traveling-wave convection', *Physical Review E* **50**(4), 2731.

[61] Kolodner, P., Passner, A., Surko, C. and Walden, R. [1986], 'Onset of oscillatory convection in a binary fluid mixture', *Physical Review letters* **56**(24), 2621.

[62] Kolodner, P., Surko, C. and Williams, H. [1989], 'Dynamics of traveling waves near the onset of convection in binary fluid mixtures', *Physica D: Nonlinear Phenomena* **37**(1-3), 319–333.

[63] Koschmieder, E. L. [1993], *Bénard cells and Taylor vortices*, Cambridge University Press.

[64] Kozyreff, G. and Tlidi, M. [2007], 'Nonvariational real Swift–Hohenberg equation for biological, chemical, and optical systems', *Chaos: An Interdisciplinary Journal of Nonlinear Science* **17**(3), 037103.

[65] Kreyszig, E. [1978], *Introductory functional analysis with applications*, Vol. 1, wiley New York.

[66] Lappa, M. [2009], *Thermal convection: patterns, evolution and stability*, John Wiley & Sons.

[67] Lloyd, D. J., Sandstede, B., Avitabile, D. and Champneys, A. R. [2008], 'Localized hexagon patterns of the planar Swift–Hohenberg equation', *SIAM Journal on Applied Dynamical Systems* **7**(3), 1049–1100.

[68] Lloyd, D. and Sandstede, B. [2009], 'Localized radial solutions of the Swift–Hohenberg equation', *Nonlinearity* **22**(2), 485.

[69] M' F, H., Métens, S., Borckmans, P. and Dewel, G. [1995], 'Pattern selection in the generalized Swift–Hohenberg model', *Physical Review E* **51**(3), 2046.

[70] Mandel, P. [2005], *Theoretical problems in cavity nonlinear optics*, Vol. 21, Cambridge University Press.

[71] Manneville, P. [2006], Rayleigh–Bénard convection: thirty years of experimental, theoretical, and modeling work, *in* 'Dynamics of Spatio-Temporal Cellular Structures', Springer, pp. 41–65.

[72] Matura, P., Jung, D. and Lücke, M. [2004], 'Standing-wave oscillations in binary mixture convection: From the onset via symmetry breaking to period doubling into chaos', *Physical Review letters* **92**(25), 254501.

[73] McCalla, S. and Sandstede, B. [2010], 'Snaking of radial solutions of the multi-dimensional Swift–Hohenberg equation: A numerical study', *Physica D: Nonlinear Phenomena* **239**(16), 1581–1592.

[74] Mercader, I., Batiste, O., Alonso, A. and Knobloch, E. [2009], 'Localized pinning states in closed containers: homoclinic snaking without bistability', *Physical Review E* **80**(2), 025201.

[75] Mercader, I., Batiste, O., Alonso, A. and Knobloch, E. [2011], 'Convectons, anticonvectons and multiconvectons in binary fluid convection', *Journal of fluid mechanics* **667**, 586–606.

[76] Mercader, I., Batiste, O., Alonso, A. and Knobloch, E. [2013], 'Travelling convectons in binary fluid convection', *Journal of fluid mechanics* **722**, 240–266.

[77] Moore, D., Toomre, J., Knobloch, E. and Weiss, N. [1983], 'Period doubling and chaos in partial differential equations for thermosolutal convection', *Nature* **303**(5919), 663.

[78] Moore, D. W. and Spiegel, E. A. [1966], 'A thermally excited non-linear oscillator', *The Astrophysical Journal* **143**, 871.

[79] Moore, D., Weiss, N. and Wilkins, J. [1991], 'Asymmetric oscillations in thermosolutal convection', *Journal of Fluid Mechanics* **233**, 561–585.

[80] Newell, A. C., Passot, T. and Lega, J. [1993], 'Order parameter equations for patterns', *Annual review of fluid mechanics* **25**(1), 399–453.

[81] Nicolis, G. [1995], *Introduction to nonlinear science*, Cambridge University Press.

[82] Nield, D. [1967], 'The thermohaline Rayleigh-Jeffreys problem', *Journal of Fluid Mechanics* **29**(3), 545–558.

[83] Niemela, J. J., Ahlers, G. and Cannell, D. S. [1990], 'Localized traveling-wave states in binary-fluid convection', *Physical Review letters* **64**(12), 1365.

[84] Platten, J. K. [2006], 'The Soret effect: a review of recent experimental results', *Journal of applied mechanics* **73**(1), 5–15.

[85] Predtechensky, A., McCormick, W., Swift, J., Rossberg, A. and Swinney, H. L. [1994], 'Traveling wave instability in sustained double-diffusive convection', *Physics Of Fluids* **6**(12), 3923–3935.

[86] Proctor, M. and Weiss, N. [1982], 'Magnetoconvection', *Reports on Progress in Physics* **45**(11), 1317.

[87] Rayleigh, L. [1916], 'On convection currents in a horizontal layer of fluid, when the higher temperature is on the under side', *The London, Edinburgh, and Dublin Philosophical Magazine and Journal of Science* **32**(192), 529–546.

[88] Roberts, M., Swift, J. W. and Wagner, D. H. [1986], *The Hopf bifurcation on a hexagonal lattice*, University of Warwick.

[89] Rucklidge, A. [1992], 'Chaos in models of double convection', *Journal of Fluid Mechanics* **237**, 209–229.

[90] Rucklidge, A. [2001], 'Global bifurcations in the Takens–Bogdanov normal form with D4 symmetry near the O (2) limit', *Physics Letters A* **284**(2-3), 99–111.

[91] Rucklidge, A. M. and Silber, M. [2009], 'Design of parametrically forced patterns and quasipatterns', *SIAM Journal on Applied Dynamical Systems* **8**(1), 298–347.

[92] Rucklidge, A., Weiss, N., Brownjohn, D. and Proctor, M. [1993], 'Oscillations and secondary bifurcations in nonlinear magnetoconvection', *Geophysical & Astrophysical Fluid Dynamics* **68**(1-4), 133–150.

[93] Sakaguchi, H. and Brand, H. R. [1996], 'Stable localized solutions of arbitrary length for the quintic Swift–Hohenberg equation', *Physica D: Nonlinear Phenomena* **97**(1-3), 274–285.

[94] Schlüter, A., Lortz, D. and Busse, F. [1965], 'On the stability of steady finite amplitude convection', *Journal of Fluid Mechanics* **23**(1), 129–144.

[95] Schneider, T. M., Gibson, J. F. and Burke, J. [2010], 'Snakes and ladders: localized solutions of plane Couette flow', *Physical Review letters* **104**(10), 104501.

[96] Silber, M. and Knobloch, E. [1991], 'Hopf bifurcation on a square lattice', *Nonlinearity* **4**(4), 1063.

[97] Spiegel, E. A. and Veronis, G. [1960], 'On the Boussinesq approximation for a compressible fluid.', *The Astrophysical Journal* **131**, 442.

[98] Spina, A., Toomre, J. and Knobloch, E. [1998], 'Confined states in large-aspect-ratio thermosolutal convection', *Physical Review E* **57**(1), 524.

[99] Stern, M. E. [1960], 'The "salt-fountain" and thermohaline convection', *Tellus* **12**(2), 172–175.

[100] Subramanian, P., Archer, A. J., Knobloch, E. and Rucklidge, A. M. [2018], 'Spatially localized quasicrystalline structures', *New Journal of Physics* **20**(12), 122002.

[101] Surko, C., Ohlsen, D. R., Yamamoto, S. and Kolodner, P. [1991], 'Confined states of traveling-wave convection', *Physical Review A* **43**(12), 7101.

[102] Swift, J. and Hohenberg, P. C. [1977], 'Hydrodynamic fluctuations at the convective instability', *Phys. Rev. A* **15**, 319–328.
URL: *https://link.aps.org/doi/10.1103/PhysRevA.15.319*

[103] Taraut, A., Smorodin, B. and Lücke, M. [2012], 'Collisions of localized convection structures in binary fluid mixtures', *New journal of physics* **14**(9), 093055.

[104] Tritton, D. J. [2012], *Physical fluid dynamics*, Springer Science & Business Media.

[105] Turton, S. E., Tuckerman, L. S. and Barkley, D. [2015], 'Prediction of frequencies in thermosolutal convection from mean flows', *Physical Review E* **91**(4), 043009.

[106] Van der Vorst, H. A. [1992], 'Bi-cgstab: A fast and smoothly converging variant of Bi-CG for the solution of nonsymmetric linear systems', *SIAM Journal on scientific and Statistical Computing* **13**(2), 631–644.

[107] Velarde, M. G. and Normand, C. [1980], 'Convection', *Scientific American* **243**(1), 92–109.

[108] Veronis, G. [1965], 'On finite amplitude instability in thermohaline convection', *J. mar. Res* **23**(1), 1–17.

[109] Veronis, G. [1966], ‘Motions at subcritical values of the Rayleigh number in a rotating fluid’, *Journal of Fluid Mechanics* **24**(3), 545–554.

[110] Veronis, G. [1968], ‘Large-amplitude Bénard convection in a rotating fluid’, *Journal of Fluid Mechanics* **31**(1), 113–139.

[111] Viñals, J., Xi, H.-W. and Gunton, J. [1992], ‘Numerical study of the influence of forcing terms and fluctuations near onset on the roll pattern in Rayleigh–Bénard convection in a simple fluid’, *Physical Review A* **46**(2), 918.

[112] Watanabe, T., Iima, M. and Nishiura, Y. [2012], ‘Spontaneous formation of travelling localized structures and their asymptotic behaviour in binary fluid convection’, *Journal of Fluid Mechanics* **712**, 219–243.

[113] Watanabe, T., Iima, M. and Nishiura, Y. [2016], ‘A skeleton of collision dynamics: Hierarchical network structure among even-symmetric steady pulses in binary fluid convection’, *SIAM Journal on Applied Dynamical Systems* **15**(2), 789–806.

[114] Watanabe, T., Toyabe, K., Iima, M. and Nishiura, Y. [2011], ‘Time-periodic traveling solutions of localized convection cells in binary fluid mixture’, *Theoretical and Applied Mechanics Japan* **59**, 211–219.

[115] Weiss, N. [1981], ‘Convection in an imposed magnetic field. part 1. the development of nonlinear convection’, *Journal of Fluid Mechanics* **108**, 247–272.

[116] Woods, P. and Champneys, A. [1999], ‘Heteroclinic tangles and homoclinic snaking in the unfolding of a degenerate reversible Hamiltonian–Hopf bifurcation’, *Physica D: Nonlinear Phenomena* **129**(3-4), 147–170.

[117] Xi, H.-w., Gunton, J. and Vinals, J. [1993], ‘Spiral defect chaos in a model of Rayleigh–Bénard convection’, *Physical Review letters* **71**(13), 2030.

[118] Xi, H.-w., Viñals, J. and Gunton, J. [1992], 'Numerical study of pattern formation following a convective instability in non-Boussinesq fluids', *Physical Review A* **46**(8), R4483.

[119] Yochelis, A., Burke, J. and Knobloch, E. [2006], 'Reciprocal oscillons and nonmonotonic fronts in forced nonequilibrium systems', *Physical Review letters* **97**(25), 254501.

[120] Zhao, B. and Tian, Z. [2015], 'Numerical investigation of binary fluid convection with a weak negative separation ratio in finite containers', *Physics of Fluids* **27**(7), 074102.

[121] Zimmermann, W., Armbruster, D., Kramer, L. and Kuang, W. [1988], 'The effect of spatial modulations on codimension-2 bifurcations', *EPL (Europhysics Letters)* **6**(6), 505.